Hybrid Kernelised Expectation Maximisation Reconstruction Algorithms for Quantitative Positron Emission Tomography

Daniel Deidda

University of Leeds
Biomedical Imaging Science Department
&
Department of Statistics

Submitted in accordance with the requirements for the degree of
Doctor of Philosophy
September 20, 2018

Intellectual Property and Publications

The candidate confirms that the work submitted is his own, except where work which has formed part of jointly authored publications has been included. The contribution of the candidate and the other authors to this work has been explicitly indicated in the next page. The candidate confirms that appropriate credit has been given within the thesis where reference has been made to the work of others.

Joint Publications

Work from the following jointly authored publications, which is listed as Deidda et al. [2016, 2017, 2018a,b, 2019a,b] in the References, is included in this thesis:

Journal papers

Daniel Deidda, Nicolas A. Karakatsanis, Nikos Efthimiou, Yu-Jung Tsai, Philip M. Robson, Kris Thielemans, Zahi A. Fayad, Robert G. Aykroyd, and Charalampos Tsoumpas. Hybrid PET-MR List-Mode Kernelized Expectation Maximization Reconstruction. *Inverse Problems;* ***Accepted***,
DOI: `https://doi.org/10.1088/1361-6420/ab013f`.

The candidate proposed, implemented into STIR, and validated the novel method together with the non hybrid version, he performed all the image reconstructions, C++, bash and R code writing, image analysis and paper writing as well as many other aspects. The organisation of the manuscript and writing corrections were jointly performed with co-authors. The acquisition experiment was performed by the co-authors.

Daniel Deidda, Nicolas A. Karakatsanis, Nikos Efthimiou, Philip M. Robson, Zahi A. Fayad, Robert G. Aykroyd, and Charalampos Tsoumpas. Effect of PET-MR Inconsistency in the Kernel Image Reconstruction Method.
IEEE Transactions on Radiation and Plasma Medical Sciences; ***Accepted***,
DOI: `https://doi.org/10.1109/TRPMS.2018.2884176`.

Daniel Deidda, Nicolas A. Karakatsanis, Claudia Calcagno, Philip M. Robson, Max Senders, Willem J. M. Mulder, Zahi A. Fayad, Robert G. Aykroyd, and Charalampos Tsoumpas, Hybrid PET-MR Kernelised Expectation Maximisation Reconstruction for Improved Image- Derived Estimation of the Input Function from the Aorta of Rabbits.
Contrast Media and Molecular Imaging; ***Accepted***,
DOI: `https://doi.org/10.1155/2019/3438093`.

The candidate designed the study, performed all the data simulations and image reconstructions, C++, bash and R code writing, image analysis and paper writing as well as many other aspects. The organisation of the manuscript as well as writing corrections were jointly performed with co-authors. The acquisition experiment was performed by the co-authors.

Mercy I. Akerele, **Daniel Deidda**, Jacobo Cal-Gonzalez, Rachael O. Forsythe; Marc R. Dweck; Nicolas A. Karakatsanis, Robert G. Aykroyd; Steven Sourbron; and Charalampos Tsoumpas, Comparison of Correction Techniques for the Spill-in Effect in Emission Tomography,
IEEE Transactions on Radiation and Plasma Medical Sciences; ***Submitted***

The candidate supported the study with ad hoc scripts to enable the use of the HKEM algorithm. The organisation of the manuscript as well as writing corrections were jointly performed with co-authors.

Book Chapter

Daniel Deidda, Robert G. Aykroyd, and Charalampos Tsoumpas. Assessment of Maximum A Posteriori Image Estimation Algorithms for Reduced Acquisition Time Medical Positron Emission Tomography Data. *Recent Studies on Risk Analysis and Statistical Modeling*, pages 3–16. Springer, 2018.
DOI: `https://doi.org/10.1007/978-3-319-76605-8_1`

The candidate performed the image reconstructions, bash and R code writing, image analysis and paper writing as well as many other aspects. The organisation of the manuscript corrections were jointly performed with co-authors.

Conference Papers

Daniel Deidda, Nikos Efthimiou, Richard Manber, Kris Thielemans, Pawel Markiewicz, Robert G. Aykroyd, and Charalampos Tsoumpas. Comparative Evaluation of Image Reconstruction Methods for the Siemens PET-MR Scanner Using the STIR Library. *Nuclear Science Symposium and Medical Imaging Conference Record*, pages 1–6. IEEE, 2016,
DOI: `https://doi.org/10.1109/NSSMIC.2016.8069615`.

The candidate performed all the image reconstructions, bash and R code writing, image analysis and paper writing as well as many other aspects. The organisation of the manuscript as well as writing corrections were jointly performed with co-authors. The acquisition experiment was performed by the co-authors.

Daniel Deidda, Nicolas A. Karakatsanis, Philip M. Robson, Nikos Efthimiou, Zahi A. Fayad, Robert G. Aykroyd, and Charalampos Tsoumpas. Hybrid PET-MR list-mode kernel expectation maximization reconstruction for quantitative PET images of the carotid arteries. *Nuclear Science Symposium and Medical Imaging Conference Record*. IEEE, 2017, DOI: `https://doi.org/10.1109/NSSMIC.2017.8532641`.

The candidate proposed, implemented into STIR, and validated the novel method together with the non hybrid version, he performed all the image reconstructions, C++, bash and R code writing, image analysis and paper writing as well as many other aspects. The organisation of the manuscript and writing corrections were jointly performed with co-authors. The acquisition experiment was performed by the co-authors.

Conference Abstracts

Daniel Deidda, Nikos Efthimiou, Richard Manber, Kris Thielemans, Pawel Markiewicz, Robert G. Aykroyd, and Charalampos Tsoumpas. Comparative Evaluation of Image Reconstruction Methods for the Siemens PET-MR Scanner Using the STIR Library. *Nuclear Science Symposium-Medical Imaging Conference*. IEEE, 2016, Strasbourg, France (Poster presentation).

Daniel Deidda, Nicolas A. Karakatsanis, Philip M. Robson, Nikos Efthimiou, Zahi A. Fayad, Robert G. Aykroyd, and Charalampos Tsoumpas. Hybrid PET-MR List-Mode Kernelized Expectation Maximization Reconstruction for Quantitative PET Images of the Carotid Arteries. *Nuclear Science Symposium-Medical Imaging Conference*. IEEE, 2017, Atlanta, Georgia, USA (Oral presentation).

Daniel Deidda, Nicolas A. Karakatsanis, Philip M. Robson, Yu-Jung. Tsai, Nikos. Efthimiou, Kris. Thielemans, Zahi A. Fayad, Robert G. Aykroyd, and Charalampos Tsoumpas. A Comparison of the Hybrid Kernel and the Parallel Level-Sets Approaches for the Inclusion of MR Information into PET Reconstruction *7^{th} Conference on PET-MR and SPECT-MR*, Isola d'Elba, Italy, 2018 (Oral presentation).

The candidate implemented, and validated both the anatomically-guided methods into STIR, he performed all the image reconstructions, C++, bash and R code writing, image analysis and paper writing as well as many other aspects. The organisation of the summary and abstract was jointly performed with co-authors. The acquisition experiment was performed by the co-authors.

Daniel Deidda, Nicolas A. Karakatsanis, Philip M. Robson, Zahi A. Fayad, Robert G. Aykroyd, and Charalampos Tsoumpas. Multiplexing Kernelized Expectation Maximization Reconstruction for PET-MR. *Nuclear Science Symposium-Medical Imaging Conference*. IEEE, 2018, Sydney, Australia (November 2018, Poster presentation).

The work related to this abstract is still work in progress and the results as presented in the accepted summary are included the Appendix A. The candidate proposed an enhancement of the HKEM, implemented it in the STIR library, performed the reconstructions and analysis, and wrote the submitted summary.

The work described in the following publications is not discussed in this thesis. However, the achievements of this thesis were also utilized in these studies:

Richard Brown, Ben Thomas, Alaleh Rashidnasab, Yu-Jung Tsai, **Daniel Deidda**, Evgueni Ovtchinnikov, Edoardo Pasca, Casper da Costa-Luis, Brian Hutton, Charalampos Tsoumpas and Kris Thielemans. Motion-Corrected PET Reconstruction with SIRF. *7^{th} Conference on PET-MR and SPECT-MR*, Isola d'Elba, Italy, 2018 (Oral presentation).

Mercy I. Akerele, **Daniel Deidda**, Jacobo Cal-Gonzalez, and Charalampos Tsoumpas. Improved Correction Techniques for Partial Volume and Spill-in Effects' Compensation in PET. *Nuclear Science Symposium-Medical Imaging Conference*. IEEE, 2018, Sydney, Australia (November 2018, oral presentation).

Acknowledgements

I wish to express deeply gratitude to both my supervisors Dr Charalampos Tsoumpas and Dr Robert Aykroyd for their constant intellectual support, constructive comments and warm encouragement during the last 3 years, and most importantly thanks for always being critical and honest, I feel this has positively changed my way of thinking about my work and other people's work. I also wish to thank Prof. Zahi Fayad who has been my external supervisor and clinical advisor for this project and for making possible to collaborate with his research team at the Mount Sinai, Icahn School of Medicine; in fact, I owe my deepest gratitude to the group at the Translational and Molecular Imaging Institute (TMII), Icahn School of Medicine at Mount Sinai, Department of Radiology in New York for the help provided with acquisition of almost all the data I used in this thesis. Thanks to Dr Nicolas Karakatsanis for the time spent to discuss the research and the constructive feedback. I would like to offer my special thanks to Dr. Kris Thielemans and the Collaborative Computational Project in Positron Emission Tomography and Magnetic Resonance imaging (CCP PET MR), funded with EP/M022587/1 grant, to allow me to be able to reconstruct the PET-MR data with all possible corrections using STIR, and to fund my attendance to the exchange programme at the Institute of Nuclear Medicine, UCL in London, and the provision of the Hoffman phantom dataset as well as the attendance to the 7^{th} conference on PET-MR and SPECT-MR (PSMR).

I thank, the University of Leeds and in particular the Leeds Institute of Cardiovascular and Metabolic Medicine (LICAMM) for providing a very welcoming environment and for all the help received with the administrative work. Thanks to my group, Mercy, Palak and Richa for being the best group I could have ever asked for. Thanks to Richa, Mercy, Sirisha, Nikos and Demetra for proofreading this thesis. Thanks to all the colleagues I met for allowing me to learn everyday something new and to see things from different perspectives. This work was undertaken on MARC1, part of the High-Performance Computing and Leeds Institute for Data Analytics (LIDA) facilities at the University of Leeds. A project like this would not have been feasible without such facilities. I am grateful to the University of Leeds for awarding me with the University Research Scholarship which allowed me to start this journey.

Finally, I wish to thank my parents, Gina and Ugo, for supporting me in everything I do, there are no words to express how lucky I am to have you. Thanks to my brothers, Marco and Davide, all my family and friends for all the fun we had and we will have, and for making me understand that, no matter how far we will be, I can always count on you. My deepest appreciation goes to Sara; thanks for following me in this adventure, for believing in me and for the unconditional love. Life as a Ph. D. student can some time be tough and overwhelming, but having the right people around you can make everything much easier.

Abstract

Positron emission tomography (PET) imaging is commonly used in clinical practice to diagnose different diseases. However, the limited spatial resolution sometimes prevents the desired diagnostic accuracy. This work examines some of the issues related to PET image reconstruction in the context of PET-magnetic resonance (MR) imaging, and proposes a novel PET iterative reconstruction algorithm, hybrid kernelised expectation maximisation (HKEM), to overcome these issues by exploiting synergistic information from PET and MR images. When the number of detected events is low, the reconstructed images are often biased and noisy. Anatomically-guided PET image reconstruction techniques have been demonstrated to reduce partial volume effect (PVE), noise, and improve quantification, but, they have also been shown to rely on the accurate registration between the anatomical image and the PET image, otherwise they may suppress important PET information that may lead to false negative detection of disease. The aim of the HKEM algorithm is to maintain the benefits of the anatomically-guided methods and overcome their limitations by incorporating synergistic information iteratively. The findings obtained using simulated and real datasets, by performing region of interest (ROI) analysis and voxel-wise analysis are as follows: first, anatomically-guided techniques provide reduced PVE and higher contrast compared to standard techniques, and HKEM provides even higher contrast in almost all the cases; second, the absolute bias and the noise affecting low-count datasets is reduced; third, HKEM reduces PET unique features suppression due to PET-MR spatial inconsistency. This thesis, therefore argues that using synergistic information, via the kernel method, increases the accuracy and precision of the PET clinical diagnostic examination. The promising quantitative features of the HKEM method give the opportunity to explore many possible clinical applications, such as cancer and inflammation.

Contents

List of Figures

List of Tables

Chapter 1

Introduction

1.1 Context and Motivation

The aspiration for image quality and quantification improvements for positron emission tomography (PET) imaging has led to the introduction and use of multi-modality scanners such as PET-computational tomography (CT) and PET-magnetic resonance (MR). PET-CT has become the gold-standard in clinical routine due to the high-resolution anatomical image provided by CT and the corresponding electron density information that can be used for attenuation correction in PET image reconstruction. On the other hand, the benefits for PET-MR are multiple. For example, the high contrast in soft tissues provided by MR allows for a more accurate localisation of the high uptake PET regions. This information can be used as 'prior' information to reduce the partial-volume effect (PVE) (Shidahara et al. [2012]) which degrades PET image quality and quantification. Due to the wide range of possible MR sequences that can be acquired during the PET-MR scan, according to which tissue one wants to study, there

are a number of possible applications that can be investigated. Furthermore, MR images can be used to detect and correct motion (Tsoumpas et al. [2013]), and the magnetic field can improve the resolution of PET by reducing the positron range (Hammer et al. [1994] and Bertolli et al. [2014]). Finally, due to the absence of ionising radiation during an MR acquisition, a PET-MR examination will involve less dose for the patient than a PET-CT examination. As a consequence, it is also relevant to reduce the dose delivered by the PET radiotracer. The dose reduction as well as the use of very short frames (5-30 s), lead to low-count circumstances, which produce noisy and biased images (Halpern et al. [2004]). Short frames are often used in dynamic studies in both PET-CT and PET-MR. MR-guided reconstruction techniques can be used in these circumstances as well as in normal-count situations to reduce PVE which is especially important when low-count data is used. Short frames are used, for example, for the estimation of the image-derived input function (IDIF) in kinetic modelling analysis (Schmidt and Turkheimer [2002]), and the accuracy of the IDIF is crucial for an accurate kinetic analysis. On the other hand, the injection of lower amounts of radioactivity has the potential to allow the examination to more patients, including pregnant woman and children (Karakatsanis et al. [2015]; Cherry et al. [2018]). This thesis focuses on developing methods for the improvement of quantification at different count-levels. Emphasis is given to low-count datasets obtained with short acquisition times. In fact, the improvements in terms of noise suppression, accuracy and contrast seen with the proposed method for the images reconstructed with short acquisition times is also likely to be achieved in the case of lower injected radioactivity dose.

1.2 Purpose of the Thesis

The main goal of this work is to propose and develop a novel image reconstruction algorithm for PET which encodes synergistic information from PET and MR in the model. The purpose is to be able to correct for PVE, recover activity and contrast of small features, such as lesions, and avoid the suppression of regions which are only detected by PET. The proposed algorithm is an iterative method where the anato-functional information is included via the kernel method described by Hoffman et al. [2008]. The reason behind the choice of synergistic PET-MR features in this thesis is related to the fact that they allow to better preserve the quantification and shape of the PET unique structure. This thesis presents the validation of the proposed hybrid kernelised expectation maximisation (HKEM) method with simulated and real data where it is possible to see how the proposed technique addresses the aforementioned issue for small lesions. The PET-MR inconsistency problem is also studied as well as the application of the HKEM for the estimation of the IDIF in the aorta of rabbits.

The specific achievements of this thesis are listed as follows:

1) The accuracy and precision performance and limitations of the standard iterative algorithms using low-count datasets were investigated and discussed;

2) Both sinogram and list mode (LM)-based anatomically-guided image reconstruction algorithm, HKEM and kernelised expectation maximisation (KEM) were implemented to reduce PVE and PET unique feature suppression;

3) The parallel level sets (PLS) prior (Ehrhardt et al. [2016]) was also im-

plemented for the comparison of the kernel method and the Bayesian approach.

4) The HKEM performance was explored in terms of quantification, and improvements in comparison with other techniques was shown;

5) The problem of PET-MR spatial inconsistency was investigated in terms of image quality and accuracy;

6) A simulation study based on real [^{18}F]Sodium Fluoride ([^{18}F]NaF) rabbit data was performed to provide the ground truth for the aorta. This allowed to study the accuracy of the IDIF;

7) The accuracy and precision of the estimates of the IDIF was studied using region of interest (ROI) analysis for rabbit data, where the ROI was extracted from both the MR image and the reconstructed PET image with the HKEM.

1.3 Thesis Overview

The thesis is divided into seven main chapters, which are interconnected through the theme of quantification investigation, and show the development of the related research project over time. The overview of the thesis is presented as follows:

Chapter 2: Background

The basic knowledge required to fully understand the contents of the thesis is briefly explained in this chapter. A concise description of the physical pro-

cesses involved in PET acquisition and the mathematical formulation of the most common iterative reconstruction algorithms is given. A similar explanation is presented for the MR, and finally, the motivation, limitations and some of the available techniques for PET-MR data correction and reconstruction are discussed.

Chapter 3: Quantitative Performances of Standard Iterative Reconstruction Techniques for Low-count PET-MR Data

In this chapter, the standard iterative reconstruction algorithms, that were described in Chapter 2, are used to reconstruct low-count datasets obtained from the Hoffman phantom. This introduces a discussion of the limitations of these methods on PET-MR low-count data when the anatomical information is not taken into account in the model. The difficulty in appropriately choosing the regularisation parameter values is described in this chapter. In particular, making the conclusion that different regions in the image may need a different parameter value to obtain the lowest root mean squared error (RMSE). The results of this chapter are published in Deidda et al. [2018a] and Deidda et al. [2016].

Chapter 4: Introduction and Validation of List-Mode Hybrid-Kernelised Expectation Maximisation

In this Chapter, the HKEM algorithm, which takes into account anatomical and functional information in the model, is proposed and validated. The novelty of the method lies in the exploitation of the features within the PET image

iteratively and combine these with the anatomical information within the MR image. This was designed to overcome the issue of over-smoothing and potential suppression of PET unique features. The method is tested with four different datasets, including simulation, phantom and patient data, to explore lesion bias and contrast with different noise levels. Previous related works is also discussed in the introduction. The results of this chapter are published in Deidda et al. [2019a] and Deidda et al. [2017]. Part of the work shown in this chapter was given as an oral presentation at the IEEE Medical Imaging Conference, Atlanta, USA, 2017, and at the 7th Conference on PET-MR and SPECT/MR, Isola d'Elba, Italy, 2018.

Chapter 5: Investigation of the Effect of PET-MR Inconsistency in the Kernel Image Reconstruction Method

The HKEM and the KEM methods used in the previous chapter are studied here in cases where the PET and MR images contain spatial inconsistency due to motion, inaccurate registration or simply where different regions are detected by PET and MR. The spatial inconsistencies are created by augmenting the MR images with shifts along the same direction and different distances for both phantom and patient data. The aim of this study is to quantify and investigate the possible limitations of the proposed algorithm in the case of erroneous feature vectors due to inaccurate registration or inappropriate choice of the MR image. The results of this chapter are published in Deidda et al. [2018b].

Chapter 6: Hybrid PET-MR Kernelised Expectation Maximisation Reconstruction for Accurate Image-Derived Estimation of the Input Function From the Aorta of Rabbits

The synergistic nature of the HKEM is exploited in this chapter to improve the accuracy of IDIF estimation. The HKEM is used for the reconstruction of the PET images first, and finally the reconstructed image is used for the extraction of the ROI of the rabbit aorta to be used for the analysis. To compare HKEM IDIF estimates with the ground truth, a realistic rabbit simulation, with different noise realisations, was created. The technique was also used with two real rabbit datasets, in particular two different radiotracers were used, [^{18}F]NaF and [^{18}F]-fluorodeoxyglucose ([^{18}F]FDG), to demonstrate applicability of the method in different cases. The results of this chapter are published in Deidda et al. [2019b].

Chapter 7: General Conclusion and Future Work

The general conclusions of the thesis are discussed in this chapter together with work in progress and possible future directions.

Appendix A: Multiplexing Kernelised Expectation Maximisation Reconstruction for PET-MR

An extension of the HKEM method is proposed in this Appendix and preliminary results from a simulation are discussed. The work is presented as submitted and accepted for the IEEE Medical Imaging Conference, Sidney, Australia, 2018. In this work, a version of the kernel method is proposed and investigated. This exploits the information contained in multiple MR images, and potentially CT

or other PET images can also be used. To do so, the HKEM was modified such that the kernel matrix is obtained using additional Gaussian terms carrying the features from multiple images.

Appendix B: Implementation of the Kernelised Expectation Maximisation Reconstruction in STIR

This appendix chapter schematically describes the implemented kernel reconstruction in the form of pseudo-code. The written code reproduces the reconstruction algorithm, and the class hierarchy.

Appendix C: Description of the Demonstrative code for the rabbit simulation

The last appendix chapter shows the README file from the Demonstrative code created for the simulation in Chapter 6.

Chapter 2

Background

The current chapter describes the basis of PET-MR imaging. In particular, it starts with a brief discussion of the physical basis of PET and continues with the data acquisition and image formation (Section 2.1). Emphasis is given to the PET image reconstruction part, as it represents the background of the work carried out throughout this research project. Section 2.2 provides a short description of the MR physics, data acquisition and image formation. Finally, in Section 2.3 a summary of the benefits and drawbacks, and available techniques of hybrid PET-MR imaging are provided.

2.1 PET Theory

2.1.1 Data Acquisition and Correction

PET is a non-invasive imaging technique used in clinical practice for diagnostic imaging, dose delivery and treatment response evaluation. It is able to image metabolism, calcification, inflammation and so on, but is mostly used clinically

for cancer detection. It requires the patient to be injected with a radiotracer, which consists of molecules labelled with positron-emitting radionuclides with short half-life. The molecules used for the radiotracer are analogues of biological molecules and thus they are able to represent typical biological processes after in vivo administration correctly. For example, [^{18}F]FDG with a half-life of 109.6 minutes, is an equivalent of glucose and is used to image cellular metabolism. The positron-emitting radionuclide is extracted in a machine called cyclotron, which basically accelerates protons in circular trajectories to reach energies of about 10-20 MeV. When the protons reach the right energy, they are forced to interact with a specific target material to produce the radioisotope. After this the isotope will be linked to the [^{18}F]FDG molecule via radiochemical processes. The PET imaging technique takes advantage of the physical effect that goes under the name of 'Annihilation Matter-Antimatter'. In this process, a positron emitted by the radiotracer travels for few millimetres before interacting with an electron. As soon as the interaction takes place, the positron and the electron rest masses are converted into a pair of annihilation photons. The photons with identical energies (511 keV) are emitted simultaneously in about 180 degree opposing directions, and are detected by two opposite detectors in the scanner ring. The detection of the two annihilation photons allows the definition of a line of response (LOR), which represents the line along which the event happened. During its path, the positron will lose energy via Coulomb interactions until it reaches thermal energies (about 0.025 eV). At this point the positron will start interacting via anhilation. Around 84% of the anhilition photons are not antiparallel due to the momentum of the bound electron that interacts with the positron, and the angular variation is around 4 mrad. The distance travelled

from the positron emission to the anhilation is called positron range, and it is of the order of 1 mm for [^{18}F]FDG. The LOR is characterised by its angle of orientation respective to the horizontal plane and the shortest distance between the LOR and the centre of the ring. In Figure (2.1), the angle is plotted as a function of the distance from the centre and four coincidence events are shown. When a large number of LORs are plotted corresponding to the same point (or voxel) the resulting graph is half of a sine wave, hence the graph is aptly called a 'sinogram'. This graph represents the measured data where the rate of detected events (count rate) gives a measure of the injected activity.

With complex objects, the measured data will then consist of a large number of overlapping sine waves (Fahey [2002]). The sinogram is stored in a matrix where each LOR represents a specific entry in this matrix called a bin. Modern scanners allow fully 3D acquisition and contain several rings, therefore, the axial position of the LOR and the difference between the ring indexes need to be taken into account, as there will be events where the two photons hit detectors in two different rings. The events which occurred within one ring are referred to as 'direct' coincidence whereas those occurred between different rings are called 'cross' coincidences. For every scanner with n rings, there are n direct plane and for every plane there are $n-1$ cross planes, which leads to a total of n^2 total sinograms.

Another way to store the detected events is LM; the events are organised into a list where every event is associated with timing information, energy, detector indexes and so on. This type of raw data can be space demanding according to the number of events; however, it preserves time and spatial information that is otherwise lost during the binning into sinogram. The LM data can also be useful

to make the reconstruction faster in case of low-counts and implicitly avoid LOR with no events (Reader et al. [1998b]).

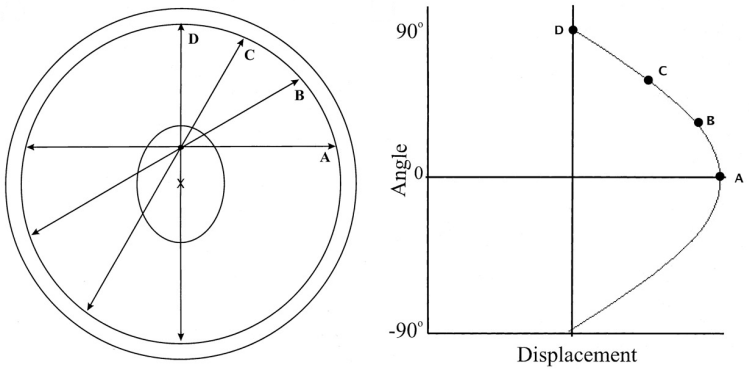

Figure 2.1: Representation of sinogram formation for 2D acquisition (Fahey [2002]).

PET data, in practice, presents a certain level of inaccuracy due to physical phenomenon, such as Compton scattering and photoelectric absorption which reduce the number of detected events. Compton scattering produces a change in direction and energy of one or both photons, resulting in an erroneous LOR. This results in a contrast loss and quantification degradation in the image (Mumcuoglu et al. [1996]). To correct for such effect, the scattered events are estimated from the data using the single scatter simulation method proposed by Watson et al. [1996] where the Klein-Nishina formula is used to estimate the probability of an event represented by a LOR to be a scattered event.

The loss of photons is also the reason behind what is called attenuation, which represents the loss of coincident events due to both scatter and absorption of one or both annihilation photons. For a point inside an object, the attenuation depends on the average depth of the object and its electron density. The human body consists of several organs and tissues with different sizes and densities.

Therefore, an accurate estimation of the attenuation coefficients is needed for each part of the body. An image with no attenuation correction will show the inner part of the organ having lower activity concentration compared to the boundaries. The adopted technique for the attenuation factor estimation uses the X-ray CT, where a beam of photons with intensity, I_0, is directed towards an object and after passing through it the beam intensity will be reduced to, I. The attenuation correction is performed by calculating the probability that the two photons are detected:

$$P = e^{-\sum_i \mu_i (d_{1i} + d_{2i})}, \tag{2.1}$$

where μ_i is the attenuation coefficient for a tissue i, d_{1i} and i, d_{2i} are the depth travelled by photons 1 and 2 inside the tissue i. On the other hand, the CT is measuring at different energy so there is not necessarily a straightforward correction (Hutton et al. [2011]).

Another contribution to inaccuracy is represented by the random events. Such events consist of two photons, from different annihilation, that have been detected simultaneously by two opposite detectors, resulting again in an erroneous LOR (Brasse et al. [2005]). To correct for random events, the rate of singles are estimated for each detector and the randoms are estimated for each detector pair, ij, as follows:

$$\overline{R_{ij}} = 2\tau \overline{S_i}\,\overline{S_j}, \tag{2.2}$$

where τ is the time width of the pulses for the system and $\overline{S_i}$ and $\overline{S_j}$ are the single count rates for the two detectors. In summary, the total number of events in the

PET sinogram bin, also called prompts, contains also random and scattered events which need to be estimated and subtracted. As a consequence, the true estimated events for one bin, $\overline{T}$, can be represented as follows:

$$\overline{T} = \overline{P} - \overline{S} - \overline{R}, \tag{2.3}$$

where $\overline{P}$ is the prompt count rate, $\overline{S}$ the estimated scatter count rate and $\overline{R}$ the estimated random events. Finally, as the radioactive decay is a random process, the number of photons passing through an object and absorbed in a detector are random variables governed by Poisson statistics (Alpert et al. [1982]). This results in statistical noise and imprecision in activity estimates, as discussed by Frey et al. [2012, and references therein]. Image reconstruction algorithms tend to amplify the high frequency component of this noise, and a post-filtering process is usually needed (Barrett et al. [1994]). The latter, however, can significantly affect the resolution of the image. Several cutting-edge techniques have been proposed in the literature which include Bayesian and machine learning methods to keep the noise low while preserving resolution (Bowsher et al. [1996]; Ahn et al. [2015]; and Gong et al. [2018b]).

2.1.2 PET Image Reconstruction

PET reconstruction is an inverse problem where projection data (sinogram or LM) are used to estimate the true activity distribution. The forward problem in this case is represented in matrix symbols as $\overline{Y} = C\lambda$, where $\overline{Y}$ is the vector containing the mean of each projection, C is the projection matrix and λ is the image of the activity distribution. However, the matrix C is not a square

matrix and therefore is not invertible. A possible way to solve the problem is to find a pseudo inverse which can be obtained using for example the singular value decomposition (SVD) which allows the factorisation of a matrix C in the form $U\Sigma V^*$, where U is a real or complex unitary square matrix $(n \times n)$, Σ is a real or complex rectangular diagonal matrix $(n \times m)$ with non-negative real numbers on the diagonal called singular values, V is a real or complex unitary square matrix $(m \times m)$, and V^* is the transpose of the complex conjugate of V. The columns of U and the columns of V represent the left-singular vectors and right-singular vectors of C, respectively. The condition number, which can be described as the ratio between the largest and the smallest non-zero singular values, gives us a way to measure the ill-conditioning of the problem. If the condition number is high the problem is ill-conditioned, and small changes in $\overline{Y}$ can results in large changes in λ. To reduce the problem a threshold, t, can be used to force to zero the singular values which are smaller than t. If the image of our linear matrix, C, is smaller than the data space, for some λ values the equation, $\overline{Y} = C\lambda$, has no solution and it is necessary to use some conditions such as maximum likelihood to select a vector λ' that minimise the discrepancy between the measured data and the estimated vector $C\lambda'$. If the image of C is smaller than the image space, there will be infinite solutions to the problem for the same $\overline{Y}$. In order to tackle this problem additional information is necessary, which can be provided via regularisation.

The state-of-the-art for image reconstruction in the clinical practice is represented by iterative algorithms, as they make it possible to incorporate the Poisson nature of photon measurement measurement, taking into account noise and a number of other relevant physical features (Lange and Carson [1984]).

The currently used algorithms for PET are based on the same concept as the maximum likelihood expectation maximisation (MLEM) algorithm proposed by Shepp and Vardi [1982]. In this method, every single voxel of the 3D image is updated during each iteration with the value that maximises the Poisson likelihood. The iterative methods make it possible to model noise and a number of other relevant physical features (Reader and Zaidi [2007]) such as system resolution (Reader et al. [2003]). On one hand, MLEM is accurate and a globally convergent algorithm (Lange and Carson [1984]). On the other hand, it takes many iterations before it reaches convergence. An accelerated version of MLEM was developed by Hudson and Larkin [1994] using ordered subsets of projection data. Such method, called ordered subsets expectation maximisation (OSEM) is largely used in the clinical practice with PET studies, because it is easily implemented and provides reconstruction acceleration over MLEM. Other algorithms are available in literature, such as the Bayesian maximum a posteriori (MAP), proposed by Green [1990a], where the posterior density function is maximised rather than the density function, incorporating prior information.

MLEM

The mathematical description in this section uses the same formalism as Lange and Carson [1984]. MLEM is an iterative technique for computing maximum likelihood estimates. The basic idea is the following: suppose the measured data in an acquisition is Y (a sinogram) with a density function $g(Y, \lambda)$, which follows the Poisson distribution, where λ is the image to be estimated. The MLEM method aims to maximise the logarithm of this density function, $l(Y, \lambda)$

$= \ln(g(Y, \lambda))$, also called an objective function:

$$l(Y, \lambda) = \sum_{i=1}^{N} \left[y_i \ln(\sum_{j \in I_i} c_{ij} \lambda_j) - \sum_{j \in I_i} c_{ij} \lambda_j - \ln(y_i!) \right], \tag{2.4}$$

where I_i is the set of voxel contributing to projection i, N is the number of projections in the data, c_{ij} represents the probability that an event occurring in voxel j produces a coincidence in the i_{th} pair of detectors and takes into account the attenuation and normalisation corrections, λ_j is the intensity of the voxel j in the emission image, y_i represents the number of events detected in projection i. If y_i represents the number of pairs of photons detected in projection i, then X_{ij} is defined as the number of pairs of photons emitted from voxel j and detected in projection i and is related to y_i by the following:

$$y_i = \sum_{j \in I_i} X_{ij} \tag{2.5}$$

X is also called 'complete data' while Y is the 'incomplete data'. To make the maximisation easier, the complete data log-likelihood needs to be used

$$l(X, \lambda) = \sum_{i=1}^{N} \sum_{j \in I_i} \left[X_{ij} \ln(c_{ij} \lambda_j) - c_{ij} \lambda_j - \ln(X_{ij}!) \right]. \tag{2.6}$$

In order to obtain the algorithm updating formula, where n is the current iteration number, two steps are necessary:

- Expectation step (E step): during this step, the algorithm estimates the conditional expectation value of $l(X, \lambda)$, $E(l(X, \lambda)|Y, \lambda^{(n)})$, where $\lambda^{(n)}$ at the first iteration is usually a uniform image. The expected value for $l(X, \lambda)$ given the measured data Y and $\lambda^{(n)}$ is:

$$E(l(X,\lambda) \mid Y, \lambda^{(n)}) = \sum_{i,j} \left[\frac{c_{ij}\lambda_j^{(n)} y_i}{\sum_{k \in I_i} c_{ik}\lambda_k^{(n)}} \ln(c_{ij}\lambda_j) - c_{ij}\lambda_j \right] + R, \tag{2.7}$$

where R are the factors that do not depend on λ_j and hence will not appear in the next step.

- Maximisation step (M step): in this step, the image that maximise the expected objective function is estimated, this is achieved by simply taking the partial derivatives of (2.7):

$$\left. \frac{\partial E(l(X,\lambda) \mid Y, \lambda^{(n)})}{\partial \lambda_j} \right|_{\lambda=\lambda^{(n)}} = \sum_{i \in J_j} \left[\frac{c_{ij}\lambda_j^{(n)} y_i}{\sum_k c_{ik}\lambda_k^{(n)}} \lambda_j^{-1} - c_{ij} \right] = 0, \tag{2.8}$$

  where J_j is the set of projections to which voxel j contributes.

  The resulting formula describes the MLEM algorithm

$$\lambda_j^{(n+1)} = \frac{\lambda_j^{(n)}}{\sum_{i \in J_j} c_{ij}} \sum_{i \in J_j} c_{ij} \frac{y_i}{\sum_{k \in I_i} c_{ik}\lambda_k^{(n)}}. \tag{2.9}$$

Then $\lambda_j^{(n+1)}$ will be used in the E step for the next iteration and the procedure is repeated for a number of iterations which can be decided according to a specific figure of merit. Equation (2.9) is summarised in Figure (2.2). Many studies have also proposed LM reconstruction algorithms (Snyder and Politte [1983]; Barrett et al. [1997]; Reader et al. [1998a,b]; Parra and Barrett [1998]; Byrne [2001]; Huesman et al. [2000]; and Levkovilz et al. [2001]). For the LM reconstruction, equation (2.9) becomes:

$$\lambda_j^{(n+1)} = \frac{\lambda_j^{(n)}}{\sum_{i \in J_j} c_{ij}} \sum_{i=1}^{L} c_{ij} \frac{1}{\sum_{k \in I_i} c_{ik}\lambda_k^{(n)}}, \tag{2.10}$$

where the sinogram bin y_i is substituted by the summation over LM events which goes from 1 to L total number of detected events, similarly to the description by Reader et al. [2002].

The MLEM algorithm is demonstrated to be a convex algorithm, nevertheless, it is computationally demanding and it takes a lot of iterations to reach the maximum likelihood estimate. This derivation does not take into account random and scatter effects. If one wants to correct the image, the algorithm can be extended by adding the additive sinogram term, which takes into account scatter and random events:

$$y_i = \sum_{j \in I_i} X_{ij} + A_i, \tag{2.11}$$

$$\lambda_j^{(n+1)} = \frac{\lambda_j^{(n)}}{\sum_{i \in J_j} c_{ij}} \sum_{i \in J_j} c_{ij} \frac{y_i}{\sum_{k \in I_i} c_{ik} \lambda_k^{(n)} + a_i}, \tag{2.12}$$

where a_i represent the element of the additive sinogram A in projection i.

OSEM

The OSEM algorithm provides acceleration of convergence, proportional to the number of subsets, by simply processing the data in subsets (blocks) within each full iteration. The projection data is organised in ordered subsets and the MLEM method is applied to each subset in turn. The resulting reconstruction after each subset becomes the starting point for the following subset, each step is called a sub-iteration. In this way, every iteration passes through every subset.

These blocks are usually chosen so that the projections within a block correspond to the projections of the image with down-sampled projection angle.

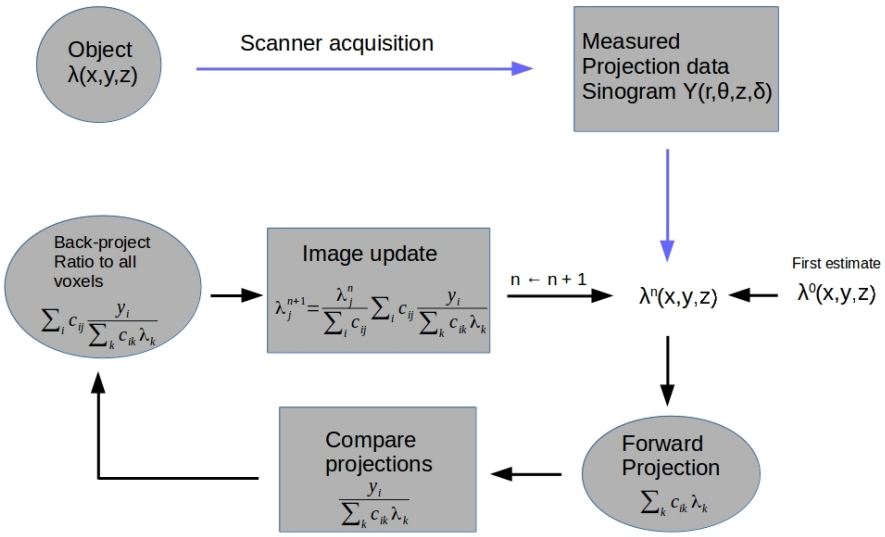

Figure 2.2: Schematic representation of the iterative algorithm Maximum Likelihood Expectation Maximisation starting from the initial estimate λ^0. In a 3D acquisition r is the distance between the centre of the ring and the LOR, θ is the angle between the LOR and the x axis (transaxial horizontal), z is the axial position and δ is the ring difference and $k \in I_i$.

Hudson and Larkin [1994] showed that it is advantageous to select subsets in a balanced way so that voxel activity contributes equally to any subset. To provide this balance it is suggested to use a number of subset which is a divisor of the number of detector blocks in a ring (Byrne [1998]). The Siemens mMR has 63 blocks per ring with 8×8 detectors per block and consequently, the choice could be between 3, 9, 21 and 63. Following the same procedure as the MLEM, the OSEM algorithm is obtained by substituting the sum over i with the sum over $s \in S_m$ in equation (2.12), where S_m is the chosen subset of detector pairs and

$m = 1, ..., M$, where M is the number of subsets:

$$\lambda_j^{(m+1)} = \frac{\lambda_j^{(m)}}{\sum_{s \in S_m} c_{sj}} \sum_{s \in S_m} c_{sj} \frac{y_s}{\sum_{k \in I_i} c_{sk} \lambda_k^{(m)} + a_s}. \tag{2.13}$$

Although, OSEM provides order-of-magnitude acceleration over MLEM, the MLEM noise artefact is magnified after each iteration. For this reason, in clinical practice, the reconstruction is often stopped at early iterations (Veklerov et al. [1988]; Gaitanis et al. [2010]; and Bissantz et al. [2006]), usually two or three for around 20 subsets (Liow and Strother [1991] Meikle et al. [1994]; Asma et al. [2012] and Ahn et al. [2015]) or a Gaussian post-filter is also applied (Hamill and Bruckbauer [2002]). It has been demonstrated that if the algorithm is initialised with a positive uniform image it provides similar images to MLEM with an acceleration factor that depends on the number of subsets. On the other hand, OSEM does not always converge and it can reach a limit cycle around the maximum likelihood point (Fessler [2000]).

OSMAPOSL

The ordered subset maximum a posteriori one step late (OSMAPOSL) algorithm is an extension of OSEM, where prior distributions are used and the maximisation step includes the differentiation of the posterior density. The derivatives of the prior term are computed at the point $\lambda = \lambda^m$ in order to find the optimum solution of the Bayesian formulation, this approximation is called one step late (OSL) and it was first proposed by Green [1990a,b]. The reconstructed image is

obtained by maximising the posterior distribution:

$$l(\lambda \mid Y) = \sum_{i=1}^{N} [y_i \ln(\sum_{j \in I_i} c_{ij}\lambda_j) - \sum_{j \in I_i} c_{ij}\lambda_j - \beta V(\lambda)], \tag{2.14}$$

where $\beta V(\lambda)$ is the energy function designed to penalise large differences between neighbouring voxels. In particular, it is suggested using energy functions of the form:

$$\beta V(\lambda) = \beta \sum_{j,k=1}^{n} \omega_{jk}\, v(\lambda_j - \lambda_k), \tag{2.15}$$

where $\beta > 0$ scales the strength assigned to the prior, ω_{jk} are positive constants that define a weight value for each neighbour voxel (in general, 1 for first-order interactions between orthogonal nearest neighbours and $1/\sqrt{2}$ for second order diagonal interactions), n is the number of neighbours and $v(\lambda_j - \lambda_k)$ is the potential function.

The corresponding reconstruction formula for the OSMAPOSL is:

$$\lambda_j^{m+1} = \frac{\lambda_j^m}{\left[\sum_{s \in S_m} c_{sj} - \beta \left.\dfrac{\partial V(\lambda)}{\partial \lambda_k}\right|_{\lambda=\lambda^m}\right]} \sum_{s \in S_m} c_{sj} \frac{y_s}{\sum_k c_{sk}\lambda_k^m}. \tag{2.16}$$

Some of the standard prior distributions, which are often used for PET imaging, are the quadratic prior (QP) (Levitan and Herman [1987]; Halpern et al. [2004]; and Huesman et al. [2000])) and median root prior (MRP) (Alenius and Ruotsalainen [1997, 2002]; Alenius et al. [1998]). The potential function V, for QP and MRP respectively are given by the following forms:

$$v\,(\lambda_j - \lambda_k) \propto (\lambda_j - \lambda_k)^2, \tag{2.17}$$

$$v\left(\lambda_j - \lambda_k\right) \propto \left(\lambda_j - M_k\right)^2, \tag{2.18}$$

where M_k is the median of the image voxels within the neighbourhood associated with voxel j. Many other prior distributions are available in the literature including edge preserving and anatomical-guided priors and will be discussed in the following sections. A potential pitfall of the method is the fact that big values of β can lead to a negative denominator in (2.16) which can break the algorithm and produce artifacts.

2.2 MR Theory

2.2.1 MR Imaging Physics

Magnetic resonance imaging (MRI) is a diagnostic technique which is able to image the anatomy of a human or animal body and ex-vivo tissues with high resolution and contrast between soft tissues without using ionising radiation. The high contrast between soft tissues makes MRI particularly useful to diagnose problems with joints, cartilage, ligaments, and tendons. It is also used to observe changes in tissue micro-structure and composition in disease processes such as inflammation, infection and cancer and it is also widely used in neuroscience.

The technique takes advantage of the so called nuclear magnetic resonance (NMR) effect. All the nuclei with an odd number of protons and/or neutrons possess an intrinsic magnetic moment and angular moment, that is to say, they possess a non-zero spin. Such a property makes it possible for a nucleus in a strong magnetic field, and excited by radio waves, to emit a radio frequency (RF) signal that can be detected. The hydrogen nucleus possesses this property and because the human body is made up to 70% water, containing such nuclei, the MRI is based on the resonance associated with hydrogen. In the absence of any external magnetic field, the hydrogen spin has a random orientation, while in the presence of a uniform magnetic field, $\boldsymbol{B_0}$, the spin will start precessing around the $\boldsymbol{B_0}$ direction or around the antiparallel direction of $\boldsymbol{B_0}$. The angular frequency, ω_0 of the precession is given by the Larmor equation:

$$\omega_0 = \gamma \left| \boldsymbol{B_0} \right|, \tag{2.19}$$

where γ is the gyromagnetic ratio, which is 42.58 MHz/T for hydrogen, and $|\boldsymbol{B_0}|$ is the strength of the static magnetic field.

Considering all the hydrogen nuclei in a tissue, the process of precession about $\boldsymbol{B_0}$ will raise a net magnetisation, $\boldsymbol{M}$, which is the overall effect of all the single magnetic moments. This is due to the fact that the magnetic moments are more likely to orientate in parallel with the magnetic field than anti-parallel, as it represents the lowest energy level. When there is no external field the net magnetisation is zero (McRobbie et al. [2017]).

2.2.2 Relaxation Mechanism

When no RF pulse is present, the net magnetisation, $\boldsymbol{M_0}$, is aligned with $\boldsymbol{B_0}$, which is aligned to the z-axis. The MR signal occurs when a RF pulse, $\boldsymbol{B_1}$, at the Larmor frequency is applied. This will rotate the magnetisation, which will start precessing about $\boldsymbol{B_0}$ at a certain angle. At this point, the magnetisation, $\boldsymbol{M_0}$, can be split into two components; one along the z axis, $\boldsymbol{M_z}$, also called the longitudinal component and a rotating component on the xy-plane, $\boldsymbol{M_{xy}}$, also called the transverse component. During the rotation of the transverse component about the z-axis, a fluctuating electromagnetic field, which will induce a current through the receiver coil, is generated. This signal is the MR signal.

When the RF pulse is off, $\boldsymbol{M_{xy}}$ will start decaying due to two simultaneous and independent processes: spin-lattice interaction and spin-spin interaction.The first will cause longitudinal relaxation while transverse relaxation is caused by both interactions.

During relaxation $\boldsymbol{M_{xy}}$ will start decaying and the net magnetisation will align again with $\boldsymbol{B_0}$ while the longitudinal component will be restored, as de-

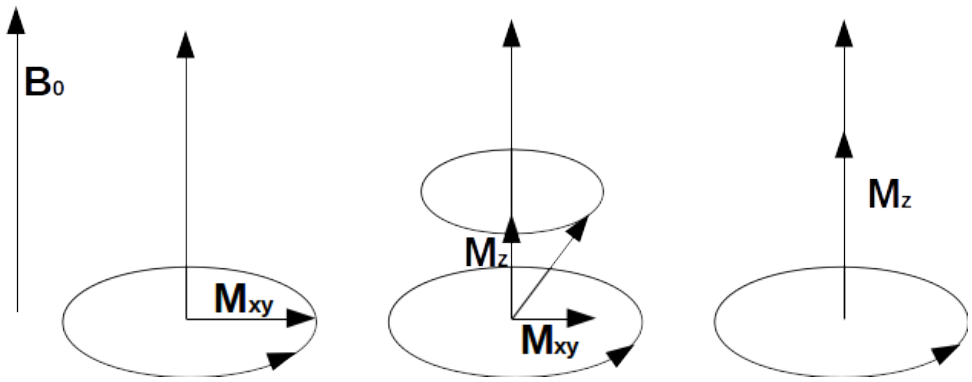

Figure 2.3: Schematic representation of the longitudinal relaxation after the RF pulse.

scribed in Figure (2.3). During this process the MR signal will gradually fade away. The z-component growth during the relaxation is represented by the exponential function (only valid for a RF pulse of 90 degrees):

$$M_z = M_0 \left(1 - \exp(-t/T_1)\right), \tag{2.20}$$

where $M_0 = |\boldsymbol{M_0}|$ and T_1 is the time necessary for M_z to reach $0.63 \times M_0$. T_1 is called longitudinal relaxation time constant, or spin-lattice relaxation time constant.

T_1 tends to be large in solids (slow relaxation) where molecules are less likely to be rotating at a rate near the Larmor frequency, while it is shorter in tissue where water is partially bound to large molecules such as proteins, and it is normally shortest in fat (McRobbie et al. [2017]).

After the excitation some of the spins precess coherently but this phase coherence is gradually lost due to spin-spin interactions. The different phases are the reason behind the transverse relaxation as the individual magnetization vectors cancel each other instead of adding together (see Figure (2.4)). The xy

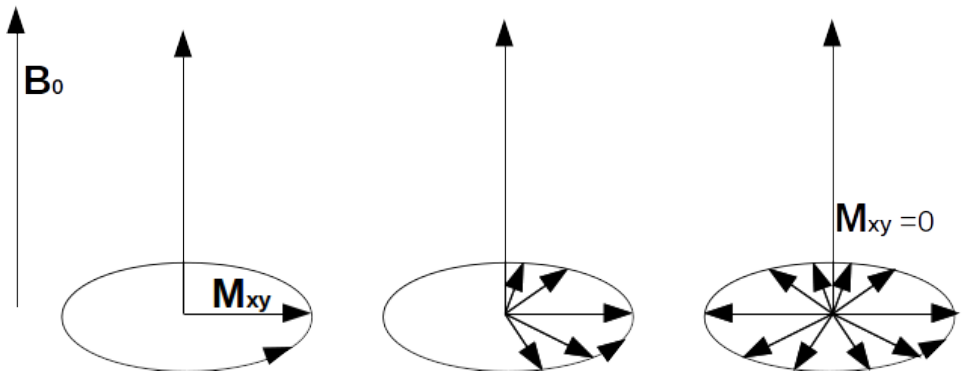

Figure 2.4: Schematic representation of the transverse relaxation after the RF pulse.

magnetisation, M_{xy}, decays exponentially with time constant, T_2, is represented by:

$$M_{xy} = M_0 \exp(-t/T_2), \tag{2.21}$$

where T_2 is the time required for M_{xy} to decay to $0.37 \times M_0$.

T_2 is short (fast relaxation) for proteins and lipids and increases with increasing water content. Such decay occurs in a perfectly homogeneous $\boldsymbol{B_0}$, however, in reality this is never the case. Therefore, additional de-phasing is caused by the variation in the field. The time constant for the decay, from both intrinsic de-phasing and de-phasing from field inhomogeneities, is T_2^* and it is shorter than T_2 (McRobbie et al. [2017]).

2.2.3 Image Formation

To produce MR images, the raw data is organised to spatially locate the signal in a matrix. To do so, a spatial encoding technique, based on magnetic field gradients, is used. To select a slice the main magnetic field is made inhomogeneous

along the z direction by using a gradient coil. In this way the magnetic field strength varies along the z-axis. As a consequence of this gradient, the Larmor frequency will change along the axis, and therefore, each slice is excited by applying a different RF pulse. According to the gradient direction the excitations can be restricted to a specific plane that can be transverse, sagittal, coronal or oblique (Weishaupt et al. [Berlin, 2008]). From Figure (2.5), it can be seen that a stronger gradient is able to select a thinner slice.

A single signal, however does not give enough information to reconstruct an entire MR image and it is necessary to acquire multiple signals in the directions that are orthogonal to the slice selection. This is the spatial encoding, and it comprises phase encoding and frequency encoding, which are done by mean of gradients in the orthogonal direction to the slice selection. The phase encoding gradient is applied to one orthogonal direction (for example y) and the result of this gradient is that along this direction the spin have different phases. As a consequence, each line of the slice is characterised by a different phase. The frequency encode gradient is applied in the third direction (x-direction) and the result is a change of the Larmor frequency along this direction. In this way every column in the slice is associated with a specific frequency. The spatial encoding allows to selection of all the combinations of phase and frequency and each combination represent a unique voxel (see Figure (2.6) for a schematic representation of the three encoding directions). The description of the slice selection and spatial encoding given here represents the simplest gradient-echo MR imaging sequence (McRobbie et al. [2017]).

The MR signal is acquired during the frequency encode gradient and after the phase-encoding, and the whole sequence pattern needs to be repeated for

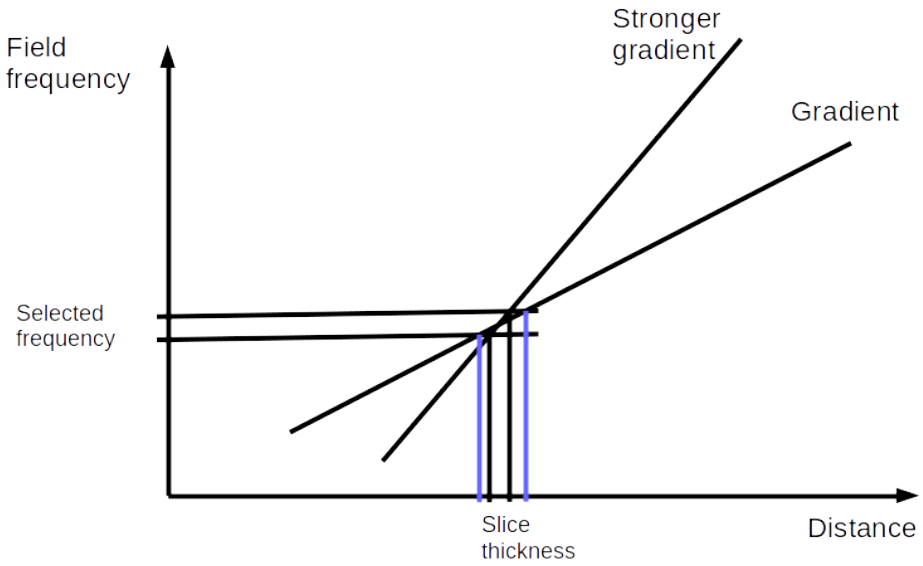

Figure 2.5: Schematic representation of the MR slice selection.

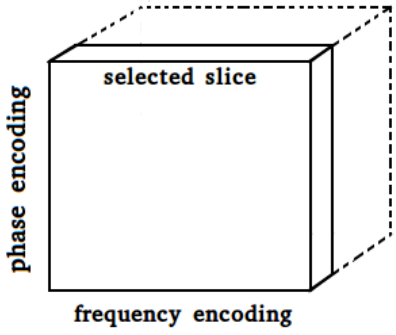

Figure 2.6: Schematic representation of the MR spatial encoding.

every 'line' of data in the K-space. The K-space is an array representing spatial frequencies, k_x and k_y. Once all the data are acquired, a Fourier transform is applied to convert the raw data into an MR image.

2.3 Basis of Hybrid PET-MR Imaging

2.3.1 Motivation

Since the advent of the first hybrid positron PET-CT scanners, the idea of combining PET and MR scanners has been a matter of discussion (Townsend [2008]; Beyer et al. [2000]; Zaidi et al. [2007]). As discussed by Disselhorst et al. [2014] and Musafargani et al. [2018] the rationale behind this was that the high contrast in soft tissue provided by MR would allow a more accurate localisation of the high uptake PET region and with the benefit of avoiding the CT radiation dose. In addition, MR can deliver anatomical information as well as complementary functional information that can be obtained via diffusion, perfusion, spectroscopy and so on. Furthermore, MR gives the ability to detect motion and thus, it can be used for motion correction. Finally, one of the driving forces in the initial development of PET-MR scanners was the reduction of the positron range in a magnetic field of the MR scanner. In fact, the distance positrons travel before annihilation is reduced in the direction orthogonal to the magnetic field. As a result, improved in-plane resolution can be obtained and it is proportional to the field strength.

2.3.2 Challenges in PET-MR Imaging

Despite all the aforementioned benefits related to PET-MR, important difficulties needed to be tackled. Some of these issues, such as attenuation correction, are still a matter of ongoing research (Delso and Nuyts [2018]). The most important issue related to simultaneous PET-MR acquisition was the fact that the PET and the MR systems can have mutual interference. For example, since the beginning of PET technology, photomultiplier tubes (PMTs) were the gold standard for the detectors. Nevertheless, such detectors were particularly sensitive to magnetic field, making the realisation of the PET-MR scanners very difficult. The development of human PET-MR systems for simultaneous PET and MR acquisition has been connected with the MR compatible solid state photodetectors such as avalanche photodiodes (APDs) (Pichler et al. [1997]; Catana et al. [2006]; Renker [2007]; Britvitch et al. [2007]; and Schulz et al. [2009]). This technology, however, presents low signal gain, high temperature dependance and a time resolution of the order of the ns which is not sufficient for time-of-flight (ToF). The application of Silicon photomultipliers (SiPMs) to PET was discussed by Roncali and Cherry [2011]). These devices represent the ideal tools as they are essentially insensitive to large magnetic fields and have higher temporal resolution than APDs.

Another major challenge for PET-MR is attenuation correction (Mehranian et al. [2013]; Mehranian et al. [2016]; Catana et al. [2018]). In fact, the MR signal is generated by the NMR related to proton concentration which is not related to the attenuation of gamma rays and as a consequence, direct evaluation of the linear attenuation coefficient is not possible with integrated PET-MR scanners. Different attenuation correction (AC) techniques have been proposed and some

of them are discussed by Hofmann et al. [2011] and Bezrukov et al. [2013]. These techniques can be classified in three categories:

- Segmentation-based methods: Tissue classes are segmented from the MR image and a uniform attenuation coefficient is assigned to each class, an example was proposed using ultra short echo time by Keereman et al. [2010];
- Population-based methods: use data from many patients to create an atlas (Hofmann et al. [2008]) or a training sample for machine learning (Liu et al. [2017]); the attenuation map is predicted by deforming a single template image to adapt it to the individual anatomy of the patient;
- Data-driven methods: these use the information from the PET data to create the attenuation map as proposed for example by Nuyts et al. [1999] and Mehranian and Zaidi [2015].

In brain imaging, the cranial bone has an important impact on attenuation of radioactivity in the brain. In particular, a high amount of photons will interact with the bone leading to a high number of photons being absorbed. For this reason, it is extremely important to estimate the bone attenuation coefficient. The MR image, in general, does not show signal in the bone because of its short relaxation time T_2. Ultrashort echo time sequences allow signal from the bone and segment this into tissue classes to create the attenuation map. Fine regions, such as, nasal cavities and cerebrospinal fluid are nonetheless commonly misclassified. For whole-body imaging, AC can be more difficult because the ultrashort echo time sequences are too time demanding to be applied for this purpose, and due to the smaller field of view (FoV) of MR, the estimated attenuation map can show

truncation artifacts Nuyts et al. [2013]. On the other hand, the impact of bone attenuation is not as significant as in the brain. A segmentation-based technique that separates air, lungs, fat, and soft tissue was proposed by Martinez-Möller et al. [2009] which is currently the most used technique. Such a technique is also the one implemented in the Siemens Biograph mMR, which is the PET-MR scanner mostly used in this thesis. In general, the technique that should be applied for AC varies depending on the application and the associated accuracy needed (Bezrukov et al. [2013]). For instance, segmentation-based methods without a bone tissue-class may be sufficient for standard clinical whole-body PET-MR imaging. Nonetheless, for quantitative PET applications such as bone tumours or bone marrow imaging, the bone tissue cannot be ignored without a loss of accuracy. For this reason, atlas and machine learning algorithms are beneficial for these studies. In brain imaging applications, consideration of bone is mandatory to have acceptable accuracy and it is implemented in all methods for brain MR AC. Nowadays, atlas and machine learning techniques have been shown to provide higher accuracy than segmentation-based methods (Torrado-Carvajal et al. [2018]).

2.3.3 MR-driven Reconstruction Algorithms

One of the limitations of PET is the low resolution it provides. Because of this, PET images are affected by the PVE which causes severe accuracy degradation, especially for small regions. Based on the assumption that the radiotracer uptake distribution follows specific anatomical patterns, the anatomical information can help to promote smoothness within a tissue region while preserving edge formation. Anatomically-driven algorithms have been proposed to correct

the PVE in PET. Several studies have recently implemented and investigated different anatomically-driven techniques, showing improvements in accuracy and precision while preserving the resolution that is usually lost through the regularisation process. Some of these method were applied after reconstruction (Müller-Gärtner et al. [1992]; Rousset et al. [1998]; and Silva-Rodríguez et al. [2016]), while in other techniques, the anatomical information is modelled into the iterative process. For the latter case, the anatomical information was initially included in a prior distribution using Bayesian techniques, which can be classified into segmentation-based (Bowsher et al. [1996]; and Baete et al. [2004]) and segmentation-free techniques (Somayajula et al. [2011, and references therein]; Tang and Rahmim [2009]; Bai et al. [2013]; and Jiao et al. [2015]) where the latter avoids the potential error in segmentation. In particular, some of these techniques were also thought to include mutual information from the anatomical and functional images: Wells et al. [1996] used the mutual information to propose a registration method for images of different modalities, while Rangarajan et al. [2000] used the information to create a Bayesian prior for functional image reconstruction. Nuyts [2007] showed that these approaches lead to bias when there are differences between the anatomical and functional images, and demonstrated that the joint entropy is a more flexible method in these circumstances.

More recent studies have proposed a different approach to introduce prior information. Such techniques benefit from the machine learning theory which goes under the name of the kernel method (Hoffman et al. [2008]). Hutchcroft et al. [2014] and Wang and Qi [2015] introduced this technique in PET image reconstruction using one prior information image, MR and PET respectively, to regularise reconstruction, and showing better performance than a wide set of

Bayesian techniques. Novosad and Reader [2016] used the kernel method combined with temporal basis functions in order to perform full dynamic PET reconstruction. Ellis and Reader [2016] proposed the use of kernelised expectation maximisation (KEM) in the context of dual-dataset longitudinal PET studies, where a baseline scan reconstruction was used to define basis functions for a follow-up scan reconstruction. Gong et al. [2018a] used a hybrid kernel method to perform direct reconstruction of Patlak plot parameters from dynamic PET using MR and PET information, where the latter was obtained by combining different frames. The first relies only on the MR image which can create PET feature over-smoothing or artifacts, while the second only relies on PET, which already contains PVE, and further it needs preliminary PET reconstructions. The main focus of this thesis is the implementation and investigation of a novel hybrid image reconstruction algorithm for accurate low-count imaging. The proposed method is an iterative reconstruction algorithm making use of the kernel method. In particular, the main novelty is that synergistic PET-MR information is included in the iterative process. This will be discussed in detail in the following chapters.

2.4 Software for Tomographic Image Reconstruction

The main software library that will be used for this thesis is the software for tomographic image reconstruction (STIR) (Thielemans et al. [2012]) is an object-oriented library based on C++; it provides classes and utilities for SPECT and PET image reconstruction, image and sinogram manipulation, estimation of cor-

rection sinograms, analytical simulation and image analysis.

STIR contains a number of 2D and 3D reconstruction algorithms, such as analytic, iterative and anatomically-driven (Jacobson et al. [2000]; and Bettinardi et al. [2002]). The hierarchy of the library is characterised by inheritance which allows each class to reuse the attributes and behaviour of the ancestor classes without repeating part of the code that is common to different classes. Figure (2.7) shows the class hierarchy for the image reconstruction algorithms, OSMAPOSLReconstruction, which is widely used in this project and a derived class, called KOSMAPOSL, described in Appendix B, was implemented to incorporate the kernel functionalities.

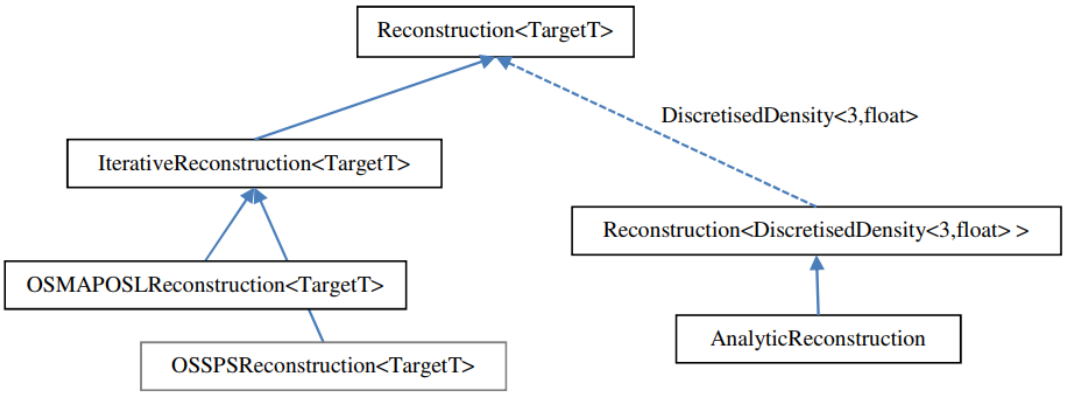

Figure 2.7: Class hierarchy for the reconstruction algorithms (Thielemans et al. [2012]).

The OSMAPOSLReconstruction allows use of many algorithms, such as MLEM, OSEM and standard priors like MRP and QP and the anatomically-guided PLS (implementated by the candidate during this project) via the use of different ob-

jective functions for motion correction, LM reconstruction and so on. All these algorithms make use of forward and backward projection operations which are implemented in STIR, as described by Thielemans et al. [1999].

The reconstruction requires the correction sinograms to be estimated. For every dataset in this thesis, these sinograms have been estimated as follows:

Attenuation: is estimated using the formula, e^{-f_μ}, where f_μ is the forward projection of the attenuation coefficient image obtained from the scanner. The attenuation image has to be in units cm^{-1};

Normalisation: consists of multiplicative correction factors that are applied during the forward and backward projection operations. The procedures for these evaluations in STIR are done following Hogg et al. [2001] where, different components, such as geometric components, time window misalignment between blocks and crystal efficiency factors, were estimated using a maximum likelihood approach.

Randoms: are estimated from singles, which were calculated from delayed events using a maximum likelihood approach (Jacobson and Thielemans [2008]).

Scatter: it is performed as described by Tsoumpas et al. [2004] and discussed in more detail by Polycarpou et al. [2011]. In particular, the scatter sinogram is estimated using an upgraded version of the Watson single scatter simulation algorithm from a down-sampled attenuation image and sinogram; the sinogram is then interpolated to match the data sinogram, and finally it is rescaled using tail-fit in order to account for multiple scatter and events outside the field of view (Thielemans et al. [2007]).

Chapter 3

Quantitative Performance of Standard Iterative Reconstruction Techniques for Low-count PET-MR Data

In the previous chapter the theory behind PET image reconstruction was discussed, and the background required to understand the standard techniques were introduced. In this chapter, the standard methods are assessed and compared for low-count circumstances, which are obtained by using short frames. In this way, an example of the limitations of such algorithms with real data is given before the introduction of the proposed MR-driven method. This chapter does not claim to propose a novel methodology but to introduce the standard reconstruction algorithm performance using low-count real data for the Biograph Siemens mMR.

3.1 Introduction

As already mentioned in the previous chapter, most of the algorithms used for PET image reconstruction are based on the same concept as the MLEM algorithm. The accelerated version of MLEM, called OSEM, which divides the datasets in balanced ordered subsets of projection data (Hudson and Larkin [1994]), is widely used in the clinical practice with PET studies, because it is easily implemented and provides good images using a small number of iterations. Other algorithms are available, such as OSMAPOSL where the posterior density, which includes prior information, is maximised rather than the likelihood. These iterative algorithms are all implemented in the STIR library (Thielemans et al. [2012]) making it possible to perform a comparative study as a simple task. The aim of this investigation is to study real data with the standard techniques implemented in STIR for the Siemens Biograph mMR for low-count datasets. The algorithms under investigation are MLEM, OSEM, OSMAPOSL-QP and OSMAPOSL-MRP. For simplicity OSMAPOSL-QP and OSMAPOSL-MRP will be referred to as QP and MRP, respectively. Their performances were assessed in terms of different figure of merits on single time frame and for ten replicates.

3.2 Methods and Material

3.2.1 Phantom Data

The data used in this study were acquired with a Siemens Biograph mMR scanner at University College London Hospital. This scanner, described in detail by Delso et al. [2011], has 8 rings, each one divided into blocks of 56 lutetium oxyorthosilicate (LSO) crystals (each crystal: $4{\times}4{\times}20$ mm^3). The axial field of view is 258 mm. The Hoffman 3D Brain Phantom (Hoffman et al. [1990]) was used, which can provide a realistic approximation of the radioisotope distribution found in the normal brain. The phantom consists of a robust plastic cylinder (Diameter: 20.8 cm, Height: 17.5 cm, Fillable volume: ~ 1.2 l) and 19 independent plates within the cylindrical phantom. It was filled with 60 MBq ^{18}F-FDG and the acquisition time was 3600 s. The total number of events (prompts) including random and scatter is about 10^9, which represents a standard for brain acquisitions. The LM file was then partitioned into 10 time frames, so as to obtain datasets with lower number of counts. The latter was obtained by selecting time frames, of about 36 s, when creating the sinogram with STIR. The duration of each time frame is calculated to take into account the decay rate and to give approximately the same expected number of events for each replicate. Hence the time window is calculated as follows:

$$\Delta t_n = t_n - t_{n-1} \qquad n = 1, \ldots, 10 \tag{3.1}$$

where n represent the sample, $t_0 = 0$, $t_1 = 36\ s$, and where

$$t_n = -\tau \ln\left(n\left(\exp(-\frac{t_1}{\tau}) - 1\right) + 1\right) \qquad n = 1, ..., 10 \tag{3.2}$$

is the time reached at the n^{th} time frame and τ is the reciprocal of the decay constant, λ, for ^{18}F.

3.2.2 Reconstruction Setup

The data were reconstructed with different ordered subsets iterative algorithms. For OSEM, 3, 9, 21 subsets were used, to study whether the choice of the number of subsets affects the reconstructed image. With the other algorithms 21 subsets and 5 complete iterations (hence a total of 105 sub-iteration) were used. Post-filtering using an isotropic Gaussian filter (FWHM = 5 mm) allows noise reduction for OSEM. In the clinic, 3 iterations for 21 subsets are usually used, however, 5 is chosen here because the value of each ROI reached a plateau at this iteration. The Bayesian algorithms include a regularising parameter, β, which must be chosen. Several β values, 0.5, 5, 10, 25, 50, 100, 500 and 1000 were compared for both QP and MRP, described in Section 2.1. Firstly, the Euclidean distance of the points, in the plots from Figure (3.2(b)), was calculated from the origin. The distance, D, of the points can also be seen as a modified version of RMSE where bias and variance are normalised by the ROI mean:

$$D = \sqrt{bias^2 + CoV^2}. \tag{3.3}$$

Secondly, the sum of the distances (SOD) of each ROI was calculated as follow:

$$S_D = D_w + D_g, \tag{3.4}$$

where D_w is the distance calculated for the 'white matter' and D_g for the 'gray matter'. Finally, the best trade-off was chosen as the smallest SOD. The im-

age size after the reconstruction is 289×289×127 with voxel size 2.04×2.04×2.03 mm^3. STIR 3.0 was used both for reconstruction and for all corrections (attenuation, scatter, normalisation and randoms).

3.2.3 Image Analysis

The image reconstructed with 126 iterations of MLEM (126 was the iteration number where the mean value of the ROIs had reached a plateaux) using the 3600 s acquisition data was used as a reference for the bias formula. The choice of the 3600 s as the 'true' image is due to the fact that images reconstructed from low count data are biased (Walker et al. [2011]), and the closest to the 'truth' is the image reconstructed from the long acquisition. To analyse the images, circular regions of interest (ROIs), were used. Six circles with 6 mm radius, each one positioned across three different slices, were located in a way that three circles lay within the 'gray matter' and the other three in the 'white matter' as shown in Figure (3.1). The analysis was carried out considering the three circles as one ROI for each tissue. For every ROI, the bias and CoV were calculated and used to study how the various reconstruction methods differ from MLEM, and to assess the variability in the ROIs. Corrections were performed as described in Section 2.4. For every ROI the bias and CoV were calculated and used to study how the various reconstruction methods differ from the gold standard, and to assess the variability in the ROI. The following formulas represent bias and CoV for each region:

$$\text{bias} = \frac{t - M_T}{M_T} \times 100, \tag{3.5}$$

$$\mathrm{CoV} = \left(\frac{\sqrt{\frac{1}{V-1}\sum_{j=1}^{V}(t_j - t)^2}}{t} \right) \times 100, \tag{3.6}$$

where M_T is the mean value of the gold standard, t is the mean value within the ROI, j the voxel index, t_j denotes the value of the single voxel j inside the ROI and V represents the number of voxels inside the three circles.

(a) (b) (c)

Figure 3.1: Regions of interest chosen for this study in different slices. The red ROI is for 'gray matter' and the blue one for 'white matter'.

To ensure exactly equal experimental conditions, ten samples with roughly the same number of counts were created, by sub-sampling from the 3600 s data, so as to mimic 36 s acquisition times and to allow assessment of reconstruction repeatability. The effective acquisition time was reduced from 3600 s to 36 s in order to simulate low-count datasets. Voxel-wise analysis was also performed on the low-count reconstructed images, using standard deviation (SD) over time frames, SD_t, bias and RMSE to quantify respectively accuracy, repeatability and the trade-off between the two.

In general, to define a general quantitative analysis design, suppose that K

replicate datasets are available, $\{Y^k : k = 1, \ldots, K\}$ and that the corresponding result of the algorithm are estimated radiotracer concentration images $\{\widehat{\Lambda}^k : k = 1, \ldots, K\}$. These can be used to define a mean image, $\bar{\Lambda} = \sum_{k=1}^{K} \widehat{\Lambda}^k / K$. Further, recall that a 'gold standard', Λ^* is available from the 3600 s dataset reconstructed using the MLEM algorithm. The SD_t, bias and RMSE are then defined as follows:

$$SD_t = \sqrt{\frac{1}{K-1}\sum_{n=1}^{K}(\widehat{\Lambda}^k - \bar{\Lambda})^2}; \quad \text{bias } = \bar{\Lambda} - \Lambda^*; \quad RMSE = \sqrt{SD_t^2 + \text{bias}^2}. \tag{3.7}$$

The ideal reconstruction algorithm would produce low values for each of these measures indicating high reproducibility from the replicate datasets and lack of overall bias.

3.3 Results

Convergence of the algorithms was studied by plotting the bias as a function of the number of iterations. Figure (3.2(a)) shows, for OSEM, the percentage bias and CoV for different subsets and number of iterations with the CoV represented by the bars. Such a study represents a preliminary investigation to investigate the quantitative effect of the number of subsets and the number of iterations. The penalty factor for the OSMAPOSL methods was optimised in order to find a reasonable trade-off between bias and CoV. In Figure (3.2(b)) the results of this optimisation study were shown and the chosen β values are listed in Table (3.1). Figure (3.2(c)) represents a comparison between the optimised algorithms in terms of bias and coefficient of variation (CoV) (bars), for each method and

ROI. Figure (3.3), shows the reconstructed phantom images for the 3600 s and 36 s reconstructed images with OSEM and the images obtained from the optimised OSMAPOSL algorithms for the low-count case. The SD_t was evaluated for these ROIs over the samples and the results showed that optimisation also helps to reduce the variability over samples, which is 9% for 'gray matter' and 24% for 'white matter', whilst in the worst case scenario, i.e. OSEM with no post-filtering, is 61% and 90%.

Table 3.1: Optimised β values for MAP algorithms for the 36 s frames.

	β values (36 s)
QP	1000
MRP	500

The results of the statistical investigation with the 36 s dataset over the

Gray Matter

	OSEM	OSEM+G	QP,β=100	QP,β=1000	MRP,β=100	MRP,β=500
mean	2.47 ± 0.59	2.39 ±0.12	2.47 ±0.26	2.39 ±0.15	2.49 ±0.21	2.42 ±0.16
SD_t	1.53 ±0.44	0.22 ±0.05	0.67 ±0.13	0.22 ±0.05	0.50 ±0.1	0.23 ±0.05
bias	0.41 ±0.36	0.22 ±0.15	0.25 ±0.18	0.22 ±0.15	0.25 ±0.18	0.23 ±0.16
RMSE	1.61 ±0.48	0.33 ±0.12	0.74 ±0.14	0.33 ±0.12	0.59 ±0.13	0.34 ±0.12

White Matter

	OSEM	OSEM+G	QP,β=100	QP,β=1000	MRP,β=100	MRP,β=500
mean	0.55 ±0.25	0.61 ±0.07	0.55 ±0.17	0.57 ±0.09	0.56 ±0.09	0.62 ±0.07
SD_t	0.57 ±0.35	0.14 ±0.03	0.38 ±0.13	0.14 ±0.03	0.17 ±0.04	0.08 ±0.02
bias	0.16 ±0.13	0.14 ±0.08	0.11 ±0.08	0.10 ±0.07	0.09 ±0.06	0.13 ±0.09
RMSE	0.61 ±0.35	0.20 ±0.06	0.41 ±0.13	0.17 ±0.05	0.20 ±0.05	0.16 ±0.07

Table 3.2: Summarised results using three circular ROIs per tissue, spread over gray and white matter. The numbers represent the averaged voxel value over all the voxels inside the ROI with the relative SD over the voxels within the ROI. The SD_t row, on the other hand, is a measure of the variability over the 10 samples used.

ten replicate datasets are represented in Figures (3.4) and (3.5). These show a

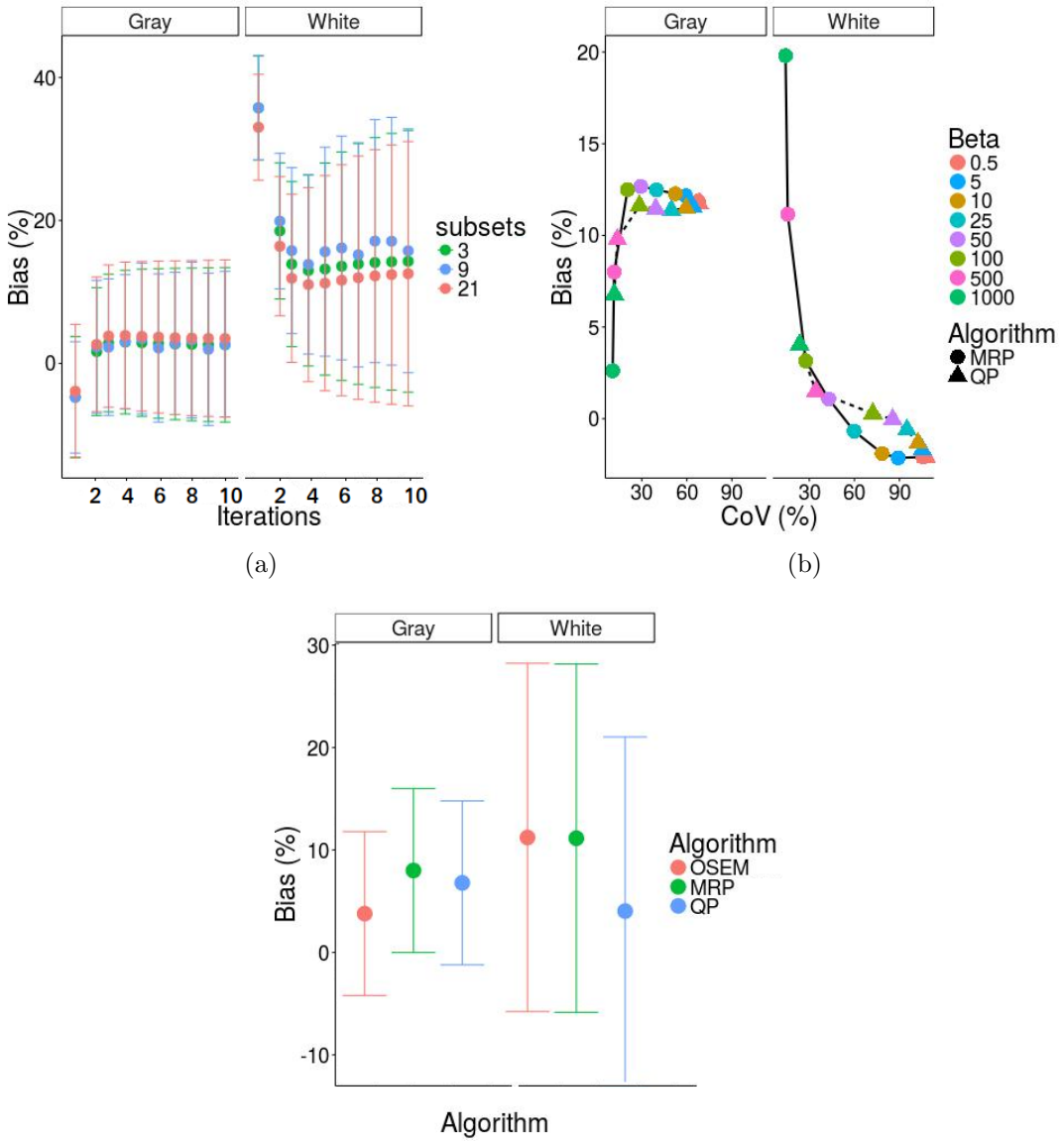

(a) (b)

(c)

Figure 3.2: Results for one of the ten 36 s frames: (a) shows the behaviour of the bias and CoV (represented by bars) as a function of the number of iterations. In addition, it shows the effect of the number of subsets for 'white matter' and 'gray matter'; (b) bias-CoV trade off for QP and MRP for several β values in the two penalised algorithms; (c) shows bias and CoV for the images obtained with OSEM, QP and MRP, where the β value is the one with the best bias-CoV trade-off.

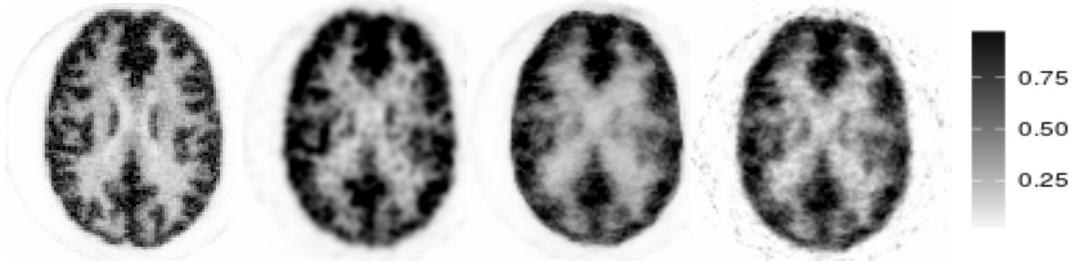

(a) (b) (c) (d)

Figure 3.3: Transverse phantom view for images reconstructed with 21 subsets at the 5th iteration: (a) 3600 s reconstructed image with OSEM; 36 s reconstructed images with: (b) OSEM + 5mm Gaussian filter; (c) MRP, β=500, and (d) QP, β=1000.

single dataset reconstruction (Sample), mean, SD_t, bias and RMSE images for 6 different cases. Figure (3.4) shows the OSEM corresponding image, the image after the Gaussian smoothing post-processing, then the OSMAPOSL estimations using QP with $\beta = 100$. Figure (3.5) shows the remaining results for QP with $\beta = 1000$ and then MRP with $\beta = 100$ and finally $\beta = 500$. The values of the prior parameters were chosen to give a range of reconstruction quality, and they were chosen based on the results from Figure (3.2(b)). The SD_t shows the variability over different samples, indeed the OSEM and OSMAPOSL estimates with small prior parameter have SD is very high. Using a filter for OSEM to produce the OSEM+G estimate, and higher prior parameter for MAP estimation, help reduce the SD_t and the higher the parameter the lighter are the SD_t images. Table (3.2) shows the mean voxel values for two ROIs, representing 'gray' and 'white' matter. Each ROI is obtained as described in Section 3.2.3. The mean, SD_t, bias and RMSE values are calculated from the images showed in Figure (3.4) and (3.5).

3.4 Discussion

The purpose of this chapter was to investigate the feasibility of image reconstruction when short acquisition time is used, and compare the performances of various iterative algorithms in this situation. The study assessed the consequences on image quantification also giving a measure of the reproducibility of the results. Figure (3.2(a)) shows that 21 subsets can be used without significant impact on the quantification. The optimum β value was chosen as the best trade-off between bias and CoV among a set of different β values. The images reconstructed with the optimum β (see Table (3.1) are compared in Figure (3.2(c)). Note that a possible way to choose the regularisation parameter is represented by the L-curve described in Hansen [1999] which displays the trade-off between the size of a regularised solution and its fit to the given data, as the regularization parameter varies. The comparison shows that the region with lower uptake have also higher bias and CoV except for the QP which has smaller bias for the 'white matter' than the 'gray matter'. In addition, QP gives the best results for both ROIs compared to MRP and OSEM.

From Figure (3.3) it is possible to notice the loss of resolution and contrast in the 36 s images compared to the 3600 s images. This preliminary results, however represents the analysis performed with only one time frame. A more complete analysis was carried out with ten samples. In this case, the same algorithms were compared by estimating the mean image, bias image, SD image and RMSE image to show the quantification results under a voxel-wise level. The mean images from Figure (3.4) and (3.5) show the improved quality when combining the information from all the 10 samples, however the image that one would look at after a low-count acquisition is the sample image. The images from OSEM, QP, with

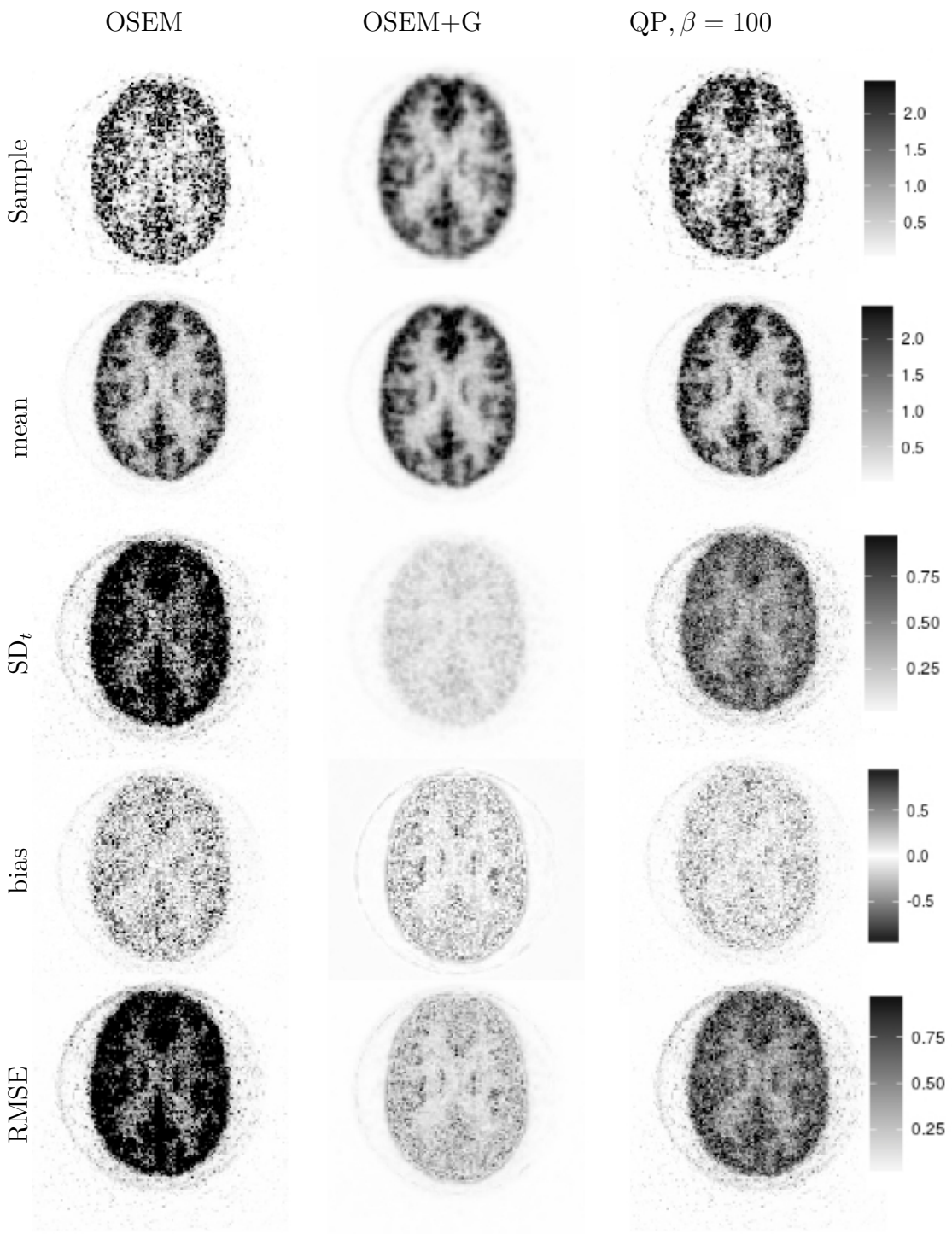

Figure 3.4: Transverse view of images reconstructed with 21 subsets at the 5^{th} iteration: 36 s acquisition.

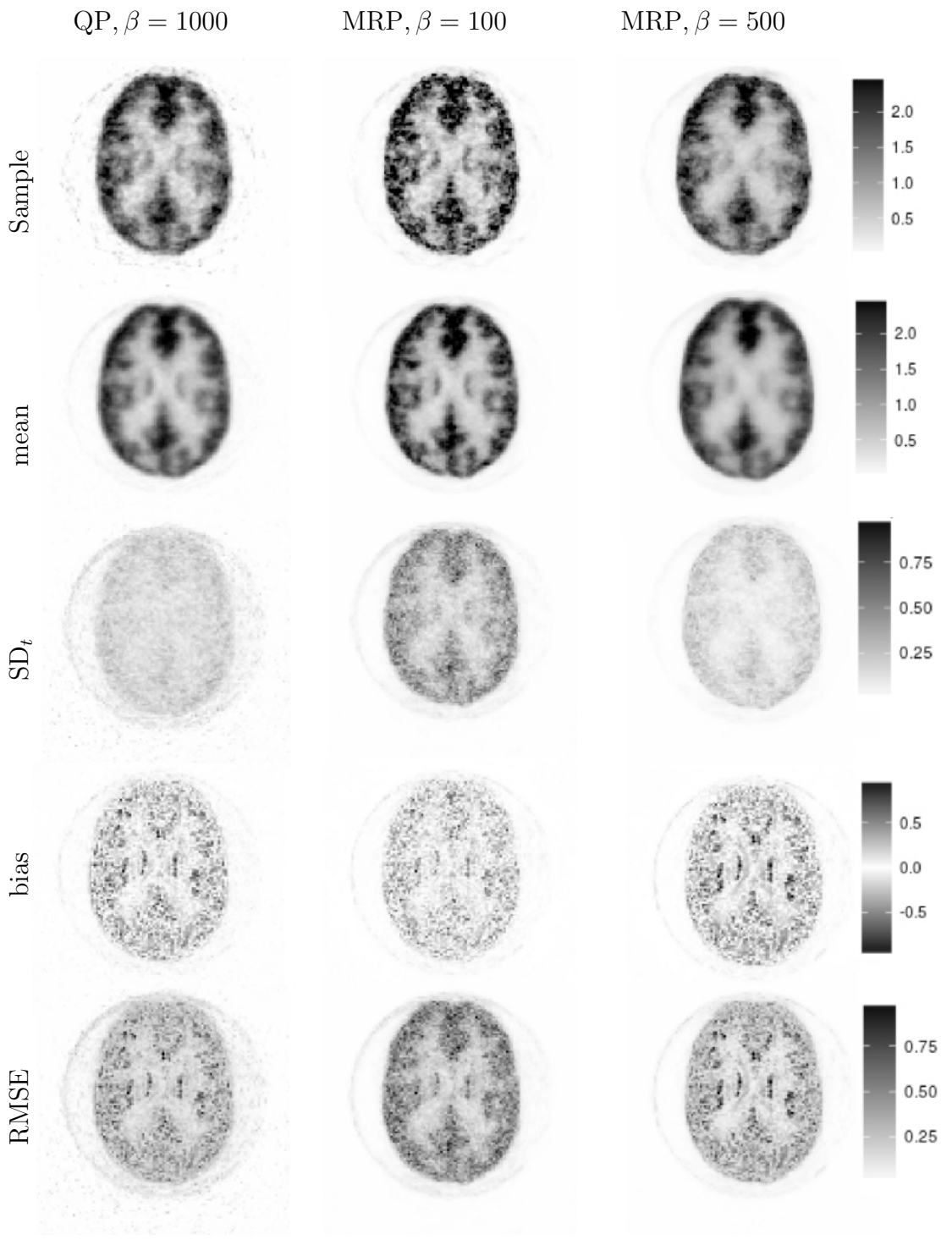

Figure 3.5: Transverse view of images reconstructed with 21 subsets at the 5^{th} iteration: 36 s acquisition.

β=10, and MRP, with β=10, have very high RMSE although it decreases with higher prior parameter values. The best values for 'Gray' Matter, 0.33, 0.33 and 0.34 are reached with the post-filtered OSEM, QP-β=1000 MRP-β=500, whilst for 'White Matter' are 0.16, 0.17 and 0.20 which correspond to MRP-β=500, QP-β=1000 (see Table (3.2). From Figures (3.4) and (3.5) it is possible to appreciate how the use of regularisation helps to reduce noise, to improve precision over samples, and, in the inner regions of 'Gray' and 'White' matter, to reduce the bias. Nevertheless, from the bias and RMSE images it is evident how this improvements come at the cost of PVE, especially when one looks at small regions and borders between different tissues. From a global perspective, improved reconstructed images can be achieved by a careful choice of the regularisation parameter, however, low-count reconstructed images always showed high noise and bias with all the investigated algorithms illustrating the limitation represented by the standard techniques. In addition, the performance of OSEM with Gaussian post-filtering was shown to be sufficiently good if compared to QP and MRP, which are difficult to optimise. This is the reason why Bayesian techniques were not translated to the clinic until the recent study by Ahn et al. [2015], which aims at the translation of the Bayesian reconstruction algorithm using the relative difference prior. Ahn et al. [2015] have demonstrated that regularisation with more advanced prior distribution can significantly improve quantification and detectability compared with post-filtered OSEM. Anatomical information from CT or MR is an important point to consider in the development of hybrid reconstruction methods as it helps to preserve anatomical borders and avoid PVE (Somayajula et al. [2011]; and Ehrhardt et al. [2016]).

3.5 Conclusions

The objective of the study was to compare the performances and limitation of various iterative algorithms when short acquisition times are used. Different β values were compared, for the Bayesian techniques, showing that improved reconstruction can be achieved by a careful choice of the prior parameter, although the loss of fine details still represents an issue to be solved. The work in this chapter was part of the research training on studying and comparing existing reconstruction algorithms within the STIR framework. As a consequence, the contents do not represent novel methodologies, although, it was the first quantitative study using STIR for the reconstruction of low-count datasets obtained from data acquired with the Biograph Siemens mMR.

Chapter 4

Introduction and Validation of LM-HKEM

In the previous chapter the performance of iterative algorithms under low-count circumstances was investigated. In this chapter a novel iterative algorithm, HKEM, is introduced with the aim of improving all the issues encountered in the previous chapter and improving quantification at different count-levels. Section 4.1 gives an introduction to the existing MR guided techniques, highlighting the novelty of HKEM, and the purpose of the method. Section 4.2 describes the mathematical aspects of the hybrid kernelised reconstruction algorithm. Section 4.3 describes the datasets used to study image reconstruction, LM sub-sampling and the experimental methodology. Section 4.4 presents results and a comparison of the different standard algorithms with the proposed algorithm. The results are discussed in Section 4.5 and conclusions are drawn in Section 4.6.

4.1 Introduction

Since the introduction of hybrid scanners, such as PET-CT and PET-MR, several anatomically-driven reconstruction methods have been proposed to better exploit the dual information provided by these scanners. There are different ways of introducing anatomical information into the iterative reconstruction. The most common is based on the Bayesian approach where instead of maximizing a Poisson density function, the posterior density function is maximised. These techniques have shown promising results in terms of image quality and quantification (Vunckx et al. [2012, and references therein]; and Ehrhardt et al. [2016]) To exploit the fact that PET-MR scanners allow the acquisition of PET and MR data simultaneously, synergistic reconstruction of these two has also been investigated in order to improve the quality of both PET and MR images (Ehrhardt et al. [2014]; Knoll et al. [2017]; and Mehranian et al. [2018]).

Most recently, another approach to include prior information was introduced based on the kernel method, which is commonly used in machine learning (Hoffman et al. [2008]). The technique was first applied to PET image reconstruction by Hutchcroft et al. [2014, 2016] and Wang and Qi [2015]. In these studies a single prior information image, MR or PET, was used to regularise reconstruction. Novosad and Reader [2016] used the kernel method combined with temporal basis functions in order to perform full dynamic PET reconstruction. Ellis and Reader [2016] proposed the use of kernelised expectation maximisation (KEM) in the context of dual-dataset longitudinal PET studies, where a baseline scan reconstruction was used to define basis functions for a follow-up scan reconstruction. Gong et al. [2018a] used a hybrid kernel method to perform direct reconstruction of Patlak plot parameters from dynamic PET using

MR and PET information where the latter was obtained by combining different time frames. These previous studies were carried out using sinogram-based reconstruction. Bland et al. [2017] studied the effect of KEM on simulated dose-reduced datasets, showing improved contrast to noise ratio, but at the cost of possible over-smoothing of features unique to the PET data. To overcome this issue, Bland et al. [2018] proposed an MR resolution spatially constrained kernel method in order to maintain the noise reduction properties of the conventional kernel method, whilst better retaining the features unique to the PET data.

The work presented in this chapter proposes a novel iterative reconstruction technique to overcome the issues associated with low-counts discussed in the previous chapter, the problem of PET unique feature suppression reported in the previously mentioned studies using only the MR-based kernel, and to improve contrast of lesions at different count levels. This chapter explores the performance of the hybrid kernel method for LM reconstruction (LM-HKEM) of static images exploiting one MR image and the PET information, iteration after iteration. Such a procedure avoids the need for a preliminary reconstruction from PET data, as in Wang and Qi [2015]. The MR component is a constant part of the kernel which has to be chosen according to the type of study one wants to perform. The proposed method is designed to improve quantification with minimal PET unique feature suppression, while keeping good resolution and image quality, at various count-levels. Both LM-KEM and LM-HKEM in this study use a voxel-wise and spatially restricted kernel rather than a patch-wise kernel (Wang and Qi [2015]). The method performance was studied on four datasets: simulated torso, Jaszczak phantom and two patient studies showing plaques in the arteries. The method was compared with different algorithms

such as OSEM and OSMAPOSL with different priors.

4.2 Theory

The kernel method is a technique commonly used in machine learning (Hoffman et al. [2008]). It aims to find a short description of the data by taking advantage of what is called a training sample where 'structure' can be extracted. One of the most general ways to represent data is to specify a similarity between pairs of objects. Suppose to empirical data is available

$$(\boldsymbol{v}_1, w_1), ..., (\boldsymbol{v}_n, w_n) \in V \times W, \tag{4.1}$$

where V is the domain of the *inputs*, $\boldsymbol{v}_j$, and W is the domain of the *outputs*, w_j. The idea is to generalise for unseen data points. That is to say, given some new input $\boldsymbol{v} \in V$, one wants to predict the corresponding output, $w \in W$. In this case, the task is to predict the PET image of a subject, using PET data as well as information from an image of the same subject in a different modality (MR or CT).

The output, w_j, can be written as a function, F, of the input, $\boldsymbol{v_j}$

$$w_j = F(\boldsymbol{v_j}), \qquad j = 1, ..., N_j, \tag{4.2}$$

$F(\boldsymbol{v_j})$ is a high dimensional and non-linear function but it can be described linearly in a transformed space, $\{\boldsymbol{\Phi(v_j)}\}_{j=1}^{N_j}$,

$$F(\boldsymbol{v_j}) = \boldsymbol{\mu^T \Phi(v_j)}, \tag{4.3}$$

where N_j is the number of inputs used to estimate output j, $\boldsymbol{\Phi}$ is a vector mapping function and $\boldsymbol{\mu}$ is a weight vector also sitting in the transformed space with

$$\boldsymbol{\mu} = \sum_{l=1}^{N_j} \alpha_l \boldsymbol{\Phi}(\boldsymbol{v_l}), \tag{4.4}$$

where α_l is an element of the coefficient vector, $\boldsymbol{\alpha}$. At this point, it is clear how the outputs can be described as a linear function in a dot product space, called feature space, as

$$w_j = \sum_{l=1}^{N_j} \alpha_l \boldsymbol{\Phi}(\boldsymbol{v_l})^{\boldsymbol{T}} \boldsymbol{\Phi}(\boldsymbol{v_j}). \tag{4.5}$$

The dot product is a similarity measure in the space V and it defines the kernel, k

$$k : V \times V \to \mathbb{R}, \qquad (\boldsymbol{v_l}, \boldsymbol{v_j}) \mapsto k(\boldsymbol{v_j}, \boldsymbol{v_l}) \tag{4.6}$$

satisfying, for all $\boldsymbol{v_l}, \boldsymbol{v_j} \in V$, the following identity

$$k(\boldsymbol{v_j}, \boldsymbol{v_l}) = \langle \boldsymbol{\Phi}(\boldsymbol{v_l}), \boldsymbol{\Phi}(\boldsymbol{v_j}) \rangle . \tag{4.7}$$

The advantage of using a kernel as a similarity measure is that it allows construction of algorithms in dot product spaces without explicitly defining $\boldsymbol{\Phi}$. The kernel approach can be applied using the LM-OSEM reconstruction algorithm. For simplicity, the mathematical formulation of the algorithm is shown for 1 ordered subset. The LM-OSEM iterative update for a voxel, j, and sub-iteration,

$n+1$ is given by

$$\lambda_j^{(n+1)} = \frac{\lambda_j^{(n)}}{\sum_{i \in J_j} c_{ij}} \sum_{i=1}^{L} c_{ij} \frac{1}{\sum_{k \in I_i} c_{ik} \lambda_k^{(n)} + s_i}, \tag{4.8}$$

where $\lambda_j^{(n)}$ is the estimated j^{th} voxel value at the n^{th} sub-iteration and c_{ij} is the ij^{th} element of the system matrix. This represents the probability that an event occurring in voxel j produces a coincidence in the i^{th} pair of detectors, s_i is the additive sinogram containing scatter and random events, J_j is the set of projections that contribute to the value in voxel j, and I_i is the set of voxels that contribute to projection i.

Each voxel value of the image, $\boldsymbol{\lambda}$, can be represented as a linear combination using the kernel method. So, λ_j can be described using the kernel matrix

$$\lambda_j = \sum_{f=1}^{N_j} \alpha_f k_{fj}, \tag{4.9}$$

where k_{fj} is the fj^{th} kernel element of the matrix, $\boldsymbol{K}$, where N_j is the number of feature vectors used to estimate voxel j, typically one for every nearest neighbour allowed (50 in a 7×7×7 window in Wang and Qi [2015]). Different kernel functions are proposed in the literature, with the most used in medical imaging being the Gaussian kernel

$$k(\boldsymbol{v}_f, \boldsymbol{v}_j) = \exp\left(-\frac{\|\boldsymbol{v}_f - \boldsymbol{v}_j\|^2}{2\sigma^2}\right). \tag{4.10}$$

4.2.1 Kernel Matrix Construction

In contrast to previous work, where the kernel was created using either MR or PET images, or where the kernel method is used in conjunction with spectral temporal basis functions for dynamic PET reconstruction, here a LM hybrid kernel method that uses information from both MR images and PET update images is proposed. The PET image, used to construct the hybrid kernel, is helpful in tackling the mismatch problem between PET and MR. The dependency on the iterative process helps avoiding the need for a preliminary reconstruction to obtain the kernel. Taking into account the fact that the kernel is iteration dependent, the iterative step becomes the following

$$\alpha_f^{(n+1)} = \frac{\alpha_f^{(n)}}{\sum_{j=1}^{N_f} k_{fj}^{(n)} \sum_{i \in J_f} c_{fi}} \sum_{j=1}^{N_f} k_{fj}^{(n)} \sum_{i=1}^{L} c_{ij} \frac{1}{\sum_{l \in I_i} c_{il} \sum_{q=1}^{N_l} k_{ql}^{(n)} \alpha_q^{(n)} + s_i}, \quad (4.11)$$

with

$$k_{fj}^{(n)} = k_m(\boldsymbol{v}_f, \boldsymbol{v}_j) \cdot k_p(\boldsymbol{z}_f^{(n)}, \boldsymbol{z}_j^{(n)}), \quad (4.12)$$

where

$$k_m(\boldsymbol{v}_f, \boldsymbol{v}_j) = \exp\left(-\frac{\|\boldsymbol{v}_f - \boldsymbol{v}_j\|^2}{2\sigma_m^2}\right) \exp\left(-\frac{\|\boldsymbol{x}_f - \boldsymbol{x}_j\|^2}{2\sigma_{dm}^2}\right), \quad (4.13)$$

is the kernel coming from the MR image and

$$k_p(\boldsymbol{z}_f^{(n)}, \boldsymbol{z}_j^{(n)}) = \exp\left(-\frac{\|\boldsymbol{z}_f^{(n)} - \boldsymbol{z}_j^{(n)}\|^2}{2\sigma_p^2}\right) \exp\left(-\frac{\|\boldsymbol{x}_f - \boldsymbol{x}_j\|^2}{2\sigma_{dp}^2}\right), \quad (4.14)$$

is the part coming from the PET iterative update. The $\alpha_f^{(n)}$ is the kernel coefficient f estimated at iteration n, $\boldsymbol{x}_j$ is the coordinate of the j^{th} voxel, $\boldsymbol{v}_j$ and $\boldsymbol{z}_j^{(n)}$ are the feature vectors calculated respectively from the MR image and n^{th} PET update image, $\boldsymbol{\alpha}$, while σ_m, σ_p, σ_{dm} and σ_{dp} are scaling parameters for the distances in (4.13) and (4.14), which allow to adjust noise suppression and edge preservation. To make it easier to choose the kernel parameters (such as σ_m and σ_p), the feature vector, $\boldsymbol{v}_j$, is normalised as

$$\bar{\boldsymbol{v}}_j = \frac{\boldsymbol{v}_j}{SD_m}, \tag{4.15}$$

for $k_m(\boldsymbol{v}_f, \boldsymbol{v}_j)$, where SD_m is the SD of the mean voxel value over the whole MR image $\boldsymbol{v}_j$. For the PET contribution, $k_p(\boldsymbol{z}_f^{(n)}, \boldsymbol{z}_j^{(n)})$, this normalisation is slightly different. The differences in (4.14) are normalised with $\alpha_j^{(n)}$

$$\bar{\boldsymbol{z}}_f^{(n)} - \bar{\boldsymbol{z}}_j^{(n)} = \frac{\boldsymbol{z}_f^{(n)} - \boldsymbol{z}_j^{(n)}}{\alpha_j^{(n)}}. \tag{4.16}$$

In this way, the normalisation is the same for every voxel f in the neighbourhood. Local mean voxel values are not used because the operation would need to be repeated for every voxel of the image and every sub-iteration making the method more computationally demanding. The SD is also not used because of the fact that the first PET image used for the kernel is uniform, the standard deviation is then zero, and division by zero will break the reconstruction. If the voxel, $\alpha_j^{(n)}$, is zero the kernel is not applied to avoid division by zero. Note that $\alpha_j^{(n)}$ is exactly zero only outside the field of view.

Once the kernel matrix is created it is used in the first sub-iteration of HKEM to estimate α^1, and as a consequence the PET image λ^1. Then, image α^1 will be

used to calculate the PET component of the kernel, while the MR component is stored in memory. The process will be repeated for every sub-iteration. Figure (4.1) describes the creation of the feature vectors from the PET and MR image voxel values, and the process of the learning and reconstruction of the HKEM method, the KEM diagram can be obtained easily by removing the PET component in the creation of the kernel. In the traditional kernel method the learning part comes before the reconstruction, while the HKEM contains an iterative learning component which comes from the iterative reconstructed image.

The iterative property of the HKEM method updates the training sample with more relevant information. In addition, preliminary reconstructions to obtain the PET input to estimate the kernel are not necessary, therefore making the process faster and direct.

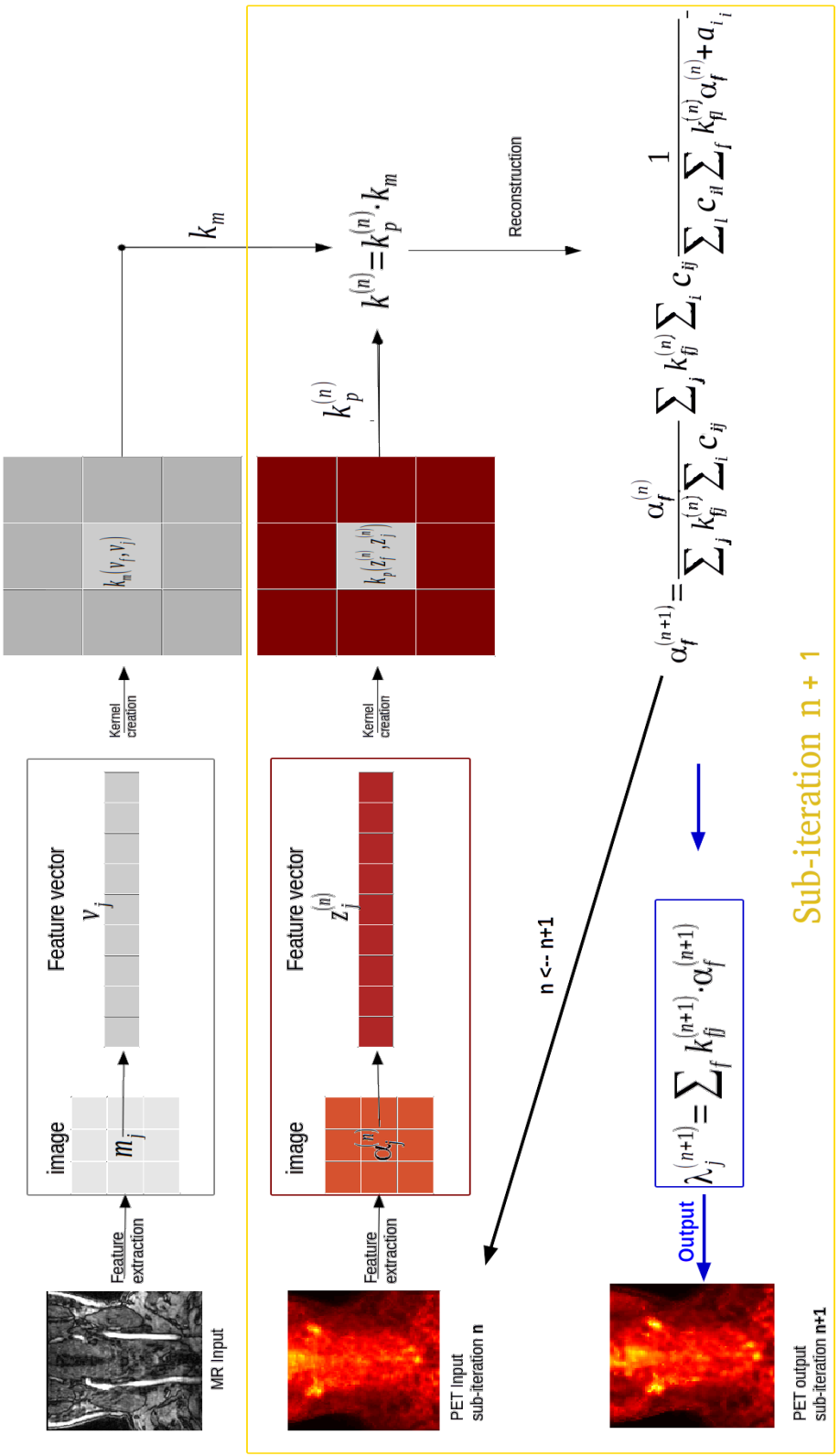

Figure 4.1: Learning and reconstruction framework for the HKEM for a generic $n+1$ sub-iteration.

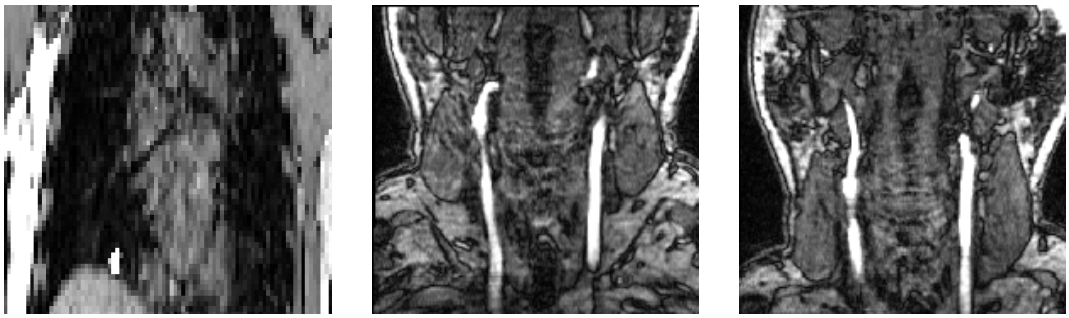

(a) (b) (c)

Figure 4.2: Slices of the MR images used to estimate the kernel matrix for different type of PET data (a) simulated anthropomorphic torso, (b) [^{18}F]FDG and (c) [^{18}F]NaF.

Note that the method has a certain similarity with the use of Sieves with the MLEM proposed by Snyder and Miller [1985]. In fact, in this study a Gaussian kernel convolution is used containing only the PET information.

4.3 Methods and Materials

4.3.1 Simulation Study

A realistic simulation study was carried out to validate the proposed method and investigate its performance under controlled conditions. The simulated data were produced by a Monte Carlo numerical simulation based on GATE (Jan et al. [2004]) which uses accurate physical modelling. The specific simulation is described in detail by Tsoumpas et al. [2011], but in brief, it uses the Philips Gemini TF scanner, described by Surti et al. [2007] having cylindrical geometry with 70 cm diameter, 18 cm length and consists of detector blocks with 44×23 crystals along 28 detector blocks. Each crystal size is 22×4×4 mm^3. The syn-

thetic data represents an anthropomorphic torso showing uniform contrast in clustered regions: lungs, myocardium, liver and three different spherical lesions between lungs and liver as shown in Figure (4.3(a)). The three lesions have their centres in different axial positions. To speed up the simulations they did not include effects such as patient motion and positron range which would need to be treated with appropriate modelling within the reconstruction system matrix. The total number of simulated events is 6.5 $\times 10^7$ with ^{18}F-fludeoxyglucose (FDG). In this study, the quantification in four cases was investigated: L1 (6 mm diameter) and L2 (12 mm diameter) are lesions which appear only in the PET images; L3 (12 mm diameter) is a lesion appearing both in the PET and the MR data (note from Figure (4.2(a)) that the MR image was augmented with a synthetic lesion equal to L3); and L4 is the part of the soft tissue which appears only in the MR. The true uptake for these ROIs is 7, 8, 4 and 1 arbitrary units (a.u.), respectively, for L1, L2, L3 and L4. The reconstructed image were obtained using 23 subsets on a 128×128×87 grid with a 4×4×2 mm^3 voxel size.

4.3.2 Phantom Experiment

A phantom experiment was performed with a Jaszczak phantom for resolution studies and PET-MR data were acquired with the Siemens Biograph mMR scanner at Mount Sinai Hospital, NY, USA. The phantom consists of cold rods of different diameters: 12.7 mm, 11.1 mm, 9.5 mm, 7.9 mm, 6.4 mm and 4.8 mm. The background represents the hot region, which was filled with 155 MBq of [^{18}F]FDG. PET data were acquired over 1 hour (5×10^9 measured events). The attenuation image was obtained from a MR volumetric interpolated examination (VIBE) acquisition segmented into two tissue classes: air and water. This

was done because the gold standard Dixon technique cannot discriminate fat from water (Karakatsanis et al. [2016]) and the attenuation coefficients were assigned erroneously. The MR contribution for the kernel was obtained from a co-registered MR-VIBE sequence. The original voxel size was $0.35\times0.35\times1$ mm^3, but it was then aligned to the PET field of view (FOV) and re-sliced to match the PET native voxel size, $2.087\times2.087\times2.031$ mm^3, and FOV size, $344\times344\times127$ voxels. PET images were reconstructed in two different cases: the original, high count, 3600 s acquisition times and modified, low-count, 5 s acquisition times. The low-count time frames were taken from the beginning of the long acquisitions and, in order to contain around the same number of events, the decay process was taken into account to give around 8.75×10^6 events.

4.3.3 Clinical Application

The LM-HKEM method was also applied to dynamic data for a patient with suspected atherosclerotic plaques in the carotid arteries. The acquisition was carried out using the Siemens Biograph mMR at Mount Sinai Hospital, NY, USA, and a consent form was signed by the patient. The patient was injected with [^{18}F]FDG 184 MBq (1.62×10^9 measured events) for the first study and [^{18}F]NaF 189 MBq (8.31×10^8 measured events) for the second, both lasted 90 min. The attenuation images were obtained from the Dixon MR from a free-breathing MR VIBE sequence using four tissue classes (air, fat, water and lungs). The LM data were divided to reproduce 10 short time frames of about 30 s each. Each of these frames contains about 1.17×10^7 events for the [^{18}F]FDG study and about 6.90×10^6 for [^{18}F]NaF. The acquisition commenced 10 minutes after the injection of the tracer. The MR part of the kernel matrix is obtained from

a time-of-flight (TOF) MR angiography sequence (Figure (4.2(b)) and (4.2(c))) producing an image with voxel size 0.7×0.7×1 mm^3. This image is then aligned to the PET field of view (FOV) and re-sliced to match the PET native voxel size, 2.087×2.087×2.031 mm^3, and FOV size, 344×344×127 voxels. The MR TOF acquisition time is 540 s. A head and neck coil was employed: 3 slabs, each consisting of 60 slices of 1 mm thickness and a coil attenuation map is included as described by Eldib et al. [2015]. This image sequence is particularly suitable for carotid PET-MR studies, because it provides high contrast between the carotid arteries and the surrounding tissue.

4.3.4 Reconstruction Setup

All datasets were reconstructed with 21 subsets and 10 full iterations using LM-HKEM. Given that subsets are used in this thesis the subset sensitivities were caluclated for each case. The values of the parameters, N, σ_m, σ_p, σ_{dm} and σ_{dp} are reported in Table (4.1). The size of the cubic neighbourhood, N, was chosen to be 3×3×3 voxels, although 5×5×5 and 7×7×7 were also studied. It is possible to see, in the results that for HKEM this does not show big improvement but actually the RMSE becomes a little higher in some cases. For the KEM the lesions L1 and L2, which are the most interesting as they are PET unique feature, are over-smoothed when using bigger neighbourhood. In addition, a bigger neighbourhood make the computation slower by a factor equal or bigger than 2. Note that if the PET and MR images have the same dimension and voxel size, then the Euclidean distances in Equations (4.13) and (4.14) are the same. This is why σ_{dm} and σ_{dp} values are the same for HKEM. For the KEM there is no σ_{dp} but only σ_{dm}. As demonstrated in both Wang and Qi [2015] and Hutchcroft

et al. [2016], the RMSE is reduced when using more nearest neighbours. They used the k nearest neighbours (knn) technique to reduce the number of voxels in the neighbourhood and make the method less computationally demanding. Because of the fact that this study uses compact feature vectors, the knn is not used and it is possible to use the total number of available voxels in the neighbourhood, which is 27. A preliminary study was carried out to confirm this result. For comparison, the same datasets have been also reconstructed with OSEM, as this is the algorithm used in clinical routine; the OSMAPOSL-MRP and the OSMAPOSL-PLS (to be referred to as MRP and PLS), and the KEM using the MR image. The PLS prior was implemented for this purpose in STIR, following the description in Ehrhardt et al. [2016]. This inclusion was motivated by the fact that the PLS prior depends on the gradient of the PET image and the gradient of the MR image and as a consequence, its hybrid nature makes it particularly relevant in the comparison. The PLS prior is decribed as follows:

$$V(\boldsymbol{\lambda}) = \sqrt{\alpha^2 + |\nabla \boldsymbol{\lambda}|^2 - \langle \nabla \boldsymbol{\lambda}, \xi \rangle^2} \tag{4.17}$$

where α is a parameter which controls the edge preservation property of the PLS, and

$$\xi = \frac{\nabla \boldsymbol{m}}{\sqrt{|\nabla \boldsymbol{m}|^2 + \eta^2}} \tag{4.18}$$

contains anatomical information from the MR; where $\boldsymbol{m}$ is the MR image and η is a parameter to avoid division by zero. Note that all algorithms in this study use LM reconstruction; for this reason, the proposed algorithm is referred to as HKEM, instead of LM-HKEM, from now on.

Kernel parameter values N=3×3×3			
	σ_{dm}=σ_{dp}	σ_p	σ_m
Simulation	1	1	1
Phantom 3600 s	3	1	1
Phantom 5 s	5	1	1
Patients 5400 s	3	1	1
Patients 30 s	5	1	1

Table 4.1: Parameter settings used for the different datasets

Scatter, attenuation, normalisation and random corrections were performed in the same way as described in Chapter 3.

4.3.5 Image Analysis

The comparison was carried out in terms of contrast-to-noise ratio (CNR) for the full dataset including all events, while bias and contrast recovery coefficient (CRC) were considered for the low-count cases. The rationale behind the choice of different image metrics for different count levels is that for the low-count case it is possible to use the long acquisition reconstructed image with 10 iterations as the 'true' image for the bias assessment and 'true' contrast for CRC. On the other hand, only CNR is a meaningful measure of contrast for the long acquisition. The 10^{th} iteration was chosen because it is assumed to be closer to convergence than the 3^{rd}, since the difference compared to the 30^{th} iteration is only 0.8 %. Although this study is focused on quantification, which is performed for all 10 iterations, the images are shown at the 3^{rd} iteration which provided good quantitative results

for all algorithms. The iteration could be chosen as the one which optimises a specific figure of merit, such as CNR, however this is dependent on the chosen ROI and varies between datasets. Therefore, using a fixed iteration number to show the reconstructed images allows better consistency among the different cases. For the Jaszczak phantom, the two regions which are reported in Figure (4.3) have been chosen: the full hot region which was segmented from MR and the cold rods were used as background to assess the impact of the noise and the contrast in a uniform region. Region of interest (ROI) analysis was performed on the clinical data using two separate regions: (a) the target ROI located in the atherosclerotic plaque of the right carotid bifurcation, which was segmented from the MR image, and (b) the background ROI drawn in the surrounding tissue of the lesion.

Quantitative comparison was performed using different figures of merit for the phantom and the patient. For the phantom:

$$CNR = \frac{t - b}{\sqrt{\mathrm{SD}_t{}^2 + \mathrm{SD}_b{}^2}}, \tag{4.19}$$

$$\overline{bias} = \frac{1}{P} \sum_{p=1}^{P} \frac{t_p - M_T}{M_T}, \tag{4.20}$$

and

$$\overline{CRC} = \frac{1}{P} \sum_{p=1}^{P} \frac{t_p - b_p}{C_T}, \tag{4.21}$$

$$\overline{CoV} = \frac{1}{P} \sum_{p=1}^{P} CoV_p, \tag{4.22}$$

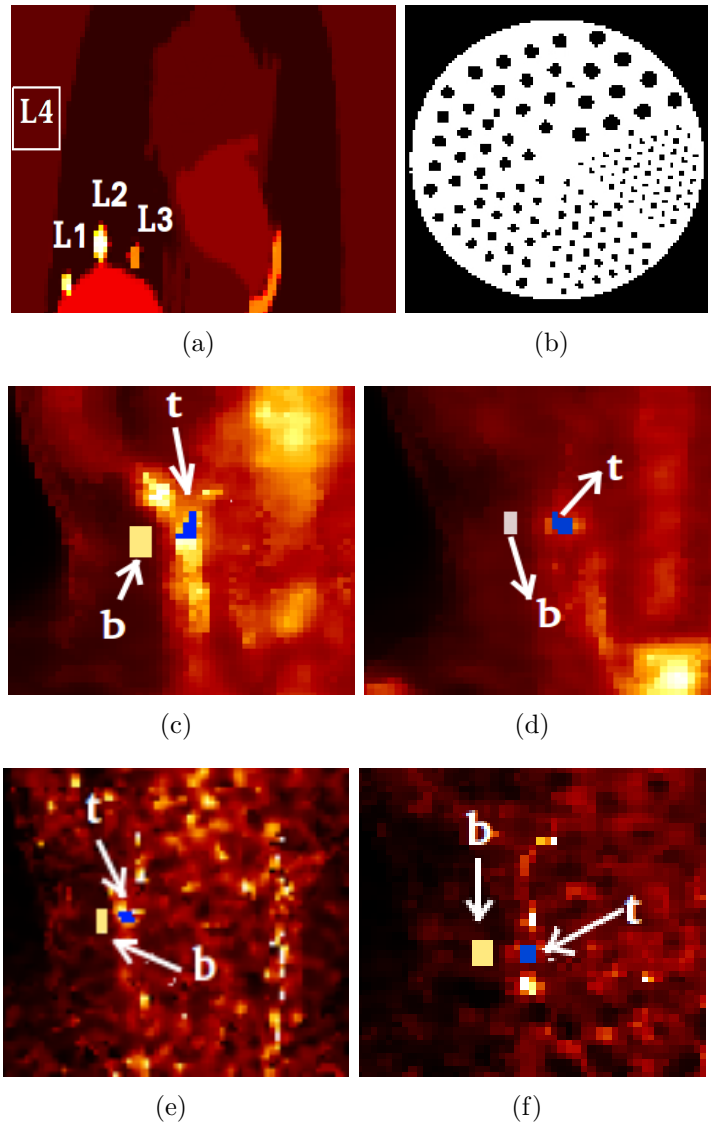

Figure 4.3: Regions of interest (ROI) chosen for this study: (a) three lesions, L1, L2 and L3 and normal tissue region, L4 for the simulation, (b) the target ROI extended over all the transaxial slices of the phantom (white part), and the background described by the black rods; (c) target, t, and background, b, ROIs for the patient [^{18}F]FDG study with 5400 s acquisition; (d) target, t, and background, b, ROIs plaque for patient [^{18}F]NaF study with 5400 s acquisition; (e) target, t, and background, b, ROIs for the patient [^{18}F]FDG study with 30 s acquisition and (f) target, t, and background, b, ROIs for patient [^{18}F]NaF study with 30 s acquisition. The target and background ROIs are indicated by the white arrows for (c), (d), (e) and (f).

where t and b are the mean values over target (hot region) and background (cold rods) ROIs, SD_t and SD_b are the standard deviations related to target and background ROI, respectively. Note that CNR was used only for the single long acquisition image. For the low-count images, a mean CRC, and a mean bias, were calculated over the 10 sub-samples: M_T is the mean value in the ROI of the long acquisition reconstructed with OSEM at the 10^{th} iteration and 21 subsets, which is taken as the 'true' value, t_p is the mean value of the chosen ROI and sample p, P is the number of sub-samples, b_p is the mean value of the target background ROI, C_T is the true contrast calculated from the long acquisition image, and CoV_p is the coefficient of variation (CoV) of the voxels inside the region of interest for the specific sample or time frame and is estimated as the percentage SD.

Apart from the calculation of CNR for the long acquisition, the analysis procedure is slightly different with the patient data. This is due to the fact that there are several sources of variability for a real human body, such as motion, kinetics and others. Therefore, the average value over the 10 time frames was not evaluated, while the CRC was calculated for each time frame. In addition, a different form of bias, the bias of the sum was estimated in this case. In particular, all the 10 time frame images were summed up and compared with a reconstructed image from a 304.349 s acquisition. Note that the duration of each time frame takes into account the decay process, which is the reason why the sum is not 300 s. Bias and CRC were calculated as follows:

$$bias = \frac{S - M_T}{M_T} \quad \text{and} \quad CRC_p = \frac{t_p - b_p}{C_T} \tag{4.23}$$

where S is the value of the sum over the time frames in the selected ROI, M_T is

the value in the same ROI for the 304.349 s image, and C_T is the true contrast calculated on the long acquisition image as the difference between the values of target and background ROIs.

4.4 Results

4.4.1 Simulation

Figure (4.4) shows the optimisation of the kernel parameters (σ_p, σ_m, σ_{dp} and N) in terms of RMSE. Note that $\sigma_{dm} = \sigma_{dp}$ in this study because the voxel size of the MR image is the same as of the PET image.

Figure (4.5) presents the bias-CoV plot in all ROIs, and over 10 iterations. Also, it shows a comparison between OSEM, MRP, PLS, KEM and HKEM. The image quality comparison is reported in Figure (4.6). Figure (4.7) shows the line profiles for each lesion of the simulated phantom and for all algorithms, at the 10^{th} iteration.

RMSE					
Lesion	OSEM	MRP	PLS	KEM	HKEM
L1	11.37	55.92	68.0.5	36.49	20.48
L2	36.99	40.67	48.81	37.36	34.95
L3	38.35	43.10	16.78	26.92	27.65
L4	49.75	24.22	29.60	25.50	25.46

Table 4.2: RMSE at the iteration with minimum RMSE: OSEM 10, MRP 10, PLS 9, KEM 25, HKEM 16.

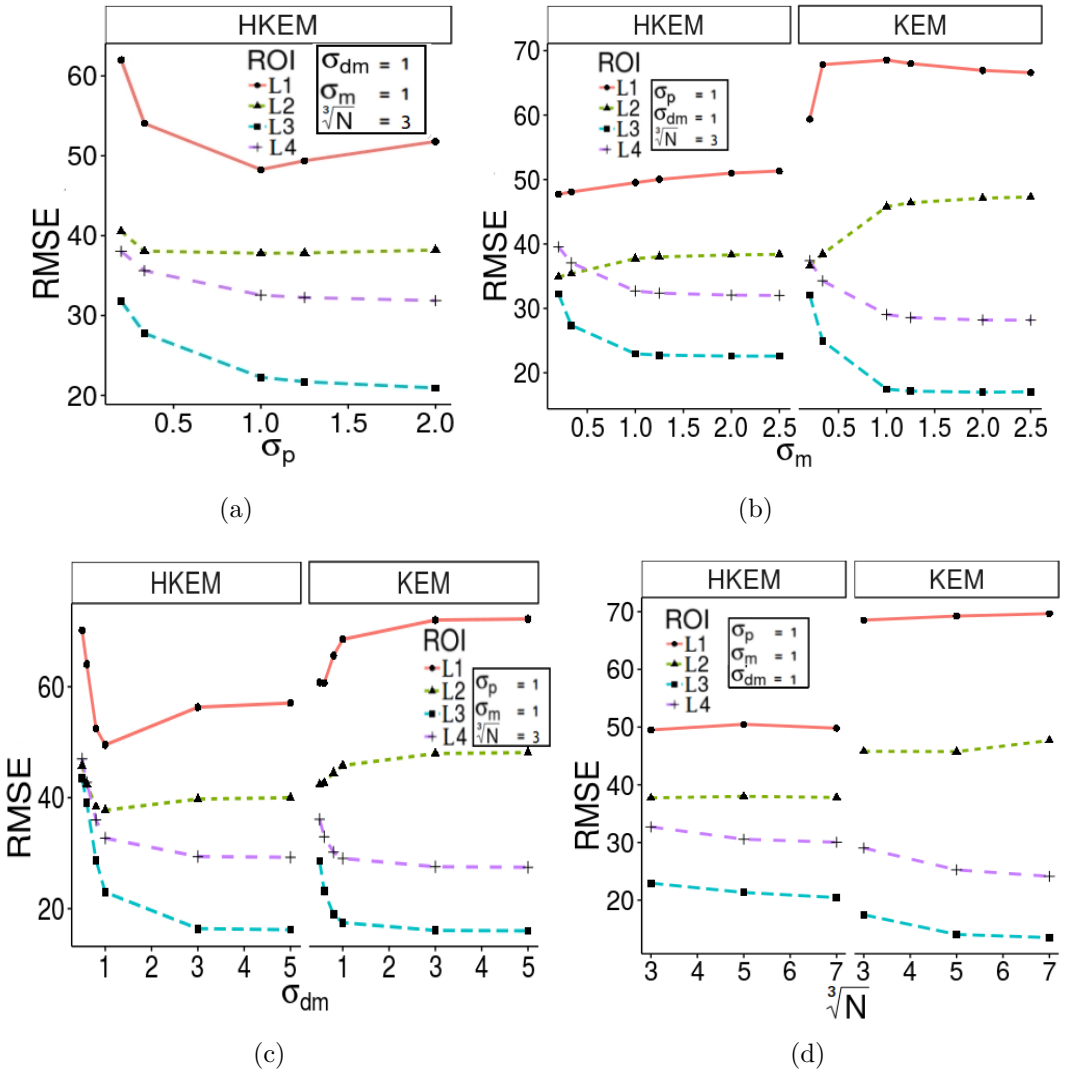

Figure 4.4: Effect of hybrid kernel parameters: (a) σ_p, (b) σ_m (c) $\sigma_{dm} = \sigma_{dp}$ and (d) N on RMSE using the simulated torso. The comparison is performed at the 10^{th} full iteration.

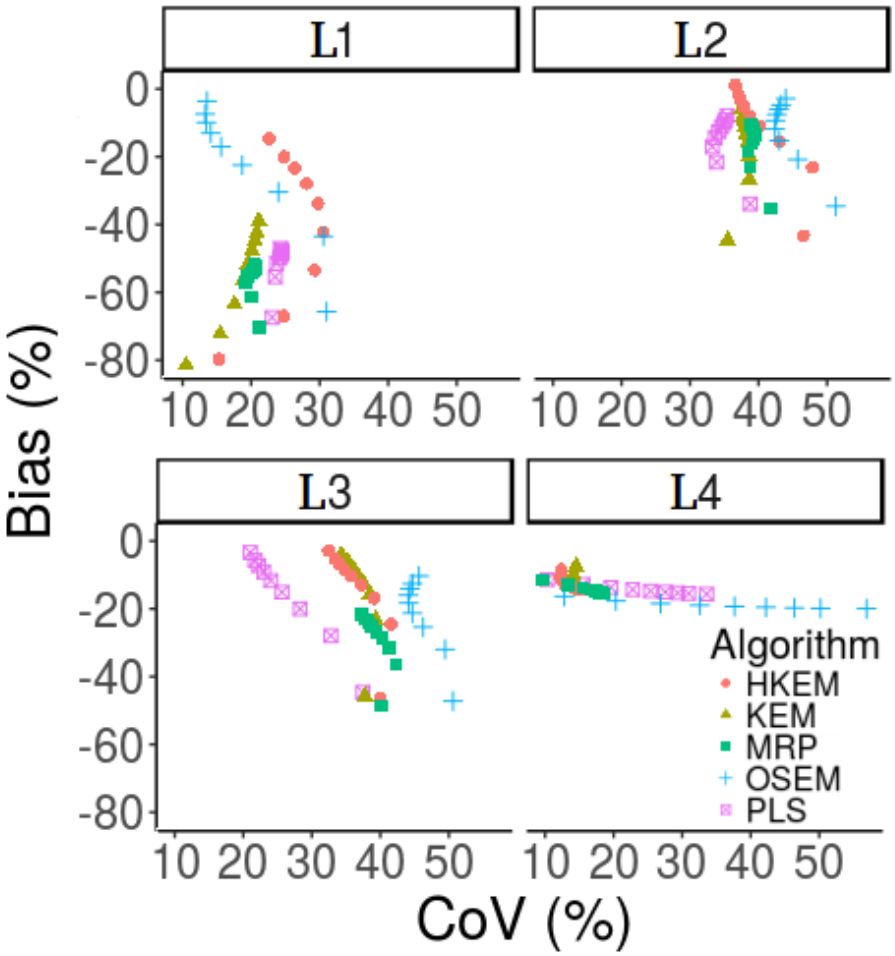

Figure 4.5: Bias-CoV plot for the ROIs L1, L2, L3 and L4. The figure shows the comparison between reconstructed images with PLS, OSEM, OSEM+G, MRP, KEM, the proposed method HKEM over 10 iterations for the simulated torso.

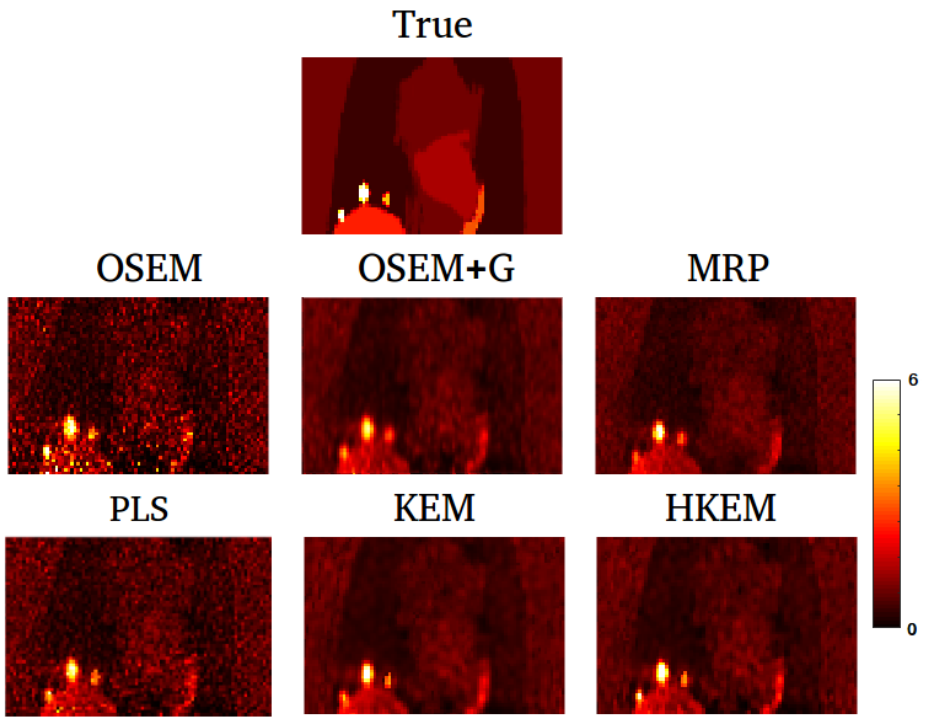

(a)

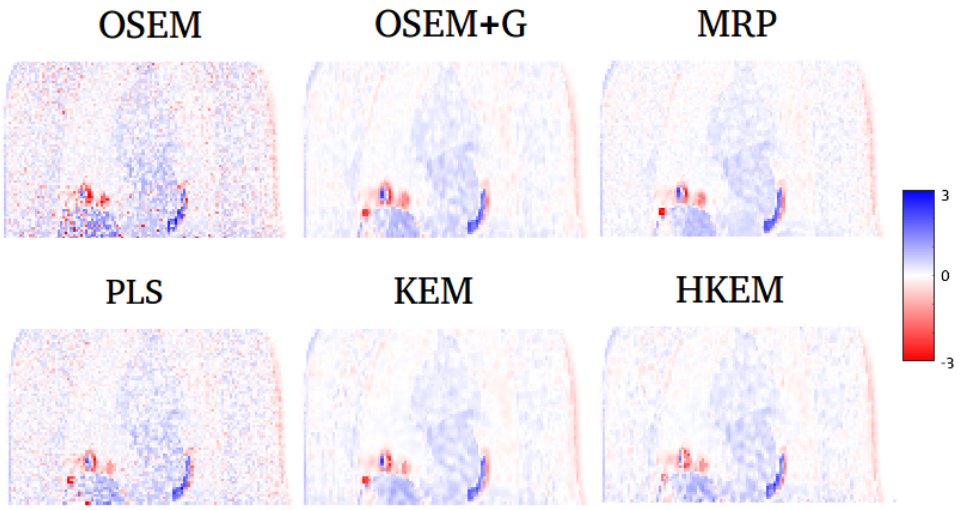

(b)

Figure 4.6: Image comparison (a) between the True image and the reconstructed images with OSEM, OSEM + 5 mm Gaussian post filter, MRP, PLS, KEM, the proposed method HKEM over 10 iterations for the simulated torso; (b) the bias image calculated from the ground truth.

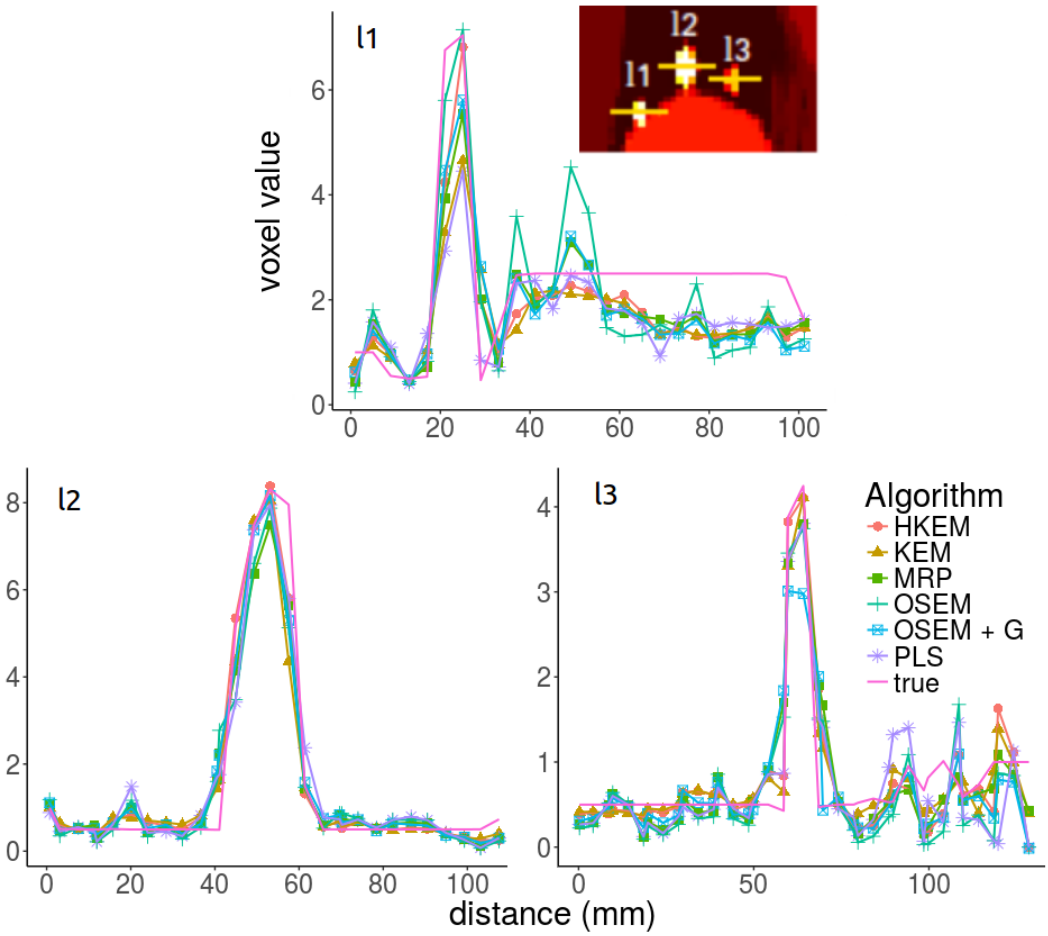

Figure 4.7: Line profile (LP) comparison between the true simulated image and the reconstructed images with PLS, OSEM + 5 mm Gaussian post filter, OSEM, MRP, KEM, the proposed method HKEM for the lesions L1, L2, L3, of the simulated torso, at the 10^{th} iteration.

4.4.2 Phantom

Figure (4.8) reports the mean value of the phantom ROI as a function of the iteration number to study the convergence rate of the kernel methods in comparison with the convergence rate of OSEM. Figure (4.9) shows the ROI comparison, using the Jaszczak phantom, between OSEM, MRP, PLS, KEM using MR, and the proposed HKEM in terms of CNR for the long acquisition. All the images shown correspond to the 3^{rd} iteration. Figure (4.10) shows the image quality obtained with all methods in this study. The top row represents the long acquisition while the bottom shows the 5 s frame. Figure (4.11) reports the line profiles showing the differences between rods of different diameter. Figure (4.12) shows the mean bias, from equation (4.20), as a function of $\overline{CoV}$. In Figure (4.13) a ROI comparison is provided for the mean CRC, shown as a function of the $\overline{CoV}$ over 10 iterations, using the 5 s reconstructions. The CRC was averaged over the 10 sub-samples using the formula in (4.21) while the $\overline{CoV}$ was obtained similarly using equation (4.22). The penalty factors of the MRP and all PLS parameters were chosen to find a reasonable trade-off between bias and CoV. A similar procedure was followed for each parameter of the kernelised methods. The values of the kernel parameters are reported in Table (4.1). To give an idea of the computational time, in Table (4.3) the reconstruction time required for 10 iterations of a 5 s frame for each algorithm is reported and they refer to the University of Leeds high performance computer: each reconstruction used one of the 10 cores Intel E5-2660v3 (2.6GHz) processor, and the available memory is 256 GB. The compiler that was used was GCC 4.4.7.

Computational time for 1 iteration					
5 s frame reconstruction					
Method	OSEM	MRP	PLS	KEM	HKEM
Time (min per iteration)	11	12.8	13.5	14.8	16.2

Table 4.3: Computational time performances for the algorithms.

4.4.3 Patient studies

Similar image analysis was carried out for the patient studies. Figures (4.14) and (4.18) show the CNR comparison, among all algorithms, for the [^{18}F]FDG and [^{18}F]NaF study respectively, using the right carotid plaque (as it shows higher uptake) in Figures (4.3(c)), (4.3(d)), (4.3(e)) and (4.3(f)) as the target (hot region) and the surrounding tissue as the background (cold region). In Figures (4.15) and (4.19), the CRC metric, as evaluated for the [^{18}F]FDG and [^{18}F]NaF carotid study with equation (4.23) for four low-count (30 s) frames, illustrates the consistency of the results. The four time frames cover, respectively, from 630-660 s, 720-750 s, 810-830 s and 870-900 s after [^{18}F]FDG injection, and 600-630 s, 750-780 s, 780-810 s and 870-900 after [^{18}F]NaF injection, and they have been labelled accordingly. Bias was evaluated as described in section 4.3.5 using equation (4.20). Figures (4.16) and (4.20) show the comparison among the different methods using the [^{18}F]FDG and [^{18}F]NaF data. The plot shows the bias of the sum, as a function of the $\overline{CoV}$ related to each iteration. The MR images used as the source of the kernel are shown in Figures (4.2(b)) and (4.2(c)).

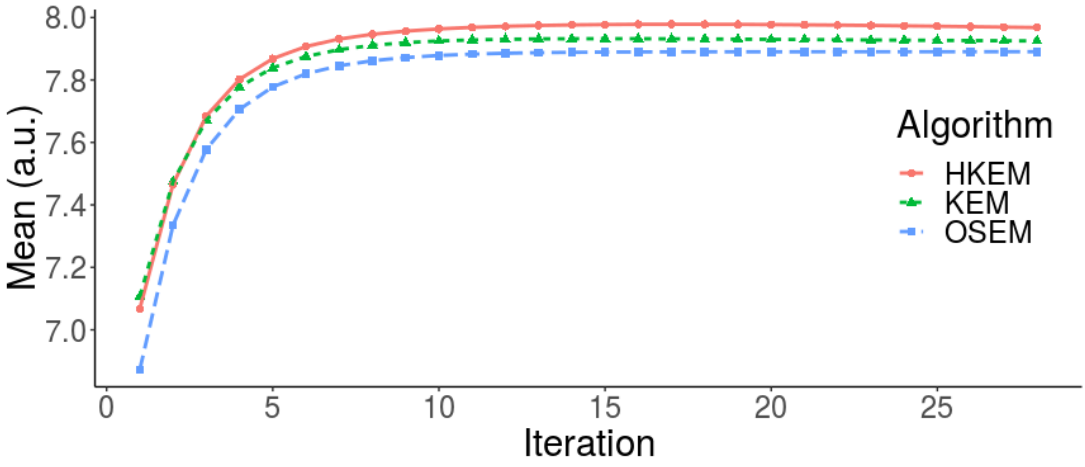

(a)

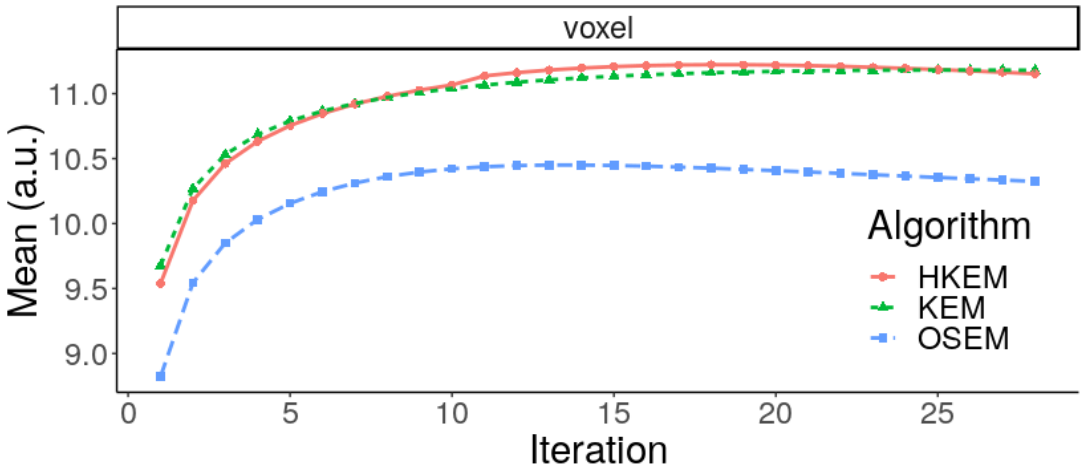

(b)

Figure 4.8: Mean value over 30 full iterations: (a) for the hot ROI of the Jaszczak phantom (b) for one voxel in the hot region of the phantom.

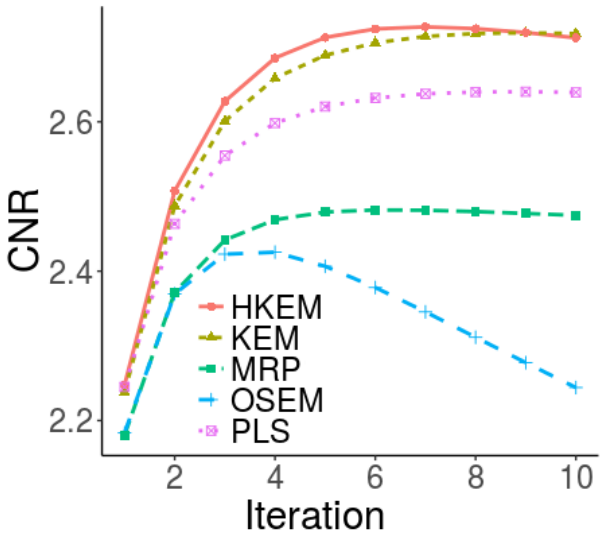

Figure 4.9: CNR comparison between reconstructed phantom images with PLS, OSEM, MRP, KEM, and the proposed method HKEM for 3600 s acquisition.

4.5 Discussion

In this chapter the proposed HKEM, which includes information from both MR and PET, was validated and investigated. In addition, the results were compared with a set of different algorithms. Particular attention is focused on the improvement in quantification at different count-levels. The parameter study using the simulation investigates four different cases. Regions L1 and L2 represent the case of a lesion being only detected by PET, however L1 represents a borderline case where the lesion is very small and it is also attached to the liver, making it possible to study the limitations of the proposed method. Region L3 shows the case where the lesion is detected from both MR and PET. Finally, L4 is the region where PET contains uniform uptake while MR shows different soft tissues. From Figure (4.4) it is possible to see how the RMSE changes as a function of the parameters and for each ROI. It is generally safe to use the setting in Table

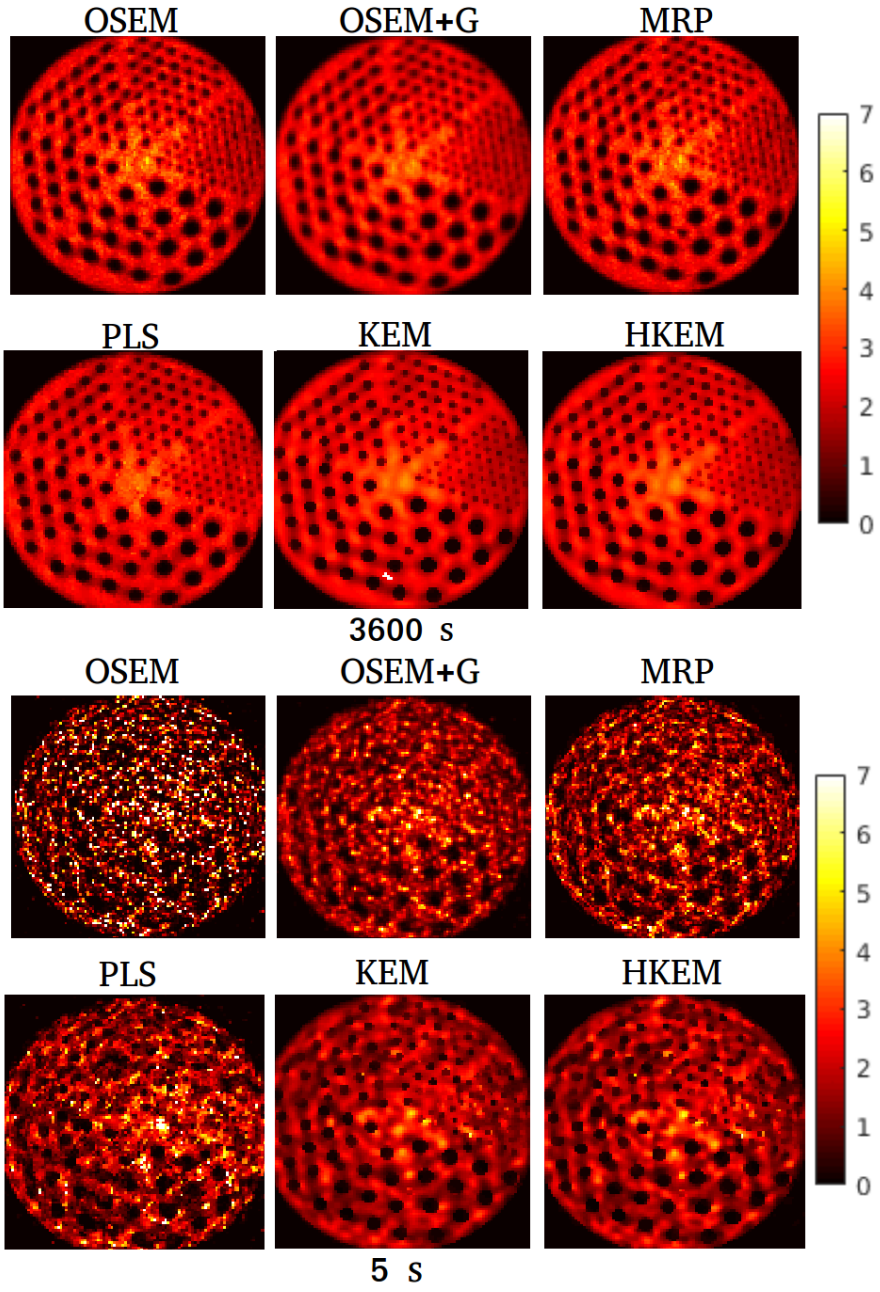

Figure 4.10: Reconstructed images, at the 3^{rd} iteration, with OSEM, OSEM + 5 mm Gaussian post filter, MRP, PLS, KEM using only MR and the proposed method HKEM for the Jaszczak phantom. The figure reports in the top line the 3600 s acquisition, and in the bottom line the 5 s frame.

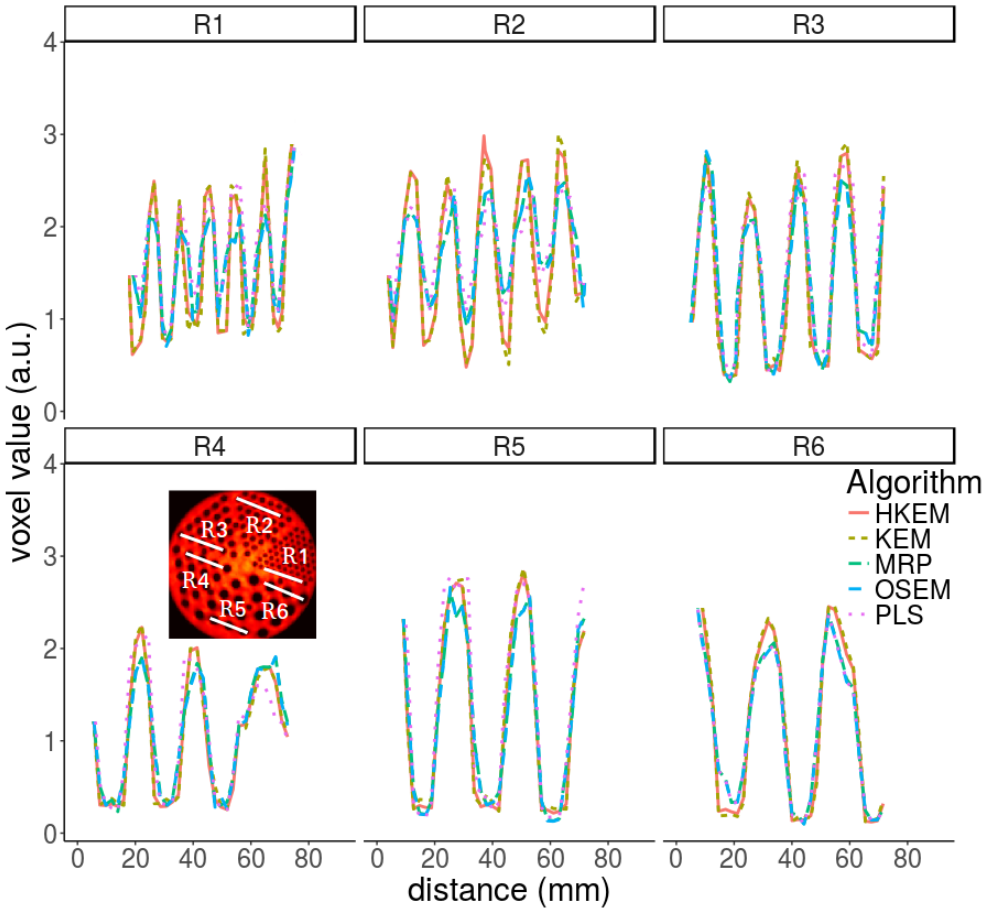

Figure 4.11: Line profiles for the Jaszczak phantom images, at the 3^{rd} iteration, with PLS, OSEM, MRP, KEM using only MR and the proposed method HKEM for the Jaszczak phantom. The figure reports in the line profiles for the different size rods, R1, R2, R3, R4, R5, R6, from the smallest to the biggest.

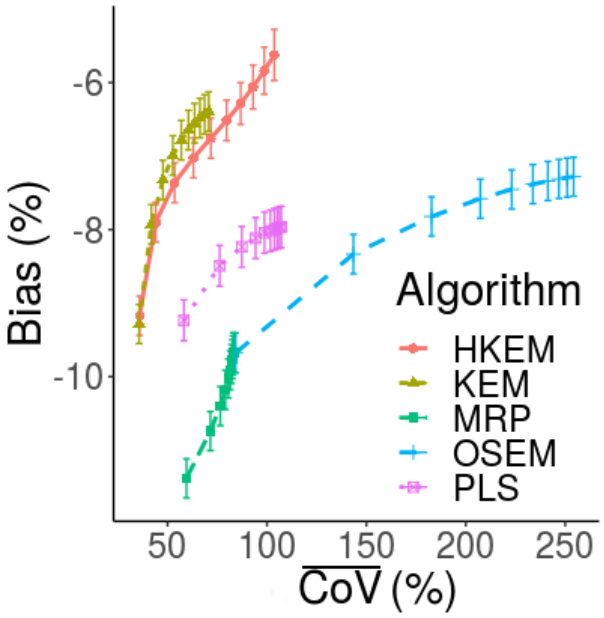

Figure 4.12: Bias-CoV plot showing the comparison between reconstructed images with PLS, OSEM, MRP, KEM, and the proposed method HKEM over 10 iterations, from left to right, for 5 s acquisition in the hot ROI of the Jaszczak phantom. The error bars represent the standard deviation of the ROI value over the 10 sub-samples. The quantity $\overline{CoV}$ represent the average over the 10 time frames.

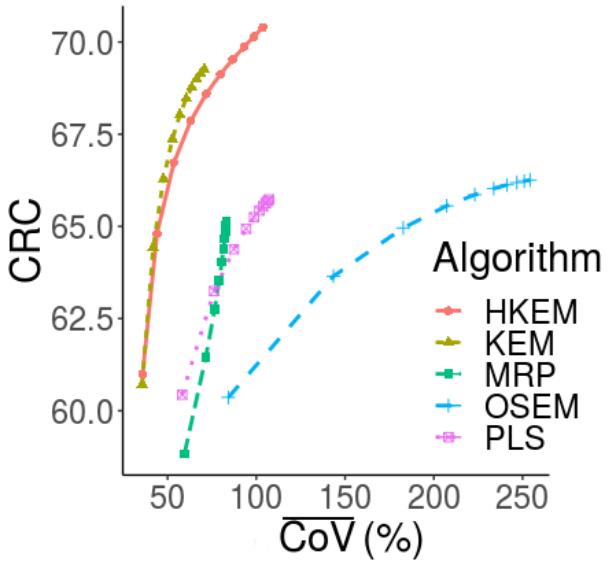

Figure 4.13: CRC-CoV plot showing the comparison between reconstructed images with PLS, OSEM, MRP, KEM, and the proposed method HKEM over 10 iterations, from left to right, on 5 s phantom acquisition. The quantity $\overline{CoV}$ represent the mean CoV over 10 time frames.

(4.1), which has led to the detection of all lesions in the study. If the study aim is, however, a high level of quantitative accuracy for lesions that are smaller than the kernel neighbourhood, it would be better to use either $\sigma_{dp} = 0.5$ or $\sigma_p = 0.3$. Both these values will have the effect of increasing the noise but making the quantification, even for small regions, very accurate. Finally, although large values of N have been shown to better suppress the noise, they also make the RMSE higher in some cases (Figure (4.4)) and the computation slower.

The σ_m and σ_p parameters reflect the relative contribution of MR and PET. When the data are very noisy, it is better to increase the PET contribution to obtain a smoother image, however this will gradually reduce the quantification accuracy of the proposed method. Figures (4.5) and (4.6) show the comparison between the different algorithms and for all the ROIs in terms of quantification

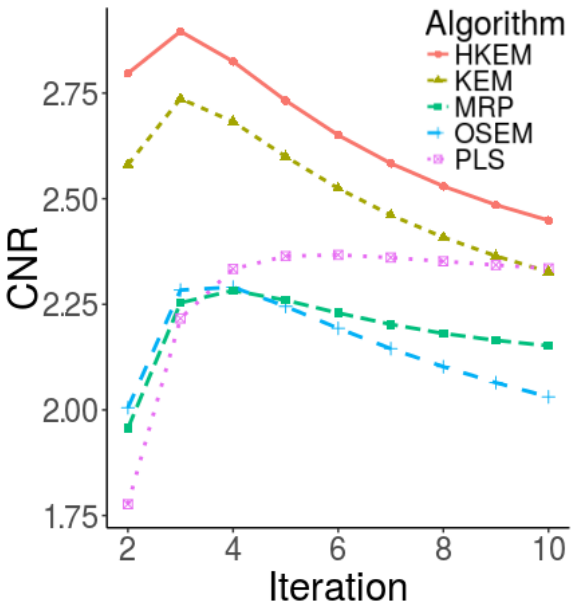

Figure 4.14: CNR comparison between reconstructed images with PLS, OSEM, MRP, KEM, and the proposed method HKEM over 10 iterations, from left to right, for 5400 s carotid [^{18}F]FDG acquisition.

and image quality. Also, Figure (4.5) shows that the HKEM method outperforms all the other techniques for lesion L2, and that when the MR features are similar to the PET distribution, all MR-based methods perform well, whereas they can be at least 5% worse than the HKEM when MR has not related contrast on the corresponding area. The same outcome can be seen in Figure (4.7) where the line profiles for HKEM are closer to the true image, while avoiding the noise that is expressed by the OSEM. In particular this is more evident for the lesion L1 and L2. Such results describe the reliability of the proposed method even when no information about the lesion is included in the MR image.

The L1 and L4 regions are informative showing that for quantification of lesions smaller than the voxel neighbourhood a smaller σ_p is required, and that quantification in a uniform region is not affected by the presence of MR tissue-

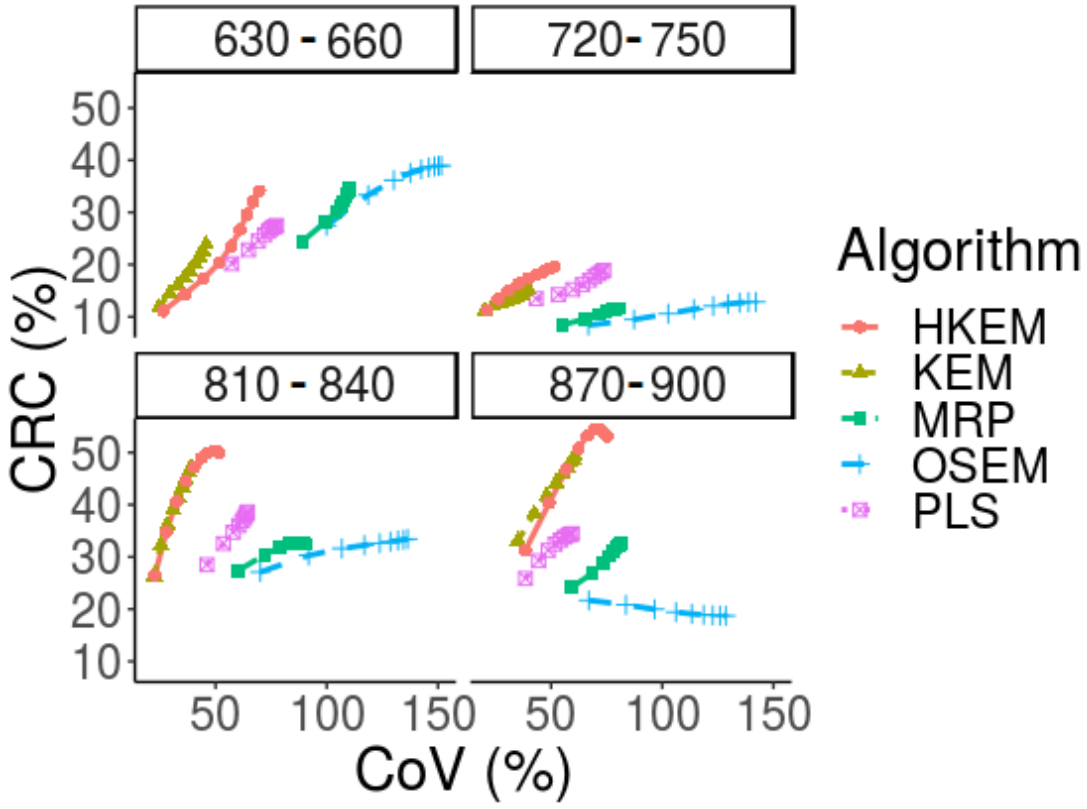

Figure 4.15: CRC-CoV plot showing the comparison between reconstructed images with PLS, OSEM, MRP, KEM, and the proposed method HKEM over 10 iterations, from left to right. The plots show four [^{18}F]FDG patient time frames corresponding to the time intervals 630-660 s, 720-750 s, 810-830 s and 870-900 s after injection.

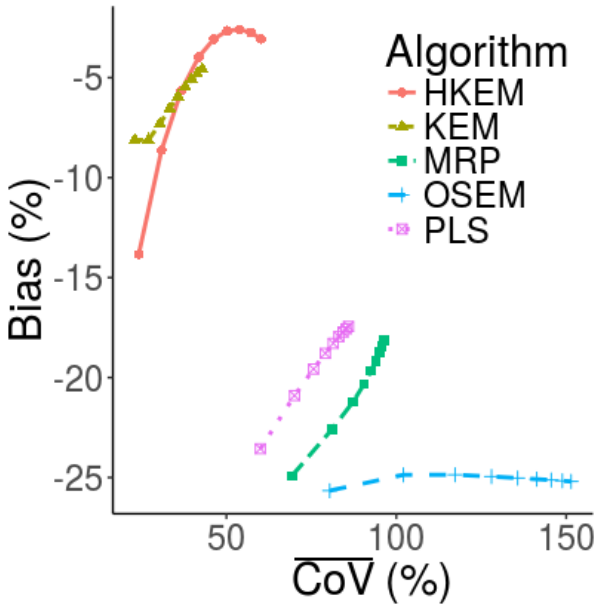

Figure 4.16: Bias-CoV plot showing the comparison between reconstructed images with PLS, OSEM, MRP, KEM, and the proposed method HKEM over 10 iterations, from left to right. The plot shows the bias calculated from the sum of all 10 (30 s) [^{18}F]FDG time frames.

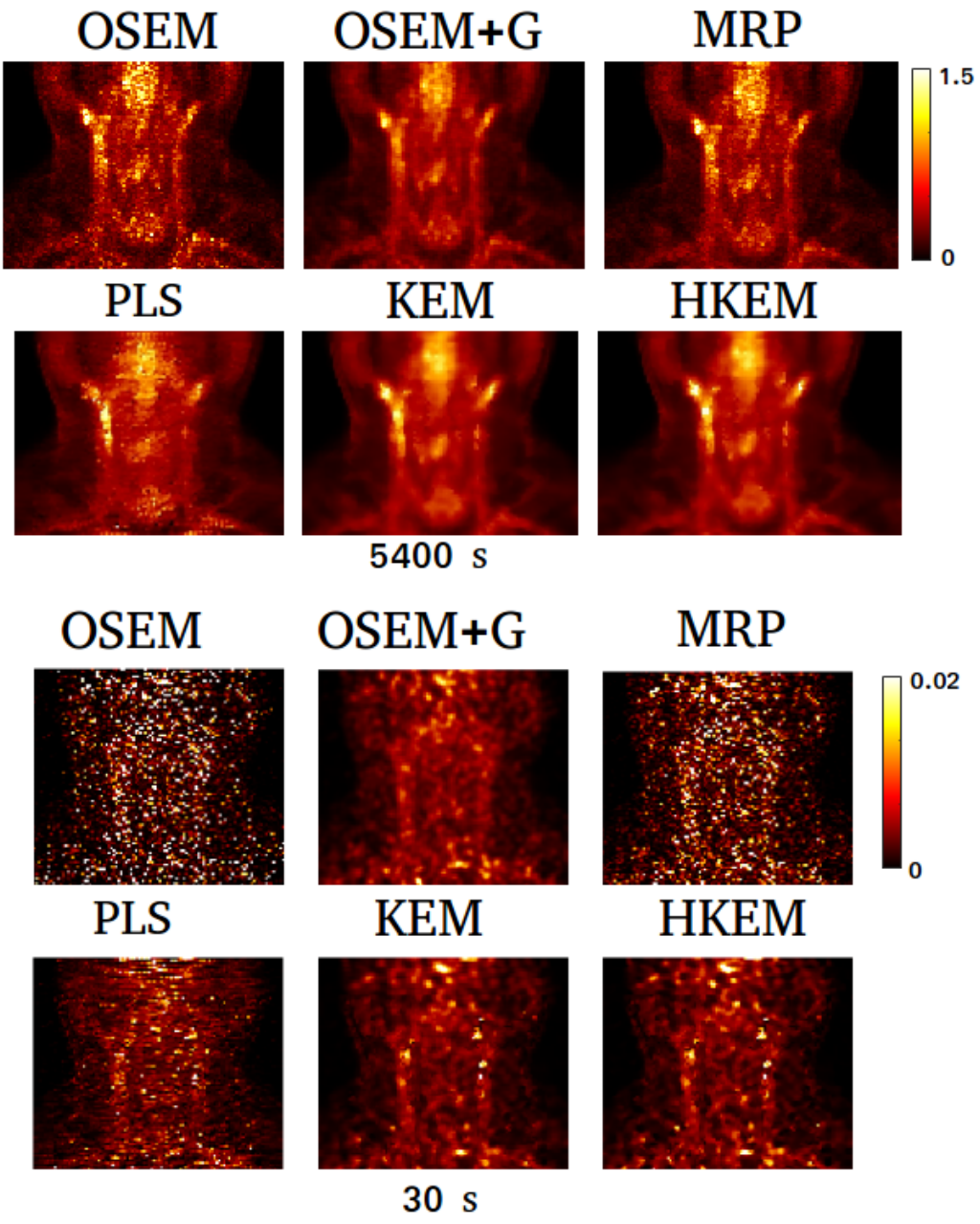

Figure 4.17: FDG study reconstructed images, at the 3^{rd} iteration with OSEM, OSEM + 5 mm Gaussian post filter, MRP, PLS, KEM, and the proposed method HKEM. The figure reports in the top line the 5400 s acquisition, and in the bottom line the 30 s frame.

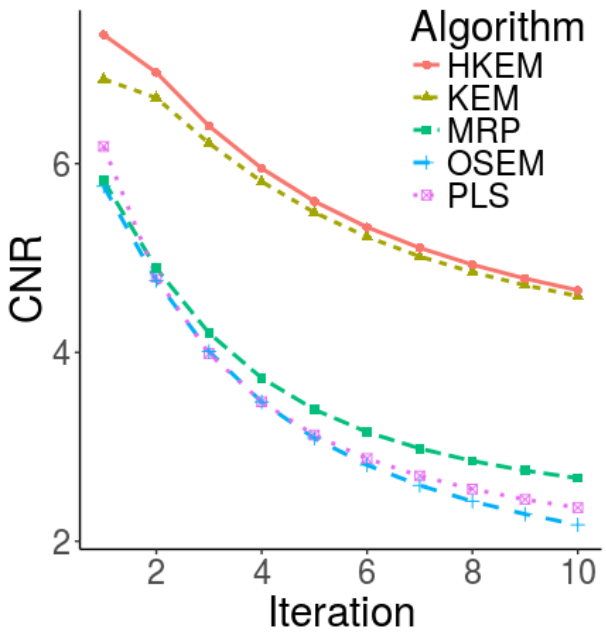

Figure 4.18: CNR comparison between reconstructed image with PLS, OSEM, MRP, KEM, and the proposed method HKEM for 5400 s acquisition with [^{18}F]NaF. The highest CNR value are the early iterations.

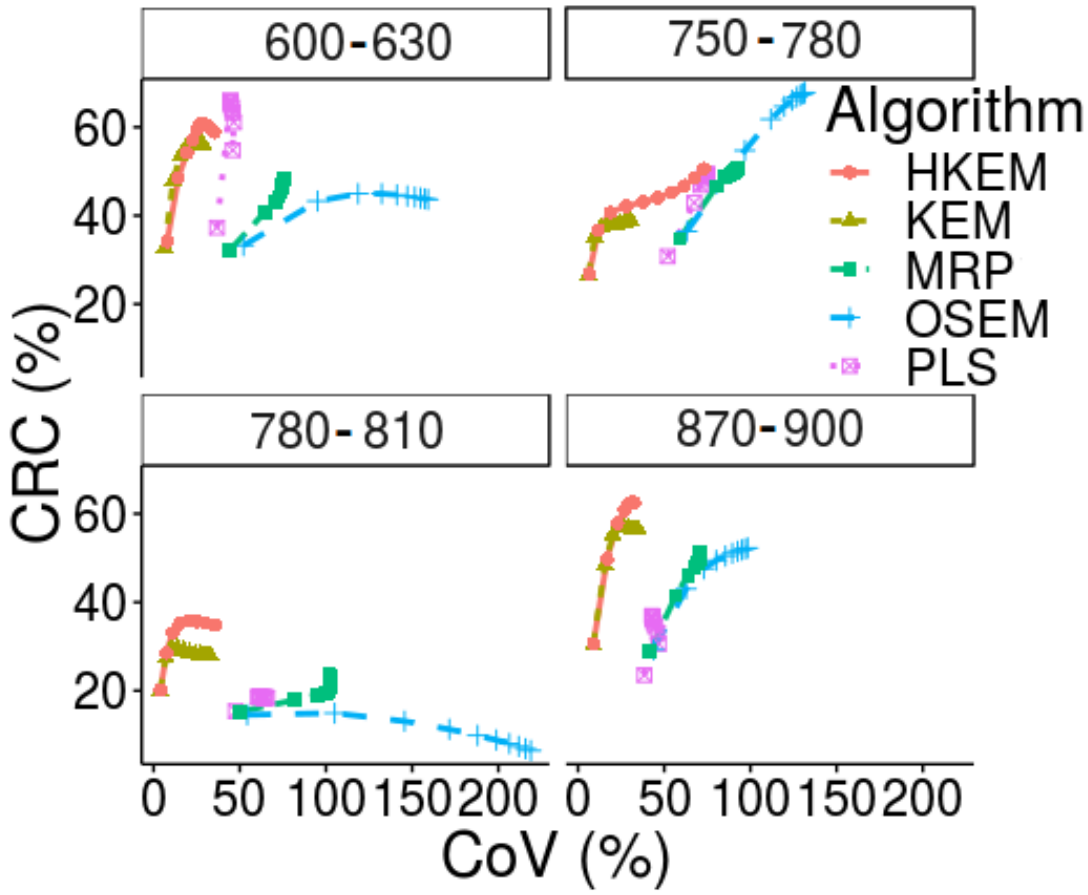

Figure 4.19: CRC-CoVplot showing the comparison between reconstructed images with PLS, OSEM, MRP, KEM, and the proposed method HKEM over 10 iterations, from left to right. The plots show four time frames corresponding to the time intervals 600-630 s, 750-780 s, 780-810 s and 870-900 s after [^{18}F]NaF injection.

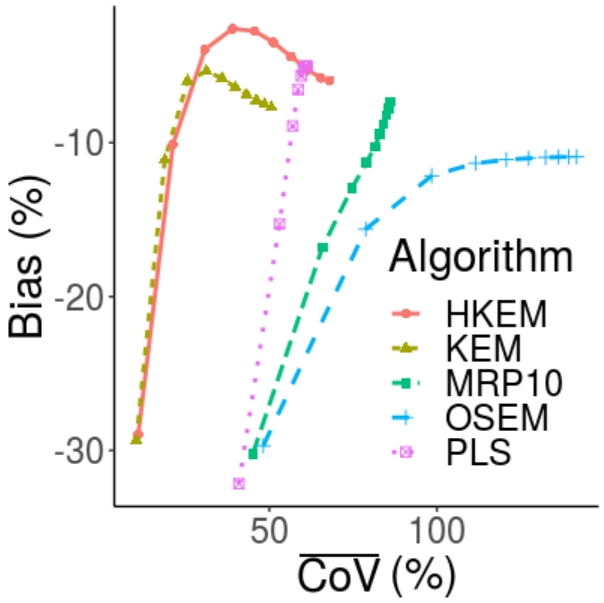

Figure 4.20: Bias-CoV plot showing the comparison between reconstructed images with PLS, OSEM, MRP, KEM, and the proposed method HKEM over 10 iterations, from left to right. The plot shows the bias calculated from the sum of all 10 time frames with [^{18}F]NaF. The highest bias value are the late iterations

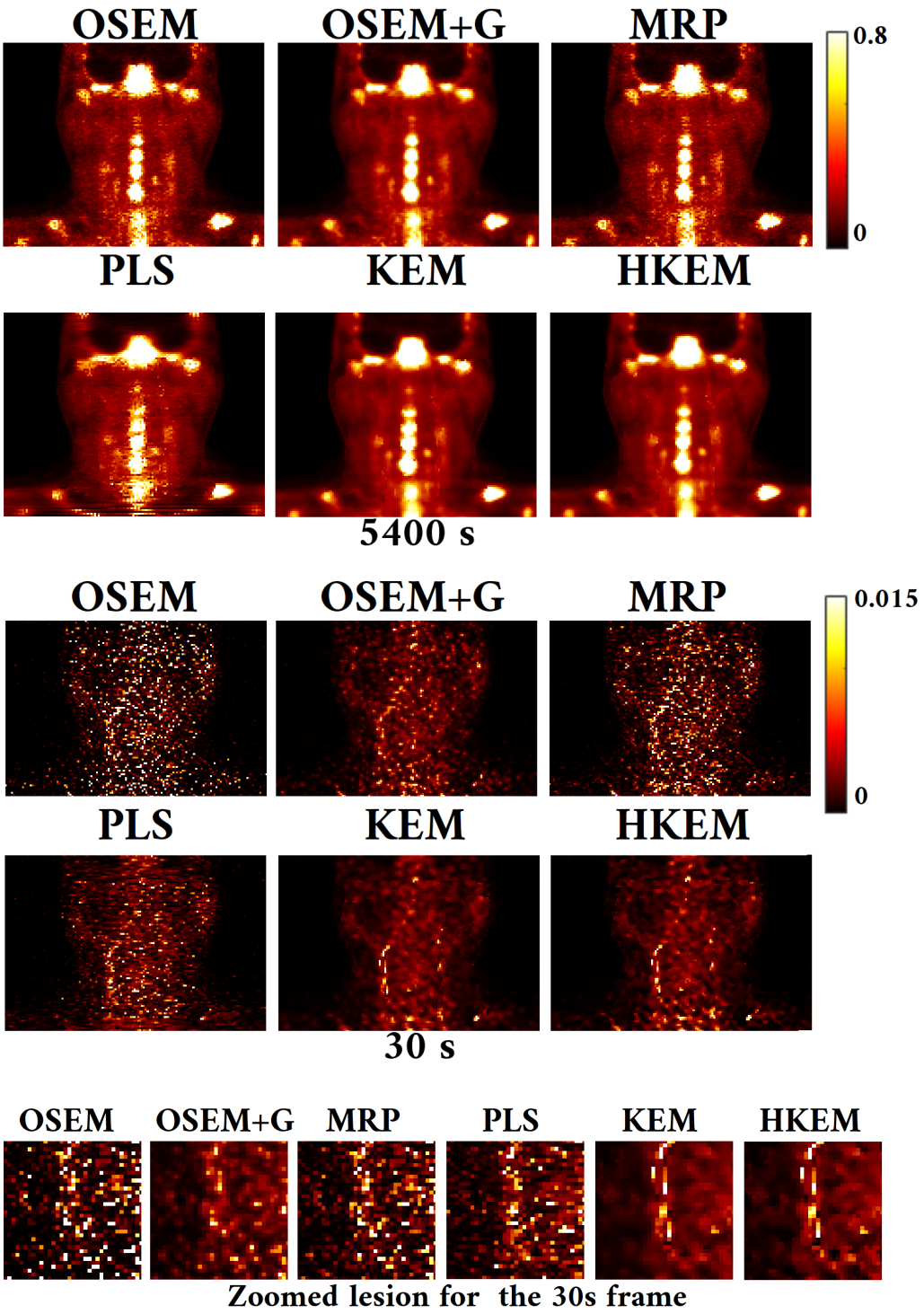

Figure 4.21: NaF reconstructed images, at the 3^{rd} iteration with OSEM, OSEM + 5 mm Gaussian post filter, MRP, PLS, KEM, and the proposed method HKEM. The figure reports in the top the 5400 s acquisition, in the middle the 30 s frame and in the bottom the zoomed lesion of the 30 s frame.

borders, as the bias is similar for all the algorithms.

Figure (4.8) shows the ROI mean value as a function of the iteration number for both simulation and Jaszczak phantom, and it can be seen that HKEM and KEM have a similar convergence behaviour as the OSEM. Figure (4.9) shows the CNR for the 3600 s acquisition of the Jaszczak phantom as a function of the iteration number. The figure shows good performance for all the MR-driven methods with the HKEM having the highest CNR. In Figure (4.10), it is possible to see that the kernel methods and PLS show good resolution recovery showing that similar image quality can be obtained with different anatomically-driven techniques, at normal count-levels, if the PET and MR images are spatially matching.

Figure (4.11) shows the line profiles for the rods with different diameters. The improvement achieved by the kernel method is evident even for the case of the narrowest rods.

The study with ten 5 s sub-samples was carried out in terms of bias and CRC using the 3600 s image as a reference. From Figure (4.12), it is possible to obtain with the proposed method bias lower than 6% compared with 7.5% for KEM, 8% for PLS and OSEM, and over 9% for MRP. Figure (4.13) shows that even though the number of events is reduced by a factor of about 600, around 70% CRC was obtained with the proposed method and KEM, while lower values were achieved with the other methods. From the bottom row of Figure (4.10) it is possible to appreciate the good performance of the kernel method in reducing the noise while keeping a very good contrast and resolution. From the low-count Jaszczak phantom experiment it is clear that the KEM provides the best trade-off between bias and noise, and CRC and noise when PET and MR have detected the same

boundaries, this is because the noise for the HKEM increases faster than KEM with the increasing iterations.

In Table (4.3) it can be seen that both kernelised methods are slower than OSEM. This is because a search in the neighbourhood is performed for each voxel three times every iteration.

Patient investigations were carried out to give two different examples of applications for the proposed method using atherosclerosis studies published by Karakatsanis et al. [2017]. Regarding the [^{18}F]FDG patient experiment, for the 5400 s acquisition, CNR was calculated on the defined ROIs and compared all the studied techniques. Figure (4.14) shows higher CNR for HKEM, followed by the KEM and PLS. The low-count case consisted of 10 consecutive time frames of around 30 s starting from 600 s post injection. Figure (4.15) shows higher CRC over time frames for the same iteration number for HKEM, except in one case were PLS reaches the highest CRC, while the CoV for HKEM is bigger than KEM. Figure (4.16) shows an improved bias— less negative than all the other algorithms. It is possible to see, from Figure (4.15), that the contrast varies between time frames, this is due to effects such as motion and kinetics that introduce variability over time. The first and third rows of Figure (4.17) show the image quality for the 5400 s acquisition with [^{18}F]FDG. It is worth noting the improved carotid local resolution and contrast around the area of the carotid for PLS, KEM and HKEM, although the PLS image shows suppression of the PET unique lesion above the right aorta. From the second and fourth rows of Figure (4.17) it is possible to see how the kernel method is able to suppress noise while keeping a satisfactory level of contrast in the location of the suspected carotid lesions even for low-count data.

Although several parameter settings were investigated for PLS, it was not possible to obtain a better image than the one shown in the bottom row of Figures (4.10) and (4.17). This is probably due to the fact that this technique is not based on a local neighbourhood, which is very efficient at tackling noise. The results from the [^{18}F]NaF patient study in Figures (4.18)-(4.21), are consistent with the findings for the [^{18}F]FDG case and the phantom, showing that HKEM provides higher or similar values of CNR, CRC and bias compared to KEM and always higher than the other algorithms. Of particular interest is the bias, as it has previously been shown that OSEM and penalised algorithms are biased under low-count circumstances (Karaoglanis et al. [2015]; Walker et al. [2011]). Positive bias is associated with the positivity constraint in iterative reconstruction algorithms, this is because the average value without negative values is shifted to a higher value, therefore the bias is more positive. When the number of events is very small there can be trapping of iterative estimates at zero making the average values lower thus introducing negative bias in those regions (Jian et al. [2014]). The results of this study show that the kernel method, and also Bayesian anatomical priors, can reduce this effect in all datasets. Furthermore, when the MR information is combined with the available PET information, this reduction is even stronger, making it feasible to produce less biased images even at lower injected doses. This is due to the fact that each voxel is correlated with its neighbours and although one can have zero value, some of the neighbours will have non-zero values, and this will result in an increased voxel value. For the PLS algorithm no neighbourhood is used, however, the gradients are calculated between pairs of neighbouring voxels in all directions. When the MR features over-smooth the unique PET features, the PET kernel preserves the signal mak-

ing the proposed method more reliable while providing quality image which is as good as the KEM.

Nevertheless, depending on the noise level of the data it can be seen that in some cases the CoV increases iteration after iteration for the HKEM whilst it increases less in the KEM. Because of the normalisation of the feature vector from equation (4.15) and (4.16), which avoids the dependence from the image scale, HKEM and KEM provide stability in terms of parameter optimisation, as the same reconstruction settings demonstrated similar performance across three different applications and datasets at similar count levels. Although a limited degree of tuning may improve the results, it would be better for reproducibility to use σ_p between 1 and 2 (according to how much noise the data contains) and $\sigma_{dp} = \sigma_{dm}$ between 0.8 and 5. All the other parameters should be set as suggested in Table (4.1).

4.6 Conclusion

In this work, a novel LM hybrid kernelised reconstruction method which takes into account the PET features from the iterative process was proposed. The aim was to improve accuracy in those cases where MR and PET local information is only partially equivalent or completely different. In addition, special emphasis was placed to the reduction of negative bias on low-count circumstances. The proposed reconstruction method offers stable results across varied datasets. The performance for low-count data, obtained with short acquisition times, makes this approach particularly useful in dynamic PET-MR studies. The proposed algorithm, with the settings in Table (4.1), outperformed the other techniques in

terms of CNR, CRC and bias, at fixed iteration number, in regions of high focal uptake, such as suspected carotid plaque lesions.

Chapter 5

Investigation of the Effect of PET-MR Inconsistency in the Kernel Image Reconstruction Method

The HKEM and KEM investigated in the previous chapter are used in this chapter to study how spatial inconsistency between the PET and MR images can influence quantification. This is done by augmenting the MR image with simple translation along one axis before the calculation of the kernel. Section 5.1 contains the introduction and description of the study. Section 5.2 describes the datasets used to study image reconstruction, LM sub-sampling and the experimental methodology. Section 5.3 presents results and a comparison of the different standard algorithms with the proposed one. The results are discussed in Section 5.4 and conclusions are drawn in Section 5.5.

5.1 Introduction

Anatomically-driven algorithms have become popular in PET. The rationale supporting the use of these techniques is based on the assumption that the radiotracer uptake distribution follows specific anatomical patterns. As a consequence, the anatomical information from MR can be used as prior knowledge. As discussed in Chapter 2, several studies have recently implemented and investigated different anatomically-driven techniques, showing that they can suppress noise while preserving resolution that is usually lost through the regularisation process. Different ways of including anatomical information in the reconstruction algorithm include: Bayesian techniques and the kernel method. Bayesian techniques are also subdivided into segmentation-based and segmentation-free, the latter avoids the potential error in segmentation. The kernel method can be divided into hybrid (Gong et al. [2018a]; Chapter 4), where the kernel matrix is extracted from more than one source (for example, PET and MR) and non-hybrid (Hutchcroft et al. [2014]; Wang and Qi [2015]; Novosad and Reader [2016]; and Ellis and Reader [2016]), where the kernel is estimated from one source.

This chapter focuses on the kernel method techniques discussed in Chapter 4. As discussed before, Bland et al. [2017] studied the effect of KEM on simulated dose-reduced datasets, showing improved CNR, but at the cost of possible over-smoothing of features unique to the PET data. To overcome this issue Bland et al. [2018] proposed a method using a spatially constrained MR kernel in order to maintain the noise reduction properties of the conventional kernel method, whilst better retaining the features unique to the PET data. In this chapter the limitations of the anatomically-driven kernel methods, HKEM and KEM, are investigated. In particular, focus is given to circumstances where there is an evi-

dent spatial inconsistency between the MR and PET signal distribution even for perfectly co-registered PET and MR images, and to confirm that synergistic information can improve the flexibility of the reconstruction in these circumstances. This is important because in some cases a PET lesion may be located at the border between two different regions, as shown in Schramm et al. [2018], moreover, it has been shown that PET unique features can be severely over-smoothed (Bland et al. [2017]) with the MR-guided kernel. Strul and Bendriem [1999] investigated the limitations, due to MR segmentation and PET-MR registration, of different segmentation-based partial volume correction techniques in simulation studies. Although the segmentation does not represent a problem for the segmentation free techniques, registration can always represent a problem. The effect on the PET image of PET-MR inconsistencies, is investigated particularly for cold and hot regions that are crossed by MR regions. HKEM and KEM from Chapter 4 were used to reconstruct images for four types of datasets: 5 s and 50 s acquisition with phantom data, and 30 s and 300s acquisition with patient neck data. The MR image was shifted by a different number of pixels along the x direction. All the data were acquired with the Biograph Siemens mMR. Both algorithm implementations use spatially restricted kernels and, thus, reduced smoothing of the PET unique features is expected, compared to the standard patch-based kernel methods, as shown by Bland et al. [2018].

5.2 Methods and Materials

5.2.1 Phantom Experiment

A phantom experiment was performed with a Jaszczak phantom for resolution studies and was acquired with the Siemens Biograph mMR scanner at Mount Sinai Hospital, NY, USA. The phantom consists of cold spheres with different diameters, 13 mm, 10 mm, 9 mm, 7 mm, 6 mm and 4 mm. The background represents the hot region, which was filled with 155 MBq of [^{18}F]FDG, data were acquired over 1 hour. The attenuation image was obtained from an MR volumetric interpolated examination (VIBE) acquisition, segmented into 2 tissue classes (air, water). The MR component of the kernel was obtained from a co-registered MR-VIBE sequence. The original voxel size is $0.35\times0.35\times1$ mm^3. The image is then aligned to the PET field of view (FOV) and re-sliced to match the PET native voxel size, $2.087\times2.087\times2.031$ mm^3, and FOV size, $344\times344\times127$ voxels. The raw PET data were reconstructed in two different cases: 5 s and 50 s frames. These time frames are those at the beginning of the acquisition obtained from the full LM file.

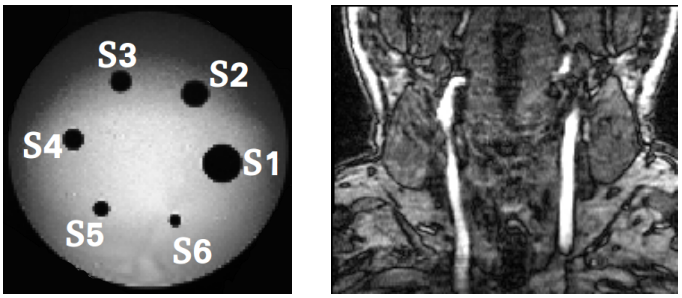

(a) (b)

Figure 5.1: Slices of the MR images used to estimate the kernel matrix for (a) the phantom and (b) the patient studies.

5.2.2 Patient Experiment

The LM-HKEM method was also applied to dynamic data for a patient head and neck data. The acquisition was carried out using the Siemens Biograph mMR at Mount Sinai Hospital, NY, USA, and a consent form was signed by the patient. The patient was injected with [^{18}F]FDG 184 MBq and scanned for 90 minutes. The attenuation images were obtained from the Dixon MR sequence using 4 tissue classes (fat, water, air, lungs), and it contains attenuation coefficients for bed and coils. The LM data were divided into smaller time frames, 30 s and 300 s. The scan started after 10 minutes from the injection of the tracer. Note that the two different durations are considered as two different datasets and the uptake in these datasets is not comparable due to different kinetic behaviour, especially because they are the first time frames after injection. The MR part of the kernel matrix is obtained from a time-of-flight (TOF) MR angiography sequence (Figure (4.2)), the original voxel size is $0.7\times0.7\times1$ mm^3. It is then aligned to the PET field of view (FOV) and re-sliced to match the PET

native voxel size, 2.087×2.087×2.031 mm^3, and FOV size, 344×344×127 voxels. The MR TOF acquisition time is 540 s. A head and neck coil was employed: 3 slabs, each consisting of 60 slices of 1 mm thickness. This image sequence is particularly suitable to study the carotid because it provides high contrast between the carotid arteries and the surrounding tissues.

5.2.3 Reconstruction Setup

All the datasets were reconstructed with 21 subsets and 10 iterations using HKEM and KEM. The subset division for the LM reconstruction in STIR is made by subdividing the events according to the view number. The values of the kernel parameters for this study are set to find the trade-off between quantification and noise suppression while minimizing PET feature suppression: $N = 3 \times 3 \times 3$, $\sigma_m = \sigma_p = 1$, and $\sigma_{dm} = \sigma_{dp} = 5$. These settings have been selected to maximise the CNR following a similar procedure as in the previous chapter.Altough the comparison has been carried out for 10 iterations in this chapter only the 3$^{\text{rd}}$ iteration is reported to reduce the influence of the noise in the quantification. The different time frame durations are obtained by selecting only the events occurred during the first 50 s and 5 s for the phantom, and 300 s and 30 s for the patient. The MR image, for both experiments, was translated by 1, 2, 3, 5 and 10 voxels (as in Figure (5.3)) along the x direction in order to study the effect of non-accurate registration between PET and MR images, and also to introduce differences between the aforementioned images so that different case scenarios are investigated. Note that the attenuation image was not translated so that only the effect of the anatomical image used for the kernel is studied.

5.2.4 Image Analysis

The comparison was carried out in terms of mean activity concentration. Region of interest (ROI) analysis was performed using a sphere in a uniform cold region of the phantom represented by the blue circle in Figure (5.3), and extracted from the MR image. For the patient, the ROI was obtained through a few steps: firstly, the carotid was segmented using the MR image, and used as a mask on the HKEM image; a threshold was applied on the HKEM image only to segment the hot part of the carotid; finally it was cropped to match the shape of the lesion in both the HKEM and KEM image as the shape of the hot lesions are the same between HKEM and KEM. What is different between the HKEM and KEM lesion is the uptake. The ROI was not taken from the MR image because it provides the whole carotid, while the OSEM image is largely affected by PVE. One ROI is used for the 300 s acquisition, and the other for the 30 s acquisition as the kinetics and possible motion make the 2 datasets very different (Figure (5.2)).

Quantitative comparison between algorithms was performed using the following figure of merit:

$$\text{mean} = \frac{\sum_i x_i}{V} \tag{5.1}$$

where x_i is the value of voxel inside the ROI and V is the number of voxels included in the ROI. To estimate the bias images showing the induced error for each MR translation, the reconstructed images with the correct MR is used as ground truth, also labelled as shift=0. The difference between the shifted image and the ground truth is then calculated.

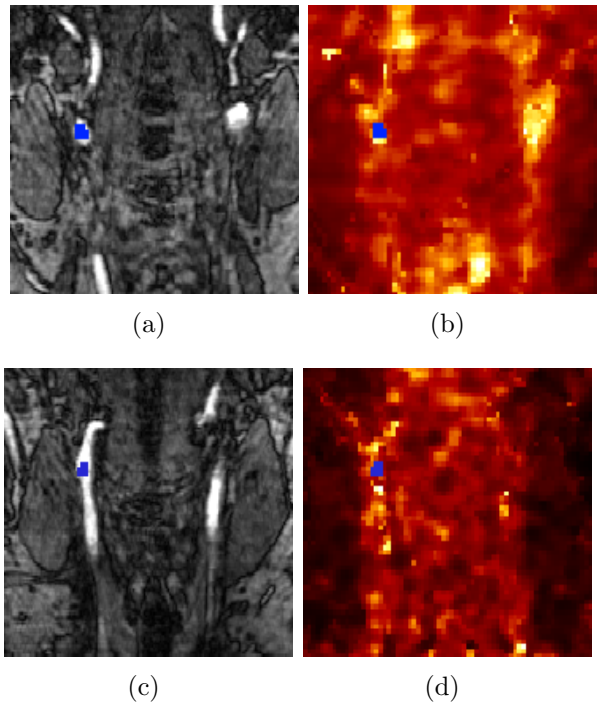

(a) (b)

(c) (d)

Figure 5.2: Regions of interest (ROI) chosen for the patient study: (a) ROI shown on the MR image for the 300 s acquisition, (b) ROI shown on the PET image for the 300 s acquisition, (c) ROI shown on the MR image for the 30 s acquisition, (d) ROI shown on the PET image for the 30 s acquisition. The PET image is obtained with HKEM.

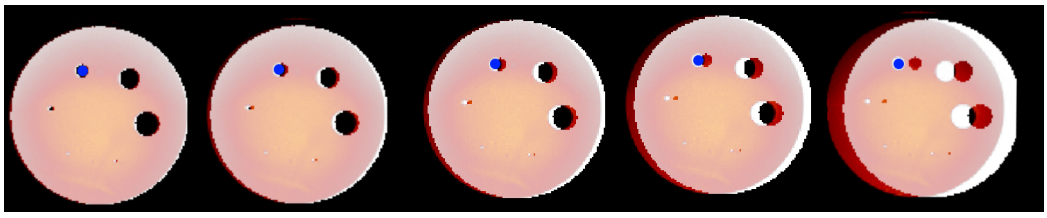

Figure 5.3: Representation of the different shift reproductions using the phantom: from left to right 1, 2, 3, 5, and 10 voxels translation. The blue sphere is the ROI used for the quantification.

5.3 Results

This study shows the effect of the anatomically-driven kernel method on the PET reconstructed images, with a focus on those situations where MR and PET information do not match. To recreate these circumstances the MR image was translated along the x axis creating specific cases, such as a cold PET region partially crossed or surrounded by an MR well-defined region with the phantom data, and hot lesion partially crossed by MR regions with the patient data. All the shifts can be seen in Figure (5.3). The blue circles in the figure help to better understand and locate the area of interest. This investigation was carried out using the hybrid and non-hybrid kernel method in Chapter 4 to explore the limitation of these methods as well as to study whether the hybrid method performs better when small differences between PET and MR images are introduced. The σ_m and σ_p in equations (4.13) and (4.14) were fixed at 1 as it represents the best CNR. The neighbourhood size, N, was set to 3×3×3 to keep computation quick and also to avoid PET unique feature suppression. The values used for the two modulation parameters, σ_{dm} and σ_{dp}, were set to 5 which was the optimum value in terms of quantification and noise suppression. Figure (5.4) shows the images reconstructed with OSEM using 5 mm Gaussian post-filter, and KEM and HKEM with the correct MR image, for Jaszczak phantom 50 s acquisition (a), Jaszczak phantom with 5 s acquisition (b), patient data with 300 s acquisition (c), patient data with 30 s acquisition (d). Figure (5.5) shows the quantitative results for the 50 s acquisition phantom datasets. The x axis reports the shift in terms of the number of voxels, while the y axis is the mean value in the ROI, calculated with equation (5.1). The OSEM ROI mean value (with no post filtering) is also reported for reference. The coloured bar

reports the range of coefficient of variation (CoV) values in the plot. In Figure (5.6) an image-based comparison for the 50 s acquisition phantom datasets is shown, where it is possible to appreciate the effects of the different translations on HKEM and KEM. The bias in all the image voxels is shown in Figure (5.7); and the zoomed cold spheres for the case where the MR image was translated by 10 voxels in Figure (5.8). The same experiment was repeated for the 5 s acquisition and the quantitative analysis is reported in Figures (5.9)-(5.12).

Figure (5.13) reports the mean ROI value as a function of the shift for the patient data obtained from 300 s acquisition. The OSEM ROI mean value is also reported for reference. The coloured bar reports the range of CoV values in the plot. Figure (5.14) shows the reconstructed images with each translation, while Figure (5.15) reports the bias images estimated as the difference between the image reconstructed with the correct MR and the image obtained using each translated MR. The same is repeated for the 30 s acquisition, where image-based and quantitative results are shown in Figures (5.16), (5.17) and (5.18) respectively.

5.4 Discussion

The images in Figure (5.4) show the improvements, in terms of contrast and resolution, provided by the two anatomically-driven kernelised method over the OSEM. With the Jaszczak phantom the effect of the PET-MR misalignment was investigated on cold spheres: in Figure (5.5) the ROI mean shows how the mean value, which is supposed to be zero, increases as the shift increases, with a significantly stronger effect for KEM. The maximum increase is 100% for

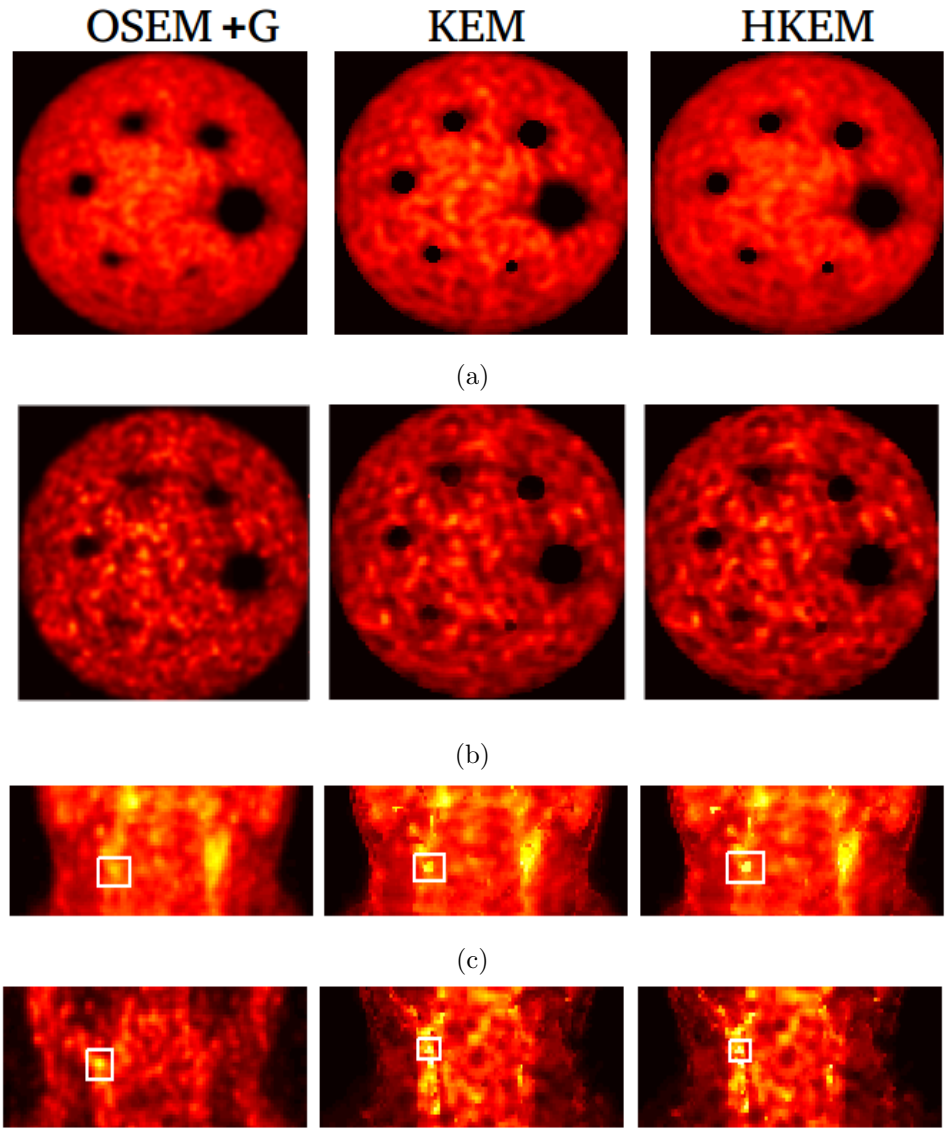

Figure 5.4: Reconstructed images with OSEM+G, KEM, and no shift, and HKEM with no shift, on all the datasets and count-levels. (a) Jaszczak phantom 50 s acqusition; (b) Jaszczak phantom 5 s; (c) patient 300 s acqusition; (d) patient 30 s acqusition acqusition.

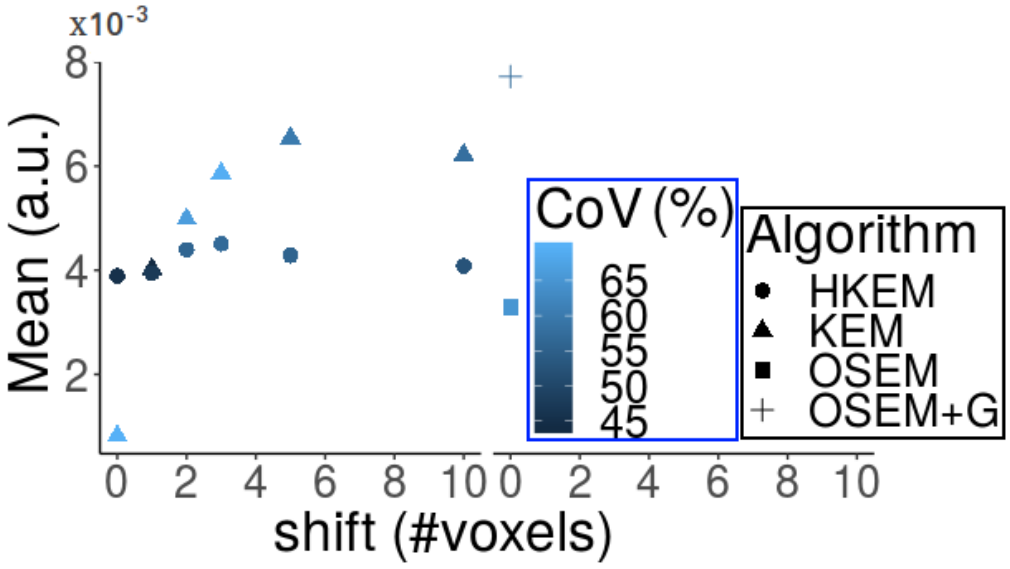

Figure 5.5: Mean activity concentration comparison between reconstructed phantom image with HKEM and OSEM on 50 s acquisition with the Jaszczak phantom. The x axis is the MR image shift in terms of number of voxels.

KEM against the 37% of HKEM. This is due to the introduction of the PET information in the kernel, which makes HKEM more flexible allowing the PET borders to be restored. The increase in activity along with the shift seems to indicate that the activity was pushed from its original position to the area after the MR border. Figure (5.6) shows the same result visually, where the effect of the difference between PET and MR can already be seen for the 1 voxel shift for both HKEM and KEM. In Figure (5.7) bias appears close to the borders of the MR and PET images. In particular, positive bias can be seen in the cold region and negative bias in the hot regions close to the borders. From this figure and from Figure (5.8) it is also possible to see that the smoothing effect is more visible for the smaller spheres.

For the 5 s acquisition, Figure (5.9) shows more moderate variation than the

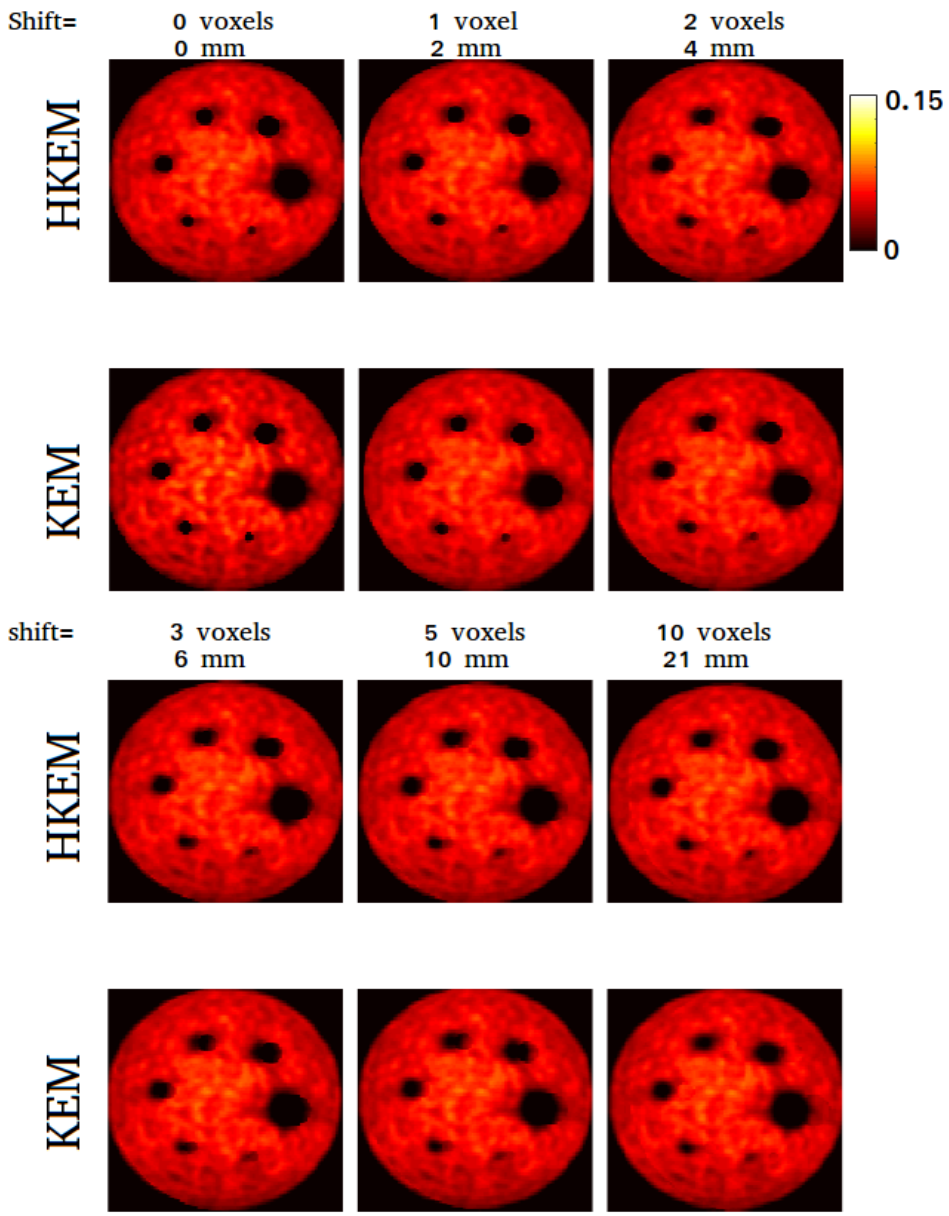

Figure 5.6: Reconstructed images with KEM and HKEM on 50 s acquisition. Each column represents a different shift (the first one is without shift), in terms of number of voxels.

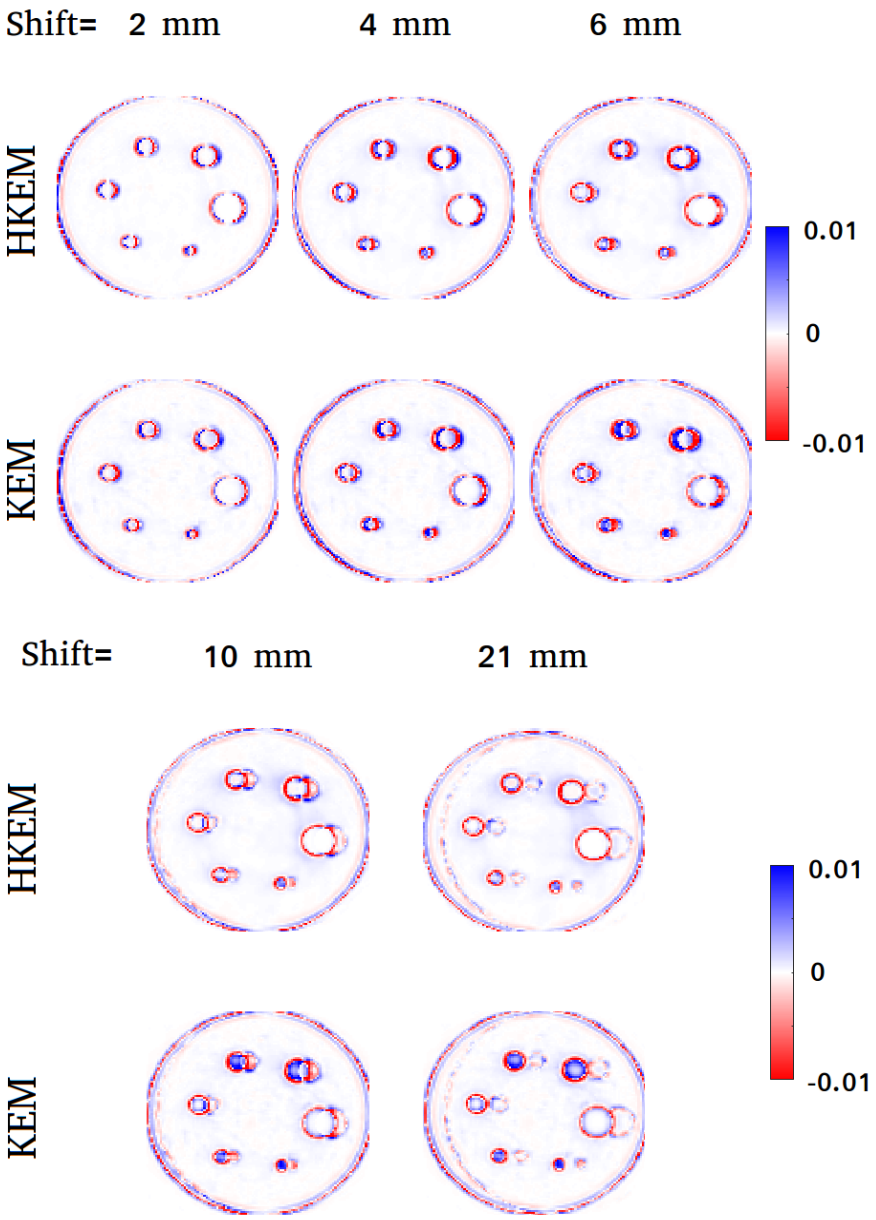

Figure 5.7: Comparison between bias images with KEM and HKEM on 50 s acquisition. Each column represents a different shift, in terms of number of voxels. Reconstructed images with the correct MR are used as ground truth;

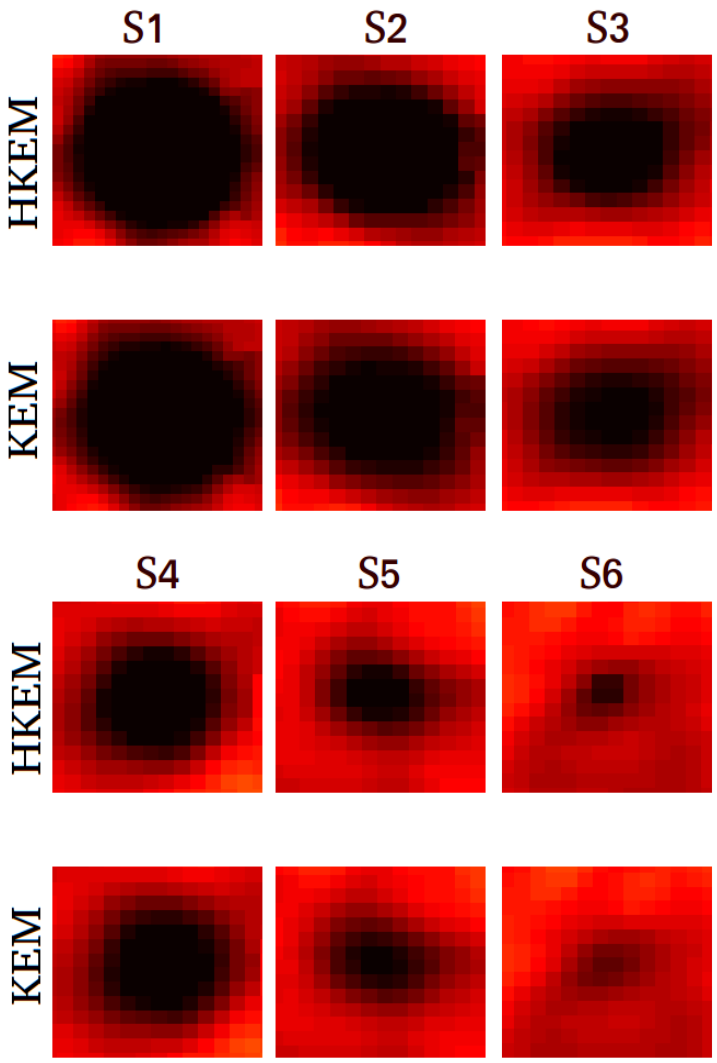

Figure 5.8: Zoom of the cold spheres of the Jaszczak phantom for the 50 s images and the case with shift = 0 voxels with HKEM and KEM.

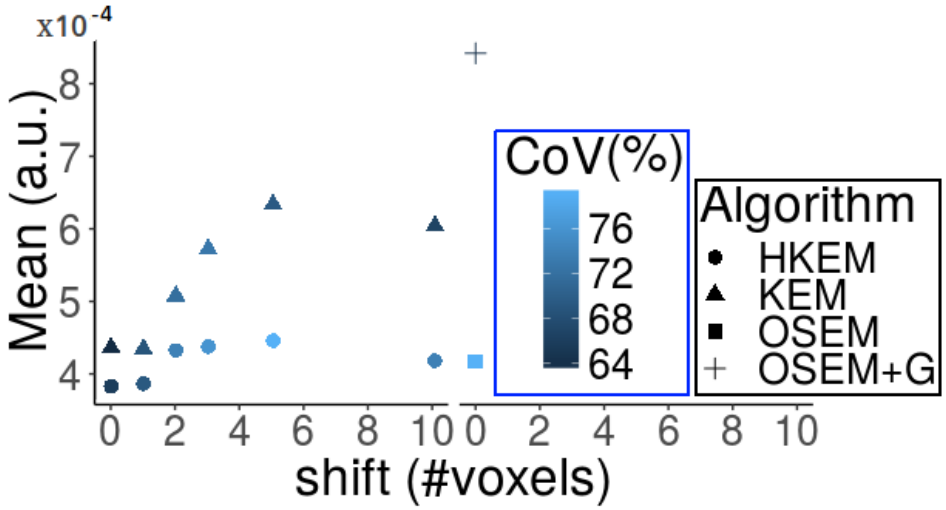

Figure 5.9: Mean activity concentration comparison between reconstructed phantom image with HKEM and OSEM on 5 s acquisition with the Jaszczak phantom. The x axis is the MR image shift in terms of number of voxels.

higher count case. In this case the maximum variation was 33% for KEM and 15% for HKEM with the 5 voxels shift. The fact that the short acquisition shows less quantitative change than the 50 s acquisition is probably due to the fact that the noise here has a more important impact and there is already an increased uptake even with the correct MR image. In fact, the OSEM value is close to the 'wrong' HKEM value. Looking at the zoomed spheres in Figure (5.12) it is possible to see that the degradation is actually more visible for the low count. Note also that in Figure (5.12) the zoom for each sphere is different to allow a better visual recognition. That is why the size does not appear in a decreasing order.

With the patient data, the effect of the PET-MR inconsistency was shown on hot lesions in the carotid artery. In contrast to the phantom data, here it is more difficult to visually detect the effects because the human body is more

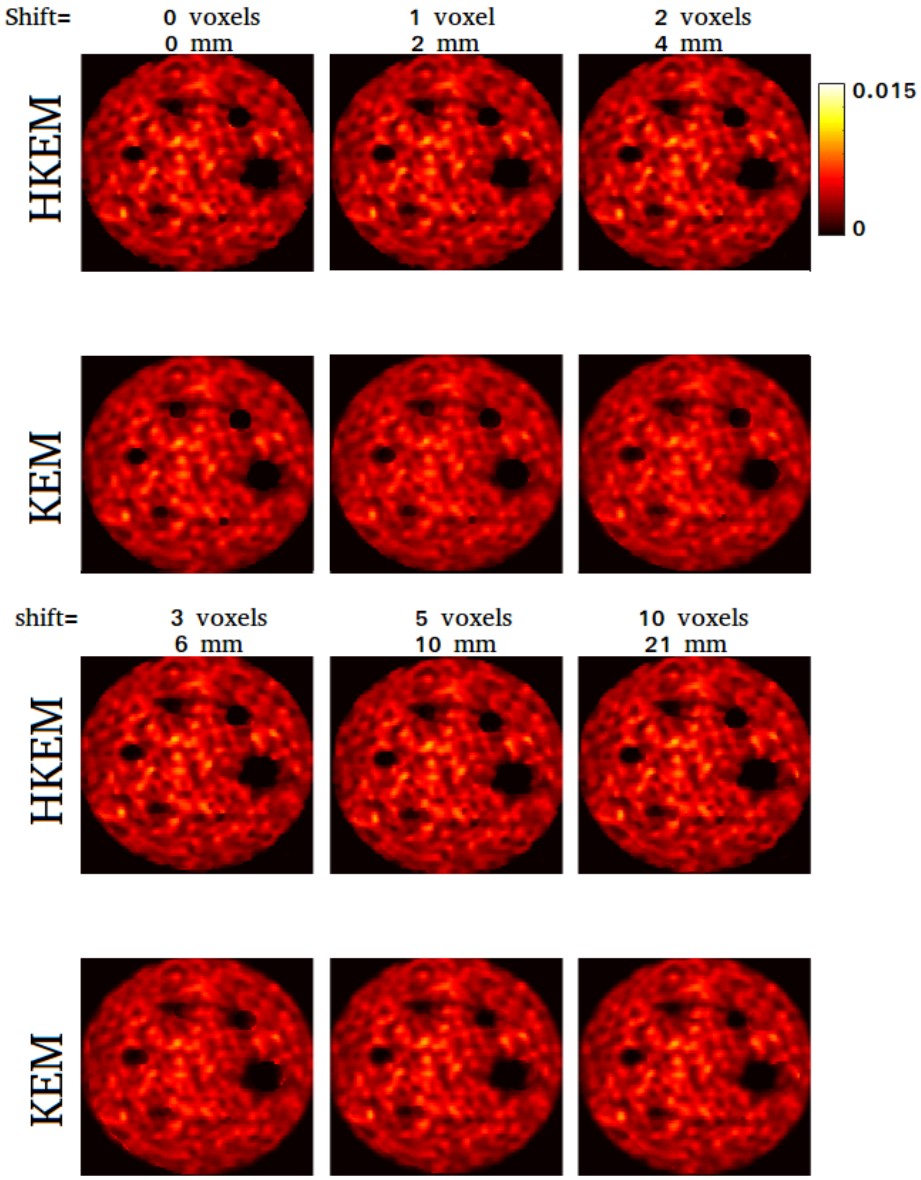

Figure 5.10: Reconstructed phantom images with KEM and HKEM on 5 s acquisition. Each column represents a different shift (the first one is without shift), in terms of number of voxels.

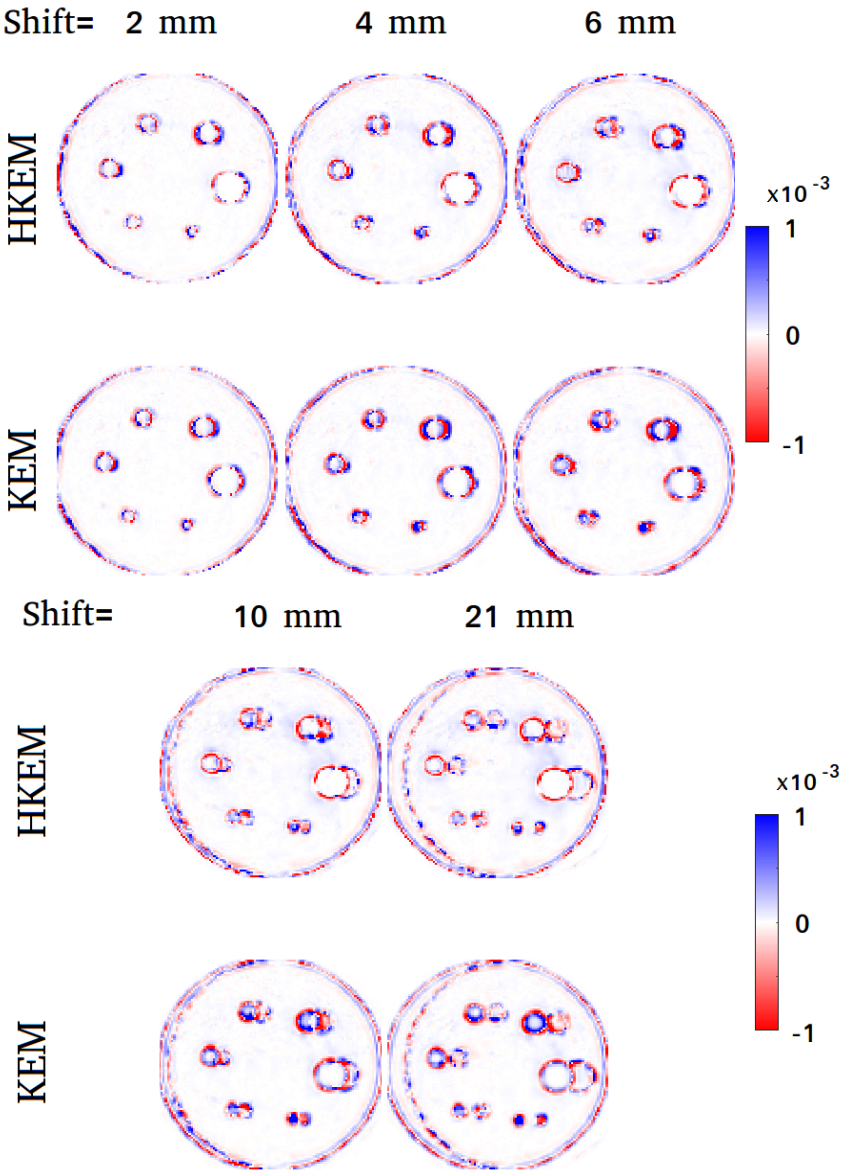

Figure 5.11: Comparison between bias images with KEM and HKEM on 5 s acquisition. Each column represents a different shift, in terms of number of voxels. Reconstructed images with the correct MR are used as ground truth.

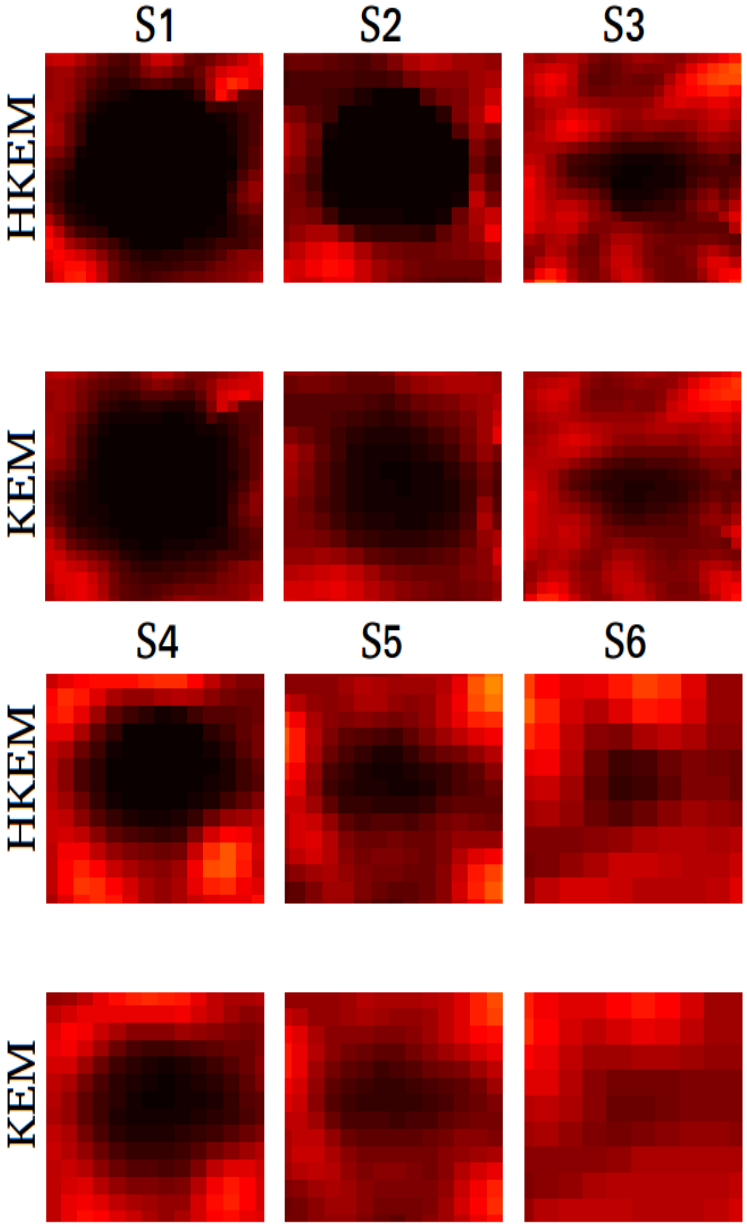

Figure 5.12: Zoom of the cold spheres of the Jaszczak phantom for the 5 s images and the case with shift = 0 voxels with HKEM and KEM.

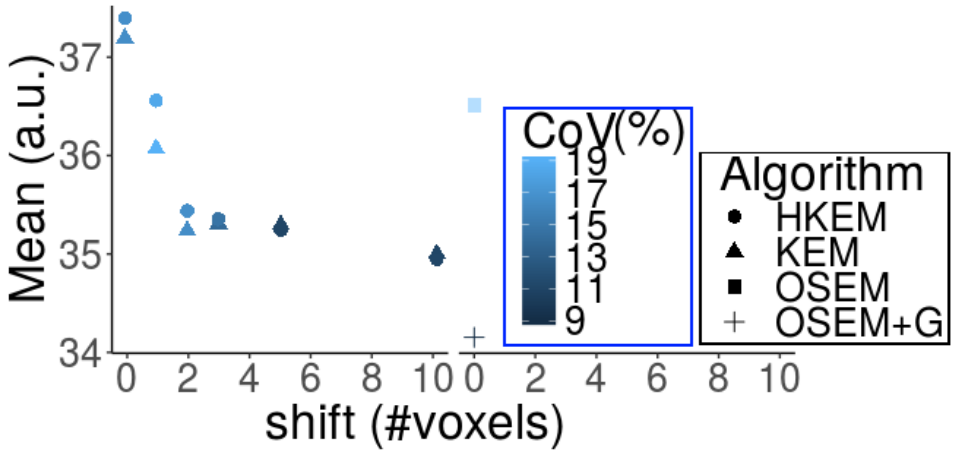

Figure 5.13: Mean activity concentration comparison between reconstructed patient image with KEM, HKEM and OSEM on 300 s acquisition. The x axis is the MR image shift in terms of number of voxels.

complicated and there is a wider variety of tissues in the MR image. Figure (5.13) shows the consequences of translation for the 300 s acquisition. An instant drop in uptakes can be seen as soon as the shift takes place. The HKEM performs better for the small shifts, however, after the 2 voxels translation it behaves similarly to the KEM with a maximum variation of 7% for both. Although the ROI analysis for the hot regions show more moderate variation than the case of the cold spheres, in Figure (5.14), it is possible to see that the shape of the lesion changes with the shift and gradually becomes blurred. Also, in Figure (5.15) negative and positive bias can be seen all over the image, which can reach ±50% in certain locations. The ROI quantification for the 30 s acquisition, as reported in Figure (5.16), shows slightly larger variation with a maximum of 10% for KEM and 8% for HKEM. In this case, HKEM performs better in all translations except the 5 voxel translation. Similarly to the 300 s case, in Figure (5.17) it is possible to see the gradual blurring of the lesion and the variation

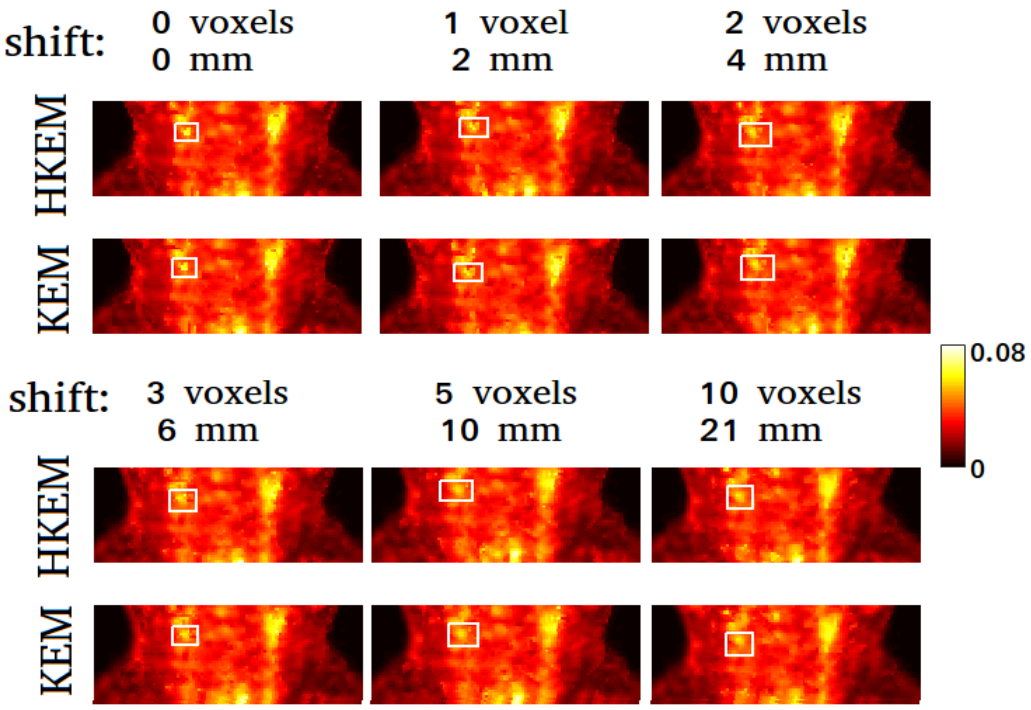

(a)

Figure 5.14: Reconstructed patient images with KEM and HKEM on 300 s acquisition using different translations; The different columns represent a different shift (the first one is without shift).

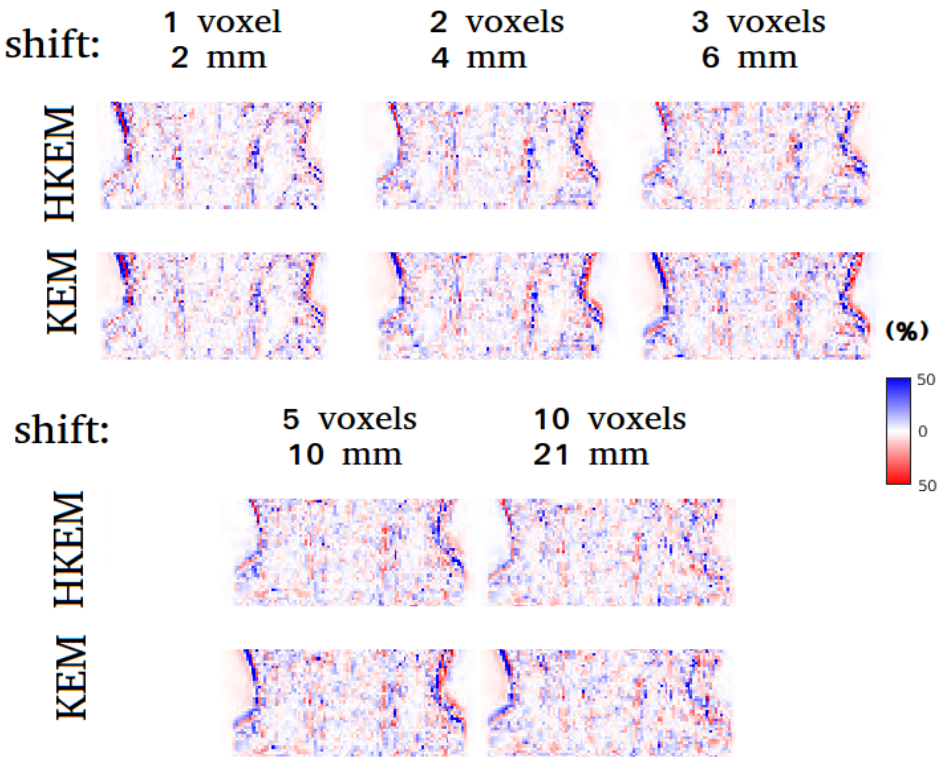

Figure 5.15: Comparison between bias images with KEM and HKEM on 300 s patient acquisition. Each column represents a different shift, in terms of number of voxels. Reconstructed images with the correct MR are used as ground truth.

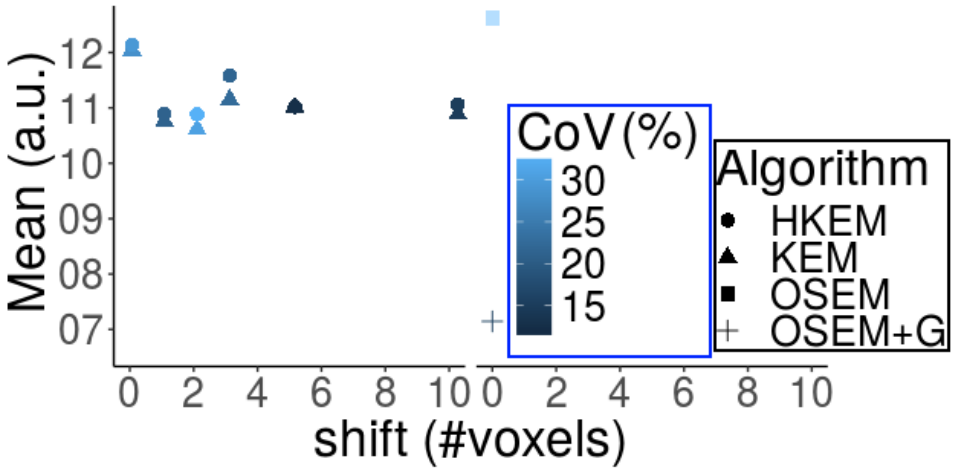

Figure 5.16: Mean activity concentration comparison between reconstructed patient image with KEM, and HKEM and OSEM on 30 s acquisition. The x axis is the MR image shift in terms of number of voxels.

voxel by voxel for all shifts. The dark blue and the dark red areas in Figures (5.15) and (5.18) represent voxel bias up to $\pm 50\%$ and it is more significant for the low-count case. Note that, 2 cm of motion is probably too big to be missed, and this type of motion can be corrected by registration. However, in this case the effect of the uniform MR area of the neck overlaying the carotid artery of the PET image was studied. This represents, for example, cases where a high uptake region in PET does not show any signal in the MR. Note that there were no PET-MR mismatches in the attenuation map so that only the effect of the anatomical image used for the kernel is studied. The artefacts due to attenuation mismatches may be, however, so significant that the error due to the kernel part would not be a problem in comparison (Schleyer et al. [2010]).

In general, the PET-MR inconsistencies can induce partial volume effects, more specifically spill-in for the affected cold regions and spill-out for the hot regions. The largest errors are introduced for the cold spheres than the hot

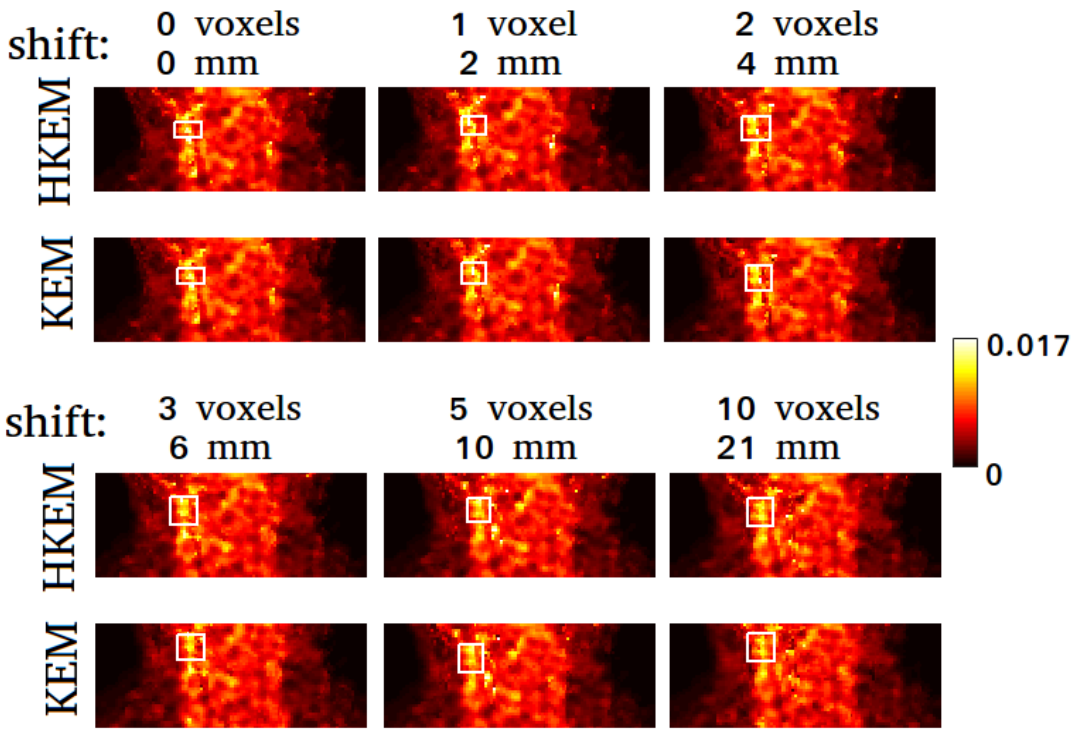

Figure 5.17: Reconstructed patient images with KEM, HKEM on 30 s acquisition using different translations ; The different columns represent a different shift (the first one is without shift), in terms of number of voxels.

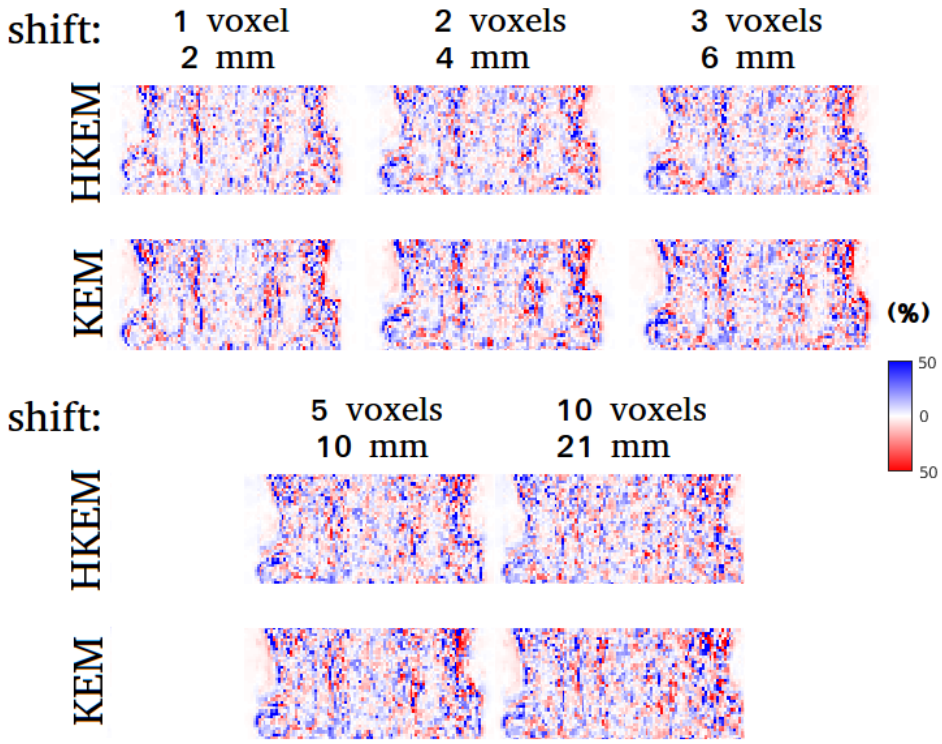

Figure 5.18: Comparison between bias images with KEM and HKEM on 30 s patient acquisition. Each column represents a different shift, in terms of number of voxels. Reconstructed images with the correct MR are used as ground truth.

lesions. In this case the HKEM appears more flexible thanks to the PET information included in the kernel. The average ROI error for the hot lesions was always smaller or equal to 10% and the HKEM outperformed KEM only in some cases while they behave similarly in others. Finally, although the PET-MR spatial inconsistencies introduce voxel variations and errors, it is a consistent result over the datasets that the application of a 5 mm Gaussian filter provides a bigger PVE than the one created by any MR translation generated, when the attenuation map does not contain mismatches. This can be seen from Figure (5.5), (5.9), (5.13) and (5.16). The findings highlight the increased flexibility of both HKEM and KEM compared to the clinical gold standard, OSEM, and the importance of a well-chosen MR sequence to use as anatomical information, as well as an accurate registration between PET and MR. In fact, to obtain the most accurate result, a study making use of anatomical information should be thoroughly planned according to the region of interest one wants to study in order to avoid unwanted artifacts and erroneous quantification.

5.5 Conclusion

In this chapter, the effect of mismatches between PET and MR images was investigated, for cold and hot regions, when the kernel method is used with MR information for PET reconstructed images. It was shown that even small changes in the MR can result in a change in quantification and increase in blurring. However, hybrid information can help to reduce these effects, especially in the case of cold regions. The ideal solution is to avoid MR sequences having tissue-borders crossing the PET ROI as well as very accurate PET-MR registration. In

addition, creating a protocol where the chosen MR sequence is acquired during the PET scan would minimise the PET-MR inconsistencies.

Chapter 6

Hybrid PET-MR KEM Reconstruction for Accurate Image-Derived Estimation of the Input Function From the Aorta of Rabbits

In this chapter the HKEM introduced and discussed in Chapter 4 is applied to the estimation of the rabbit aorta IDIF. In particular, the HKEM is used for the reconstruction of the image which is also used for the extraction of the ROI with the aim of producing an accurate estimation of the IDIF. For this study a simulation based on rabbit dynamic data was created, and a demonstration code to simulate, reconstruct and extract the ROI, was made available in Code Ocean (Deidda [2018]). Section 6.1 introduces the issues related to the estimation of the

IDIF and explore some of the work available in the literature. The methodology of the study, with the realisation of the simulation, the acquisition of the real data and the explanation of the method for the ROI extraction is discussed in Section 6.2. The results are shown and discussed in Sections 6.3 and 6.4 and the conclusion of this chapter are in Section 6.5.

6.1 Introduction

[^{18}F]-based PET imaging has been used successfully as a non-invasive imaging biomarker of different human diseases. [^{18}F]NaF is associated with calcium molecular metabolism and has been used to study benign osseous diseases such as osteoporosis, vascular calcification, osteoarthritis, rheumatoid arthritis and so on (Raynor et al. [2016]; and Li et al. [2012]). [^{18}F]NaF has been proposed, for example, as a quantitative pharmacodynamic biomarker for bone homeostasis during anti-DKK1 therapy for multiple myeloma (Wang et al. [2017]), for the quantification of skeletal kinetic indices in Paget's disease (Cook et al. [2002]), and to determine therapy efficacy and response (Frost et al. [2013]; and Simoncic et al. [2015]). [^{18}F]FDG is the most commonly used tracer in clinical practise and particularly for the detection, quantification, staging and therapy evaluation of cancerous lesions (O'Connor et al. [2017]), as well as in cardiovascular and neurological diseases (Wu et al. [2013]). It can be used for the estimation of the volumetric growth rate of tumours from pre-treatment to post-treatment imaging as shown by Seyal et al. [2014] for breast cancer liver metastases and Seyal et al. [2015] for colorectal liver metastases. In addition, it is used for the localisation, and quantification of inflammation in arteries (Alenezi et al. [2016];

Jødal et al. [2017]) and so on. The availability of preclinical PET studies has allowed the calculation of molecular biomarkers at the preclinical stage with small animals being used in the context of clinical trials.

All the aforementioned applications of [^{18}F]-based PET imaging have in common the requirement of the accurate measurement of the IDIF, especially in the context of clinical translation. PET imaging in general can provide more accurate and precise quantitative biomarkers by exploiting the pharmacokinetic information which is inherited in the measured data (Kotasidis et al. [2014]). However, in most cases for the calculation of the pharmacokinetic parameters, the radiotracer concentration in the arterial blood plasma (input function) is required. The gold standard for such measurement is blood sampling during the PET acquisition, via arterial cannulation (Bentourkia [2015]). However, such techniques are invasive and can be complicated, as it requires arterial blood samples in specific quantities and at precise times and corrections for delay and dispersion to account for the distance between the sampling site and the ROIs (Fung and Carson [2013]).

A non-invasive technique is the IDIF which uses a ROI to measure the uptake in the vessel over time. The IDIF is a simple way to calculate activity over time, however, it is challenging due to image related issues. Firstly, the choice of the ROI has a very important impact and erroneous ROIs will affect the accuracy. Secondly, as discussed in the previous chapters, PET image quality is degraded by the PVE which can cause spill-in of activity in cold region and spill-out from hot region. Other challenges are related to the use of MR images to extract the ROI, because a potentially inaccurate registration between PET and MR images can lead to erroneous estimates of the activity in the chosen arterial ROI. With

hybrid PET-MR scanners, however, the problem of co-registration is expected to be minimised.

The aforementioned problems are mostly related to the ordered subset expectation maximisation (OSEM) which is usually followed by post reconstruction Gaussian filtering due to the high noise levels expected for the very narrow time frames used for the IDIF estimation. In preclinical experiments these issues can be even more challenging (Tsoumpas et al. [2016]) because of the smaller size of animal vessel tissues, such as rabbit aortas, especially when they are performed with clinical scanners designed for human subjects. In this case, the PVE can be significant, as the diameter of the rabbit aorta is about 5 mm, which is comparable to the order of magnitude of the PET resolution.

Different studies have proposed methods for the use of IDIF by correcting or avoiding PVE (Germano et al. [1992]; Lin et al. [1995]; Litton [1997]; and Laforest et al. [2005]). Nevertheless, Zanotti-Fregonara et al. [2011], have shown in their comparison between cannulation-based and image-derived input functions that the use of high resolution PET images is often not enough to avoid the use of blood samples to obtain a reliable IDIF. Moreover, the accuracy of the IDIF may vary between radiotracers and scanners. The HKEM algorithm, introduced and validated in Chapter 4 as a method for improving PET image resolution and uptake recovery in PET-MR phantom experiments, as well as contrast and quantification of atherosclerotic plaque lesions in carotid arteries in clinical PET-MR studies, is used in this study to minimise PVE during the reconstruction step so that it is possible to obtain more accurate IDIF estimates. The HKEM reconstructed image at the peak activity time frame was used together with the MR image to extract the ROI to be used for the estimation of the input function.

This chapter focuses on the quantification of the aorta IDIF of rabbits using ^{18}F based radiotracers such as [^{18}F]FDG and [^{18}F]NaF, to extend the applicability and usefulness of HKEM. Here it was assumed that if HKEM can recover the uptake while retaining satisfactory noise suppression for low-count PET acquisitions, it will also be capable of providing accurate IDIF estimates using a wide range of dynamic PET time frame durations.

6.2 Methods and Materials

6.2.1 Simulation and real datasets

A realistic simulation was created using a model derived from real [^{18}F]NaF rabbit data and utilities implemented in the STIR library. The real data were acquired with the Siemens Biograph mMR scanner at Mount Sinai Hospital, NY, USA. The voxel size for the simulated image was 1.56×1.56×2.031 mm^3. The rabbit was a healthy subject and was anaesthetised before the scan. It was injected with [^{18}F]NaF 170 MBq and scanned for 90 minutes. Different organs and tissues were segmented from the acquired MR UTE sequence, using 0.07 ms echo time. The original voxel size was 1.56×1.56×1.56 mm^3. It is then aligned to the PET field of view (FOV) and re-sliced to match the PET native z voxel size, 1.56×1.56×2.031 mm^3, and FOV size, 344×344×127 voxels. The same image is also used for the calculation of the kernel matrix. The acquisition is the same for the real data. In particular, the abdominal aorta, kidneys, bladder, myocardium, lungs, stomach and background were extracted as independent images. Each one of the aforementioned tissue images was used as a ROI in the real PET data which had been divided into 45 time frames organised as follows: 17×6 s, 4×15 s, 4

×30 s, 4 ×60 s, 4 ×180 s, 12 ×300 s. For every tissue type, a file containing the activity concentration at each time point is saved, which was then used to create 45 images of the same tissue with varying activity concentration.

In order to create the projection data, each simulated image is forward projected into the sinogram space. The attenuation sinogram is estimated using the attenuation coefficient, obtained from a Dixon MR sequence, and the precalculated hardware attenuation coefficients for the bed and coils. The projection data containing random events was estimated as a uniform sinogram containing 20% of the total number of events in the simulated acquisition sinogram. In order to estimate the scattered events the single scatter simulation, proposed by Watson et al. [1996], was applied, and a mask obtained from the attenuation map was used for the tail fitting. At this point, the random and scatter sinograms were added to the emission sinogram to create the modelled prompts projection data. The final step was the simulation of Poisson noise from the prompts events.

The above steps were repeated for each simulated time frame and for each 10 independent noise realisations.

6.2.2 Real Rabbit Data

The acquisition was carried out using the Siemens Biograph mMR at Mount Sinai Hospital, NY, USA. The rabbit was an healthy subject and was anaesthetised for the scan. They were injected with [^{18}F]NaF 170 MBq for the first study and [^{18}F]FDG 133 MBq for the second, both scanned for 90 minutes. The attenuation images were obtained from the scanner, included attenuation coefficient for bed and coils. The LM data were divided into smaller time frames, in order to reproduce the input function. The tracer was injected during the first seconds

of the scan. The MR part of the kernel matrix is obtained from a MR UTE sequence with 0.07 ms echo time, the original voxel size is 1.56×1.56×1.56 mm^3. It is then aligned to the PET field of view (FOV) and re-sliced to match the PET native z voxel size, 1.56×1.56×2.031 mm^3, and FOV size, 344×344×127 voxels.

6.2.3 Reconstruction Setup

All the datasets were reconstructed using HKEM with 21 subsets and 10 iterations. The results are reported for the 10^{th} iteration which is the iteration with the minimum RMSE. The values of the kernel parameters were set as follows: N=27, σ_m=1, σ_{dm}=3, σ_p=1 and σ_{dp}=3 (the last two are only used by HKEM). These values are the results of an optimisation study in terms of RMSE on the simulated data for both KEM and HKEM. For comparison, the same datasets have been reconstructed also with OSEM with and without 3 mm FWHM Gaussian post-filter. These methods are denoted as OSEM+G and OSEM, respectively, in this study. All datasets were reconstructed using span 1.

6.2.4 Image Analysis

The comparison was carried out in terms of the mean value for all of the short time frames and datasets, and the bias was estimated to assess the accuracy of the proposed method. The ROI was obtained using the HKEM reconstructed image and the MR image as follows (also see Figure (6.1)):

- the aorta was segmented from the MR image using the semi-automatic segmentation method in ITK-SNAP based on thresholding (Yushkevich et al. [2006]);

- the obtained mask is multiplied by the HKEM reconstructed PET image to obtain the segmented aorta, A^s, from the PET image;

- the ROI, A, is obtained by taking into account only the voxels with value bigger than 75% of the maximum in order to minimise those affected by PVE, as follows:

$$A_i = \begin{cases} 1, & A_i^s \geq 0.75 \cdot A_{max}^s \\ 0, & \text{otherwise} \end{cases} \tag{6.1}$$

where i is the index of the voxel.

Quantitative comparison between algorithms was performed using the following figures of merit:

$$\text{mean}_k = t_k = \frac{\sum_{j=1}^{V} t_{jk}}{V}, \tag{6.2}$$

$$\text{absoulute bias}_k = \frac{\mid t_k - A_k^T \mid}{A_k^T} \cdot 100, \tag{6.3}$$

where t_k is the mean value of the target ROI at time frame k, t_{jk} is the value of voxel j within the ROI at time frame k, and V is the number of voxels within the ROI. The ROIs obtained with the proposed method are shown for each dataset in Figure (6.2).

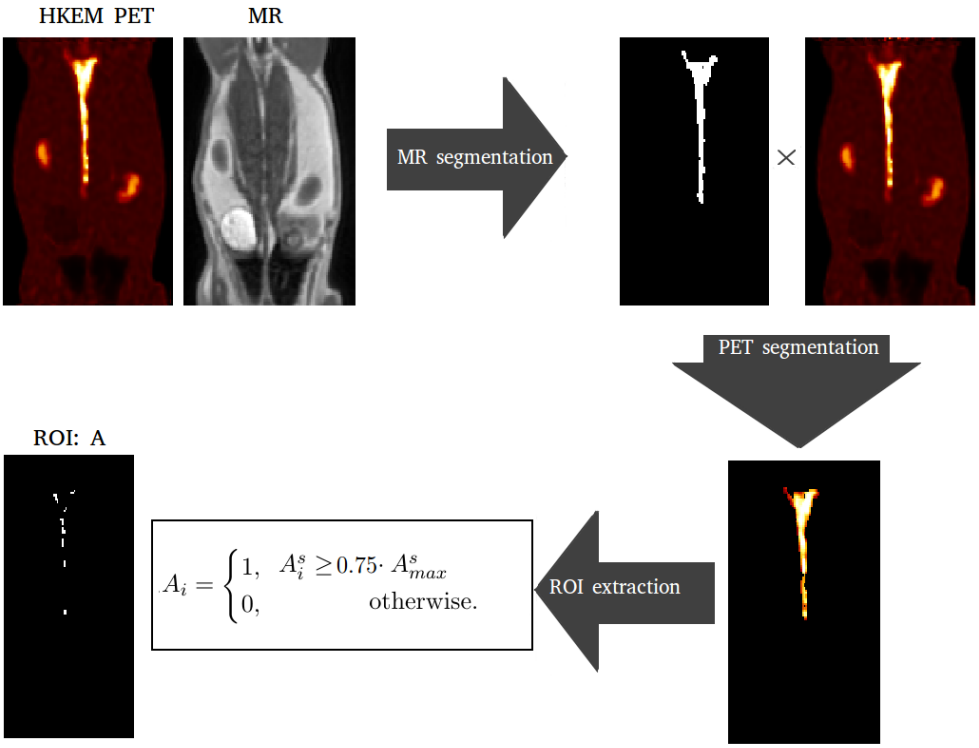

Figure 6.1: Schematic representation of the extraction of the region of interest (ROI), A, of the aorta using the PET and MR images as the input.

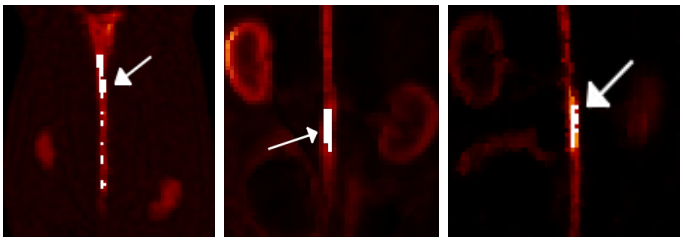

(a) (b) (c)

Figure 6.2: Regions of interest (ROI) chosen for this study, defined by the white regions: (a) the target ROI for the aorta in the simulation; (b) [^{18}F]NaF rabbit study and (c) for the [^{18}F]FDG rabbit study. The target ROIs are indicated by the white arrows.

6.3 Results

6.3.1 Simulation

Figure 6.3 shows the RMSE versus the threshold applied to the ROI for 2 different time frames: 5 (24-30 s) and 33 (1062-1242 s). The IDIF estimates for the simulated rabbit data and the early and late time frames for the IDIF are illustrated in Figure (6.4). In the same figure the reconstructed images with OSEM, OSEM+G, KEM, and HKEM, at the peak time frame (24-30 s), are shown. Figure (6.5) presents the line profile of the aorta estimated for the images, as reconstructed with all investigated methods, at two different positions (LP1 and LP2), whilst Figure (6.6) reports the median IDIF estimated over the ten noise realisations using the HKEM. The shaded region is the range of possible values over the 10 simulated datasets, and the dashed line is the true IDIF. Finally, Table (6.1), reports the percentage value of the mean, maximum, and minimum

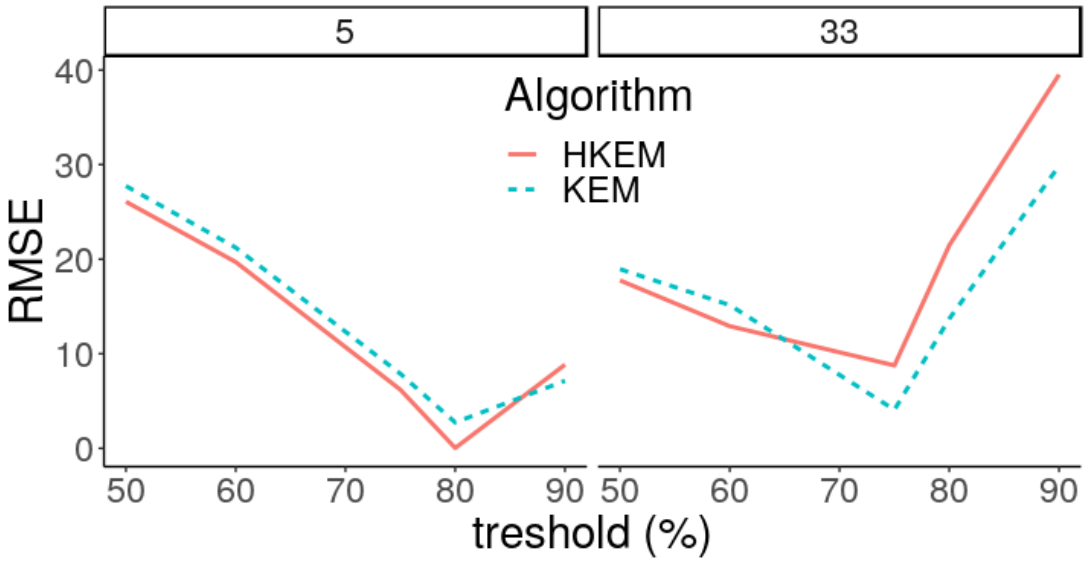

Figure 6.3: The figure shows the RMSE versus the threshold applied to the ROI for 2 different time frames: 5 (24-30 s) and 33 (1062-1242 s). The comparison reports the values measured from the reconstructed images with HKEM and KEM.

absolute bias over the time frames and the noise realisations.

Absolute bias (%) and CoV (%) estimation over the 45 time frames						
	mean bias	Max bias	Min bias	mean CoV	Max CoV	Min CoV
OSEM	6.3	20.8	0.1	52.0	75.6	31.5
OSEM+G	23.32	39.2	4.4	16.2	34.9	10.1
KEM	12.8	30.2	7.7	19.3	30.4	10.9
HKEM	5.0	16.1	0.8	19.9	32.8	10.7

Table 6.1: Absolute bias (%) and CoV (%) estimation over the 45 time frames.

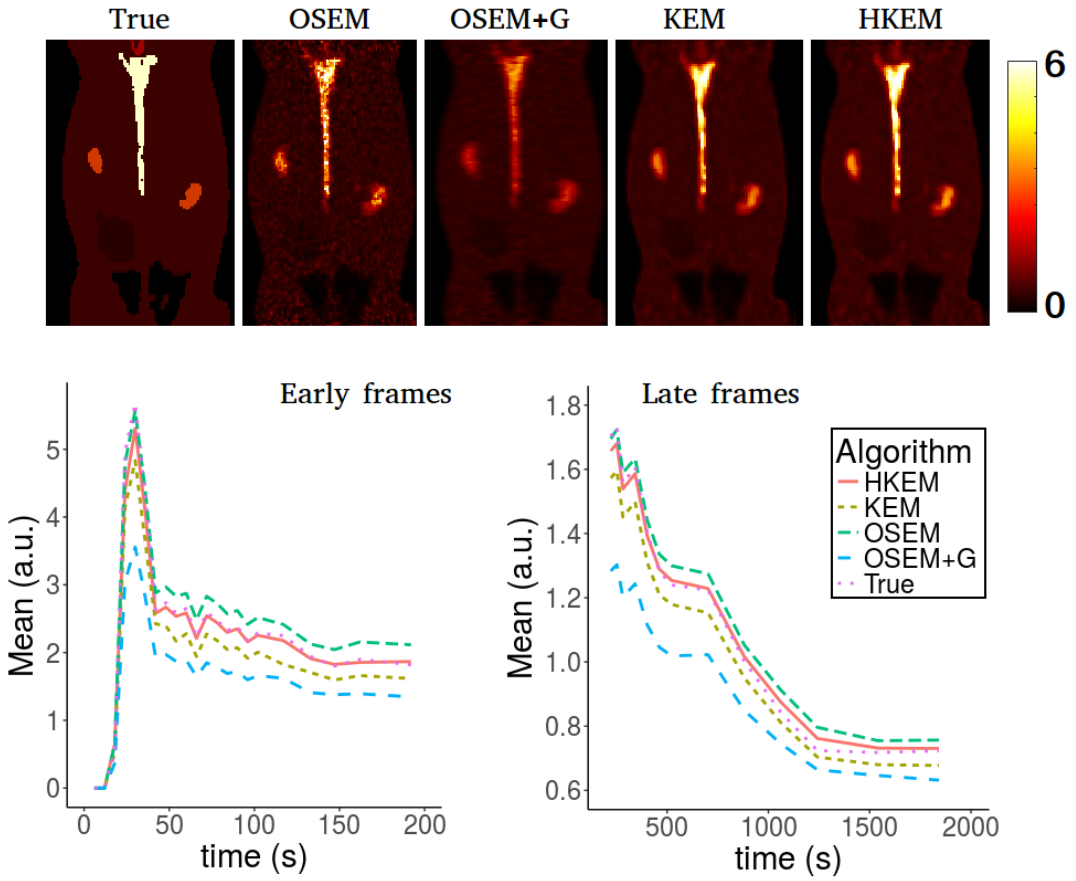

Figure 6.4: The figure shows a comparison between the true and the measured IDIF values over time, as obtained from the reconstructed image with HKEM, KEM, OSEM and OSEM+G. On the top row the peak time frame (24-30 s) images are also shown.

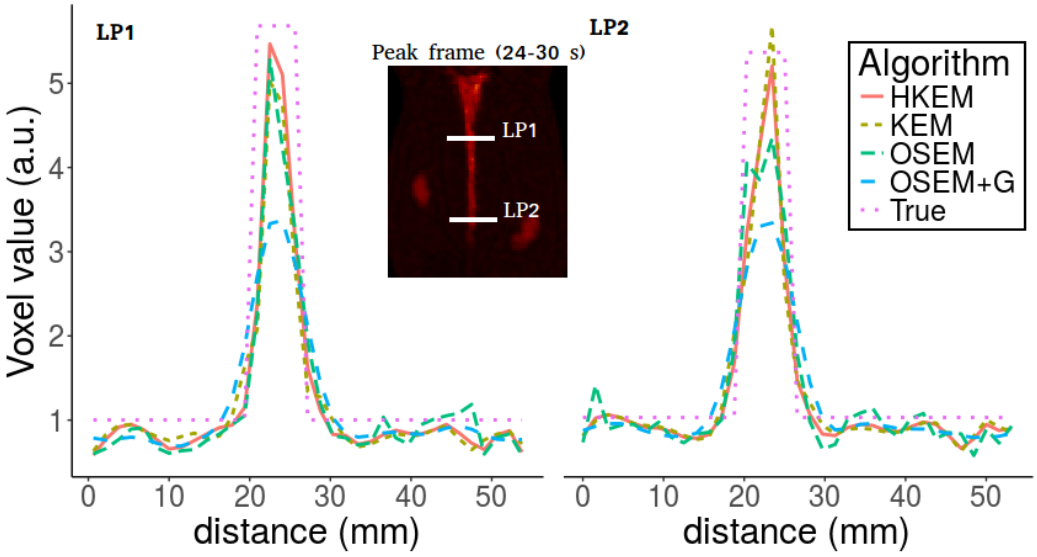

Figure 6.5: The figure shows a comparison between the true line profiles, LP1 and LP2, and the ones obtained from the reconstructed image with OSEM, OSEM+G, KEM, and HKEM.

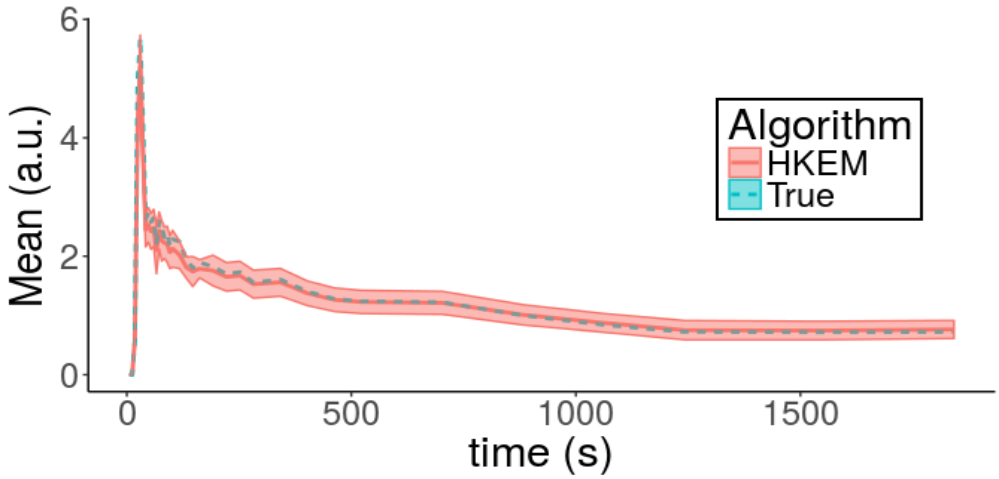

Figure 6.6: Median IDIF estimated over the ten noise realisations using the HKEM. The shaded region is the range of possible values over the 10 simulated datasets, and the dashed line is the true IDIF.

6.3.2 NaF study

Figure (6.7) shows the comparison, on the bottom row, between the initial 200 s of the input function on the left, and the later section of the IDIF, on the right. Moreover, to give an idea of the image quality, the reconstructed [^{18}F]NaF images for the peak time are shown in the top row. Figure (6.8) reports the line profiles of the aorta in two different positions (LP1 and LP2) for the [^{18}F]NaF peak images reconstructed with the investigated methods to illustrate in detail the differences between the images reconstructed with different techniques. Figure (6.9) gives an example of the fused PET-MR images for all the reconstruction techniques.

6.3.3 FDG study

The IDIF was estimated for a [^{18}F]FDG study in order to assess the method on a different tracer. Figure (6.10) shows a comparison among the different algorithms in terms of image quality at the [^{18}F]FDG peak activity time frame, input function values. On the bottom row the initial 200 s of the input function can be seen on the left, and the remaining part of the IDIF on the right, while on the top the reconstructed images for the peak time frame are shown. Figure (6.11) reports the line profile of the aorta in two different positions (LP1 and LP2) for the [^{18}F]FDG peak images reconstructed with all the investigated methods.

6.4 Discussion

In this chapter, the use of HKEM was proposed for the estimation of the IDIF in the aorta artery of rabbits having undergone [^{18}F]FDG and [^{18}F]NaF PET-MR

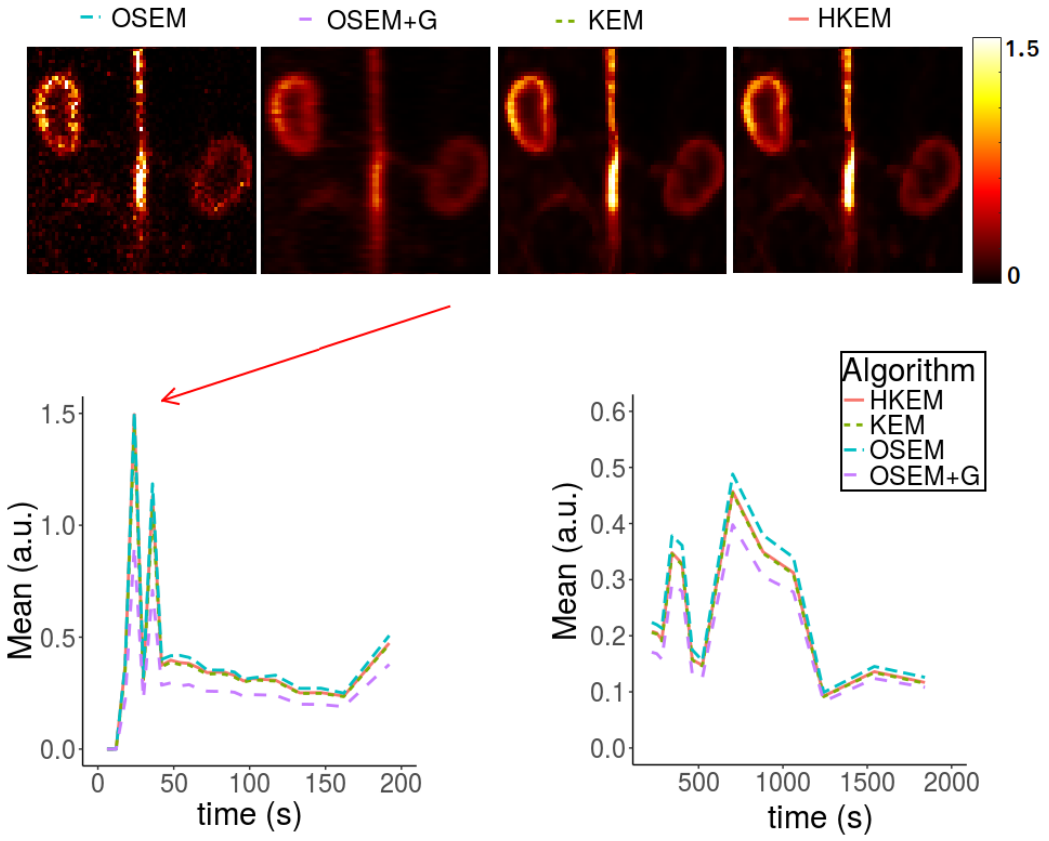

Figure 6.7: Comparison between the [^{18}F]NaF IDIF values over time, after reconstructing with OSEM, OSEM+G, KEM and HKEM methods. On the top row the peak time frame (30-36 s) images are also shown.

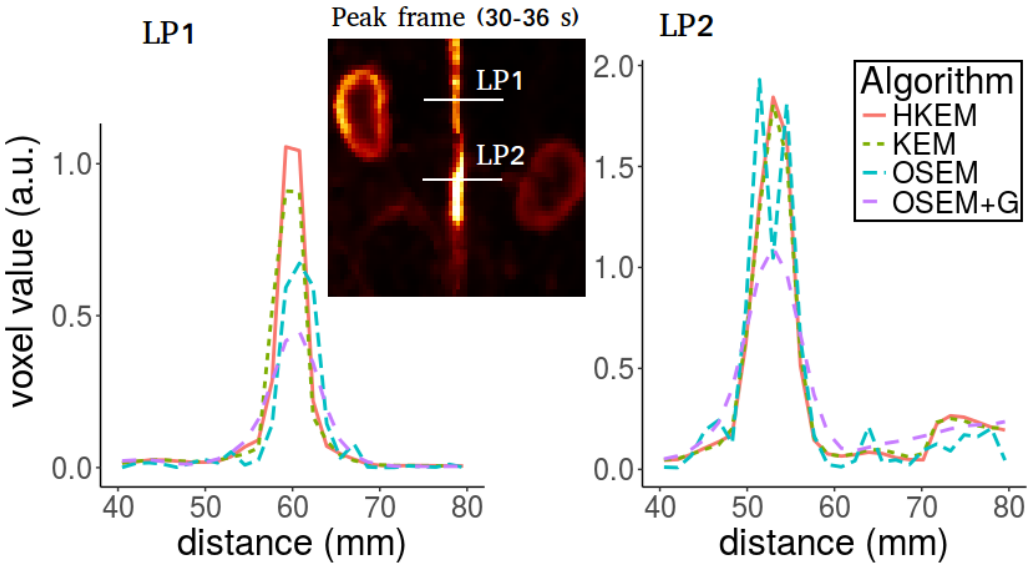

Figure 6.8: Comparison between the line profiles, LP1 and LP2 for the [^{18}F]NaF study, after reconstructing with HKEM, KEM, OSEM and OSEM+G methods.

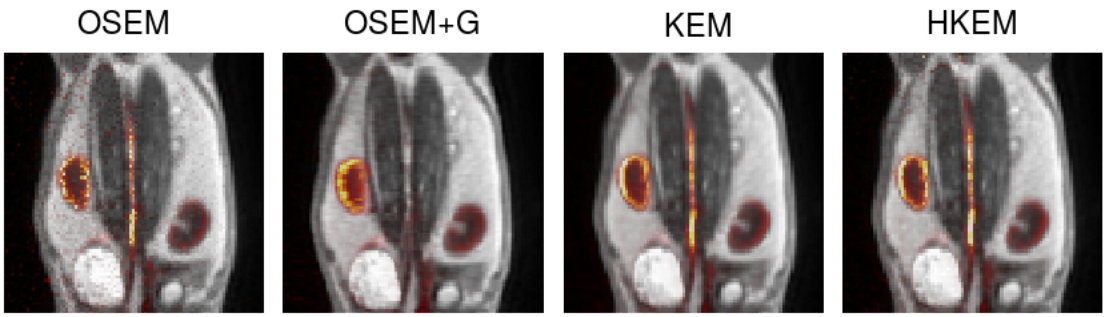

Figure 6.9: Comparison between reconstructed image with OSEM, OSEM+G, KEM, and the proposed HKEM fused with the MR UTE image for the [^{18}F]NaF rabbit data.

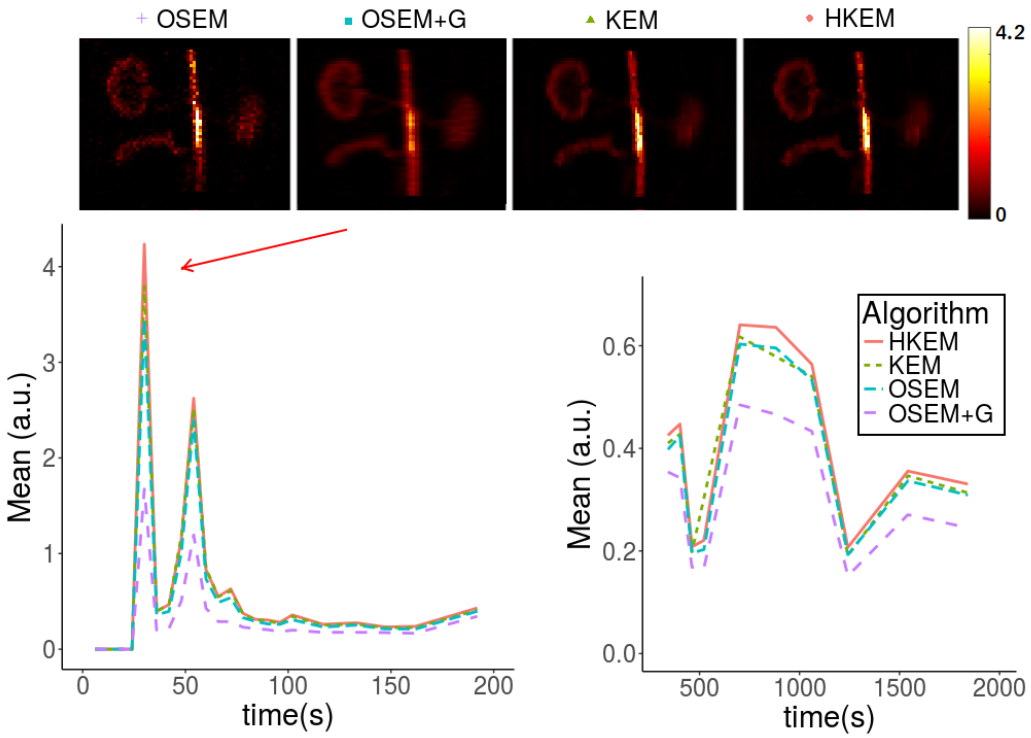

Figure 6.10: Comparison between the IDIF values over time, after reconstructing with OSEM, OSEM+G, KEM and HKEM methods for the [^{18}F]FDG rabbit data. On the top row the peak time frame (30-36 s) images are also shown.

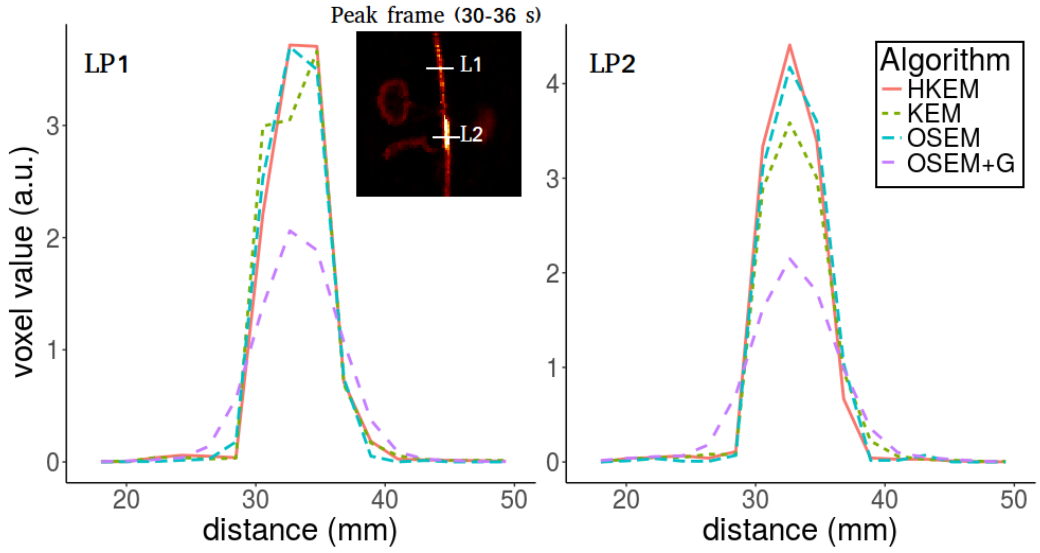

Figure 6.11: Comparison between the line profiles, LP1 and LP2, after reconstructing with OSEM, OSEM+G, KEM and HKEM methods for the [^{18}F]FDG rabbit data.

studies using a clinical PET-MR scanner. The study was driven by the fact that many applications, where dynamic PET is used to extract more accurate and precise kinetic imaging biomarkers, rely on the estimation of the IDIF, which is problematic in preclinical studies due to extensive PVE. As a consequence, it is relevant to propose a method which provides accurate estimates of IDIF. The ROI was chosen to minimise the average RMSE over the frames. In Figure (6.3) we can see that the minimum RMSE is different between different frames, thus the average minimum RMSE was obtained using a 75% threshold. The results in Figure (6.4) show that the proposed reconstruction method and ROI extraction provide accurate results for all the time points. The mean, max and min bias were also calculated over the time frames and the ten noise realisations (Table (6.1)). It was possible to obtain a mean bias of 5 % using the HKEM

with the maximum value being 16.1 %. Note that OSEM also provided accurate results, although the dynamic PET image time frames were quite noisy and thus it becomes challenging to accurately delineate the appropriate aortic input function ROI, which is crucial for the IDIF method. The results suggest that MR information can provide substantial improvement in terms of PVE and noise suppression. Nevertheless, the inclusion of the PET functional information allows better accuracy at the same noise suppression as KEM (see Table (6.1)). Figure (6.5) shows the line profiles at two different points of the carotid for the image corresponding to the peak. Here the better delineation of the aorta can be seen for both the KEM and HKEM MR-guided techniques due to the noise suppression provided in the background tissue regions. It is also important to highlight that the extraction of the ROI from the OSEM image in Figure (6.1) would not be accurate, as the maximum value was very high due to noise. Thus the 75% thresholding would only extract very few voxels, therefore causing up to 100% bias in the OSEM IDIF values despite being associated with high accuracy estimates. Figure (6.6) illustrates the median full IDIF estimate over the 10 realisations, and it is possible to notice the accuracy over time compared to the true values.

The same analysis was applied to two real PET-MR rabbit datasets acquired with the Biograph mMR scanner, using [^{18}F]NaF and [^{18}F]FDG radiotracers. Figure (6.7) shows consistent results for the IDIF. Figure (6.8) presents the line profiles obtained with all methods, showing the good resolution of the aorta when using the HKEM and KEM methods, the noise in the OSEM and the poor quality of the post-filtered OSEM which is highly affected by the PVE. In Figure (6.9) the fused PET-MR image is illustrated for each technique, confirming

the better alignment of the aorta region between the PET and the MR images and the resulting higher PET image resolution and aortic contrast. Moreover, the comparison between the [^{18}F]FDG and [^{18}F]NaF PET-MR studies allowed assessment of the feasibility and performance of HKEM in estimating the aorta IDIF for two of the most commonly employed radiotracers in oncology and cardiology. From the results in Figure (6.10) the benefit of the synergistic PET-MR information encoded in the kernel matrix is visible especially in the IDIF plot. These results are also supported by the line profiles in Figure (6.11) showing a clear definition of the aorta for the proposed method and minimum spill-out of activity from the aorta. It is worth noting that for the real data there are two peaks in the IDIF early time frames, this is probably due to the fact that the injection was not continuous during the scan but there was a sudden stop making the uptake rate drop in that specific time frame.

The input function represents a very crucial data component when estimating kinetic parameters and its accurate estimation can become extremely challenging for small animal imaging due to the very small sizes of the associated aortic vessels. It was demonstrated that, despite the small size of the rabbit aorta, it is feasible and promising to employ the HKEM method for the extraction of an aorta IDIF of improved accuracy and reduced PVE even when using a clinical PET-MR scanner. In addition, the method described to extract the ROI is easy to use and implement as it only involves trivial mathematics between matrices. It is worth mentioning that although this study was performed with PET-MR data it could also work with PET-CT data especially a CT angiography image.

6.5 Conclusion

In this chapter, it was demonstrated that the HKEM method can facilitate the more accurate extraction of the aortic ROI for improved IDIF estimation even when using a human hybrid scanner, compared to conventional OSEM or antomically-guided KEM reconstruction. The findings were obtained with both 10 simulated [^{18}F]NaF PET-MR datasets and 2 real rabbit PET-MR studies, but the methodology can be utilised for most of the available radiotracers and with PET-CT without any major modification. This technique can help enhance the use of dynamic PET in the context of imaging biomarkers with direct pharmacokinetic information.

Chapter 7

General Conclusion and Future Work

7.1 Summary

The main objective of this project was to propose and evaluate a novel PET iterative reconstruction algorithm which incorporates anatomical information from MR and functional information from the PET image itself. In particular, to correct for PVE, reduce bias in low count regions, increase lesion contrast, and allow noise suppression. In the different chapters of the thesis, a number of issues have been discussed and addressed: low-count datasets and the issues related to this with the standard algorithms, PVE and bias reduction with the proposed technique, contrast enhancement for small lesions and noise suppression, effect of PET-MR spatial inconsistencies on image quality and quantification and the accuracy during the calculation of the IDIF for small vessels such as the rabbit aorta.

7.2 Conclusions

Following the overview and the physical and mathematical introduction in Chapters 1 and 2, Chapter 3 showed that using low-count datasets, from short acquisitions, generates bias and significant amounts of noise in the reconstructed images; when regularisation is used to suppress the noise the bias has increased; the contrast and resolution was visibly degraded and small regions were severally blurred. Chapter 4 developed a new iterative algorithm for PET image reconstruction using PET-MR data. The method was inspired by previous studies carried out by other researchers on anatomically-guided techniques. These studies also showed the limitations of such techniques and the HKEM was designed to overcome these problems. This chapter also presents the validation of the algorithm using several datasets. In particular it was shown that by introducing the PET information in the kernel matrix, the detection of small PET unique (about 5 mm diameter) features can be improved compared to standard regularisation algorithms and KEM. The accuracy within the ROIs and the different measurements of contrast also improved compared to standard algorithms. The effect of the parameters σ_p, σ_m, σ_{dp}, σ_{dm}, and N was studied, and it was shown that the same parameter settings, for different datasets, with a comparable number of events give similar results due to the normalisation of the feature vector, which made the method 'independent' of the image scale. Nevertheless, depending on the noise level of the data it can be seen that in some cases the CoV increases iteration after iteration for the HKEM whilst the increase is slower for the KEM. The issues related to PET-MR spatial inconsistencies, due to motion, registration or simply the different information that the two modalities can detect, were investigated in Chapter 5. Different case scenarios were simulated by

introducing a translation along one axis in the MR image. It was shown, using phantom and patient data, that this induced spill-in of activity in cold regions and more moderate spill-out of activity from hot region. In addition, for patient data there was an induced voxel-wise bias up to ±50%. It was also shown that the HKEM can help reducing the induced error especially for the cold regions. An important quantitative outcome from this chapter is represented by the fact that even the worst case scenario for both HKEM and KEM is still better than the result obtained with the application of a 5 mm Gaussian filter after the OSEM reconstruction. Chapter 6 applied the proposed method to improve the accuracy of the IDIF estimation in the context of PET preclinical studies using rabbit data. In addition a dynamic simulation was generated for this purpose. Two rabbit datasets were also used to assess the method and to show consistency with two different radiotracers, [^{18}F]NaF and [^{18}F]FDG. In this chapter, it was demonstrated that, even considering the challenging circumstances in terms of resolution when using small animals, the HKEM can provide overall accurate and precise estimates of the IDIF, with an average bias of 5% and average CoV of about 20%. The extraction of the aorta ROI, which depends on both MR and PET, can provide flexibility in case of spatial inconsistencies between PET and MR. This is because only the maximum values are considered, avoiding low activity values coming from outer tissues. A limitation of the method is the fact that, like OSEM, the noise increases iteration after iteration and especially for low-count datasets. Although this is not as significant as OSEM, it represents a problem in those applications where minimum noise levels are required. Nevertheless, stopping at 2-3 iterations will provide a good trade-off between noise suppression and accuracy. A potential improvement of the thesis, could be

obtained with the use of point spread function (PSF) for additional resolution modelling. However, it has been shown that including PSF can lead to misinterpretation when used in quantification of small sub-centimetre lesions due to the edge artifact that appears near sharp intensity variations (Munk et al. [2017]). In addition, the intent of this thesis was to investigate the improvement provided by the kernel method over standard techniques, and to do so it is easier not to take into account other effects that can be created with the use of PSF. It could also be useful to study whether the effect that PSF has on the OSEM algorithm would be the same when applied to the kernel method.

From a general perspective, the purpose of the thesis was to provide improvement in accuracy, resolution, and image quality by exploiting the synergistic information provided by PET-MR scanners. The HKEM iterative algorithm has been proposed, validated and applied for different case scenarios. It was initially designed for the activity recovery in cases of low-count data, but subsequently extended for different count levels. The proposed technique has been demonstrated to reduce bias, enhance resolution and contrast whilst providing similar noise suppression to the one obtained with a Gaussian filter. It has also been shown that HKEM provides better flexibility in cases of anato-functional inconsistencies compared to the KEM, and finally optimum parameter settings were similar across a range of different datasets for both kernel methods. This thesis, therefore, argues that using synergistic information, via the kernel method, increases the accuracy and precision of the PET clinical diagnostic examination, and, as a consequence, accurate results can be achieved also with low-counts making it possible to conduct future studies with lower injected radioactivity, as well as considering other clinical applications.

7.3 Future Work

A wide range of possible applications could be investigated. The thesis discussed the results obtained with different datasets; however to truly assess whether the proposed method can be translated to clinical routine, clinical studies on specific diseases should be performed. For example, as part of this PhD project a collaboration with the Commonwealth Scientific and Industrial Research Organisation (CSIRO), Brisbane, Australia was established to use the HKEM as the reconstruction algorithm for a clinical study on epilepsy using PET-MR data. Similarly, performing a study on lesion detectability with receiver operating characteristic (ROC) analysis and with a large number of subjects will help to prove the usefulness of the proposed method in the clinical context.

A natural extension of this work could be to study whether consistent results are obtained when a reduced activity is injected in the patient. In the previous chapters low-count circumstances were always obtained by injecting standard activities and extracting frames with shorter time, which is helpful in the case of dynamic data. Allowing injection of a lower radioactivity to the patient would make the diagnostic examination available to more subjects, as higher doses cannot be used for pregnant women and children for example. The same issues related to noise and bias will occur in such situations and the HKEM could play an important role in reduce these issues. The study on IDIF estimation could be extended to the kinetic analysis by estimating the time-activity curve (TAC) of the tissue of interest and use a compartmental model for the estimation of the kinetic rate constants.

Finally, the modularity of the kernel function makes it possible to add multiple information in the model. For instance, with PET-MR scanners it is possible

to acquire many different MR sequences in parallel to the PET acquisition and all these sequences can be used to improve the PET reconstructed image globally. In addition, information from other imaging examination modalities, such as CT, PET with different tracers, or even single photon emission computed tomography (SPECT) images could be taken into account making PET imaging applicable in a wide range of applications. A pilot study was implemented as part of this project, and the method is introduced in Appendix A and preliminary results with simulated data are reported, while the application of the technique with clinical or preclinical data is ongoing research.

Appendix A

Multiplexing KEM (MKEM) Reconstruction for PET-MR

In this appendix an extension of the HKEM method is proposed and preliminary results from a simulation are discussed. The work is presented as submitted and accepted for the IEEE Medical Imaging Conference, Sidney, Australia, 2018. In this work, a version of the kernel method is proposed and investigated which exploits the information contained in multiple MR images, and potentially CT or PET images. To do so, the HKEM was modified such that the kernel matrix is obtained using additional Gaussian terms carrying the features from multiple MR images. The method goes under the name of multiplexing-HKEM (MHKEM) when the PET iterative information is included and 'multiplexing-KEM' (MKEM) when only anatomical images are included. Section A.1 introduces the technique and possible applications that could potentially benefit from it. The methodology of the study, with the ROI analysis is discussed in Section A.2 and the results are shown and discussed in Section A.3.

A.1 Introduction

Since the kernel method was first proposed (Wang and Qi [2015]) in positron emission tomography (PET), it has been successfully used for different applications (Deidda et al. [2018a,b, 2019a,b]; Novosad and Reader [2016]). PET-MR scanners allow the acquisition of many MR sequences, as well as PET data, and different MR sequences, for the same subject, can be exploited to improve image reconstruction. In oncology, for example, metastatic lesions are located in different tissues than the primary lesion. Therefore, lesions in different soft tissues might be detected from different sequences. In this work it is proposed and investigated a kernel method which exploits the information contained in different MR images and potentially CT or PET images. Multiplexed imaging provides diverse data from a single imaging session that can be exploited to offer improved cancer detection and treatment (Kobayashi et al. [2010]; Heinzmann et al. [2017]). Therefore, the proposed method was named 'multiplexing-HKEM' (MHKEM) when the PET iterative information is included and 'multiplexing-KEM' (MKEM) when only anatomical images are included. To do so, the kernel method from Chapter 4 was modified such that the kernel matrix is obtained from extra Gaussian terms carrying the features from the second MR image. Although it is not proposed a specific application here for this algorithm it was hypothesised a case where two MR images are beneficial using a simulated torso dataset. In the kernel method, each voxel value of the image, $\boldsymbol{\lambda}$, can be represented as a linear combination. Thus, λ_j, can be described using the kernel matrix as in equation (4.9) and, the kernelised OSEM for the estimation of voxel j at sub-iteration $n+1$ of the coefficient vector, $\boldsymbol{\alpha}$, can be written as in equation (4.11). The fj^{th} element of the kernel matrix is defined as

$$k_{fj} = k_{m1}(\boldsymbol{v}_f, \boldsymbol{v}_j) \cdot k_p(\boldsymbol{z}_f, \boldsymbol{z}_j), \tag{A.1}$$

where

$$k_{m1}(\boldsymbol{v}_f, \boldsymbol{v}_j) = \exp\left(-\frac{\|\boldsymbol{v}_f - \boldsymbol{v}_j\|^2}{2\sigma_{m2}^2}\right) \exp\left(-\frac{\|\boldsymbol{x}_f - \boldsymbol{x}_j\|^2}{2\sigma_{md}^2}\right), \tag{A.2}$$

is the kernel coming from the MR image and

$$k_p(\boldsymbol{z}_f, \boldsymbol{z}_j) = \exp\left(-\frac{\|\boldsymbol{z}_f - \boldsymbol{z}_j\|^2}{2\sigma_p^2}\right) \exp\left(-\frac{\|\boldsymbol{x}_f - \boldsymbol{x}_j\|^2}{2\sigma_{pd}^2}\right), \tag{A.3}$$

is the part coming from the iterative update. Here the Gaussian kernel functions have been modulated by the distance between voxels in the image space. $\boldsymbol{x}_j$ is the position of the j^{th} voxel, and σ_m, σ_p, σ_{md} and σ_{pd} are scaling parameters for (A.2) and (4.14). In this work, the fj^{th} kernel element in (4.12) was further modified by multiplying Gaussian terms coming from other images:

$$k_{mi}(\boldsymbol{u}_f, \boldsymbol{u}_j) = \exp\left(-\frac{\|\boldsymbol{u}_f - \boldsymbol{u}_j\|^2}{2\sigma_{mi}^2}\right), \tag{A.4}$$

where $\boldsymbol{u}_j$ is the feature vector related to the voxel j, and i is the index of the Gaussian term obtained from the i^{th} image, in this study there are two MR images so i = 1,2.

A.2 Methods and Material

A.2.1 Simulation Study

A realistic simulation study was carried out using data based on Monte Carlo simulation (Jan et al. [2004]) which uses accurate physical modelling as published

by Tsoumpas et al. [2011], using the Philips Gemini TF scanner. The data represents an anthropomorphic torso showing lungs, myocardium, liver, three different lesions between lungs and liver, and a fourth lesion in the myocardium as shown in Figure (A.1(c)). In this study the focus is on the lesion uptake for validation and 4 cases are reproduced: L1 and L2 are lesions which appear only in the PET data; L3 is a lesion appearing both in the PET and the first MR image (MR_1) only, and L4 is the lesion in the myocardium, which is visible both in the PET image and the second MR image (MR_2) only.

A.2.2 Reconstruction Setup

The simulated data were reconstructed with 10 iterations and 23 subsets using HKEM, KEM, MHKEM, MKEM in three possible scenarios:

1) $HKEM_1$, KEM_1 with MR_1;

2) $HKEM_2$, KEM_2 with MR_2;

3) MHKEM, MKEM with MR_1 and MR_2.

For simplicity the aforementioned cases are referred to as $HKEM_1/KEM_1$, $HKEM_2/KEM_2$ and MHKEM/MKEM respectively. The parameters discussed in Section A.1, ν, σ_{m1}, σ_{m2}, σ_p, σ_{md} and σ_{pd} for the kernel were chosen from a preliminary study as the best trade-off between bias and CoV. The size of the neighbourhood, ν, was chosen to be, 3^3 voxels. The voxel size, $4 \times 4 \times 2\,\text{mm}^3$ was chosen based on the scanner characteristics. The algorithms are implemented in the STIR library and all corrections were performed with STIR.

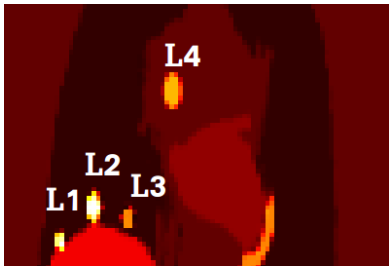

(a)

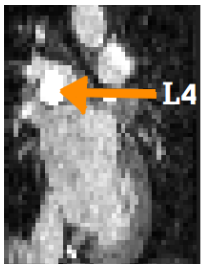

(b)

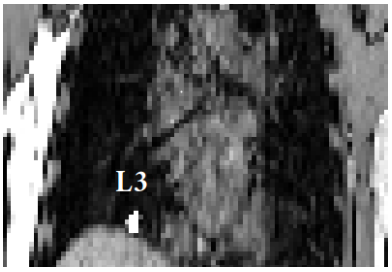

(c)

Figure A.1: Regions of interest chosen for this study. The ROIs (a) in the PET image, the L4 ROI appearing only in image MR_2 (b), and the L3 ROI appearing only in image MR_1 (c).

A.2.3 Images Analysis

The comparison was carried out in terms of bias and CoV, and the ROI analysis was performed using: the lesions L1, L2, L3, and L4. The lesions are shown in Figure (A.1), where L3 appears only in MR_1, L4 only in MR_2, while L1 and L2 represent PET unique features. The figures of merit used for the analysis are defined as:

$$\text{bias} = \frac{t - M_T}{M_T}, \tag{A.5}$$

and

$$\text{CoV} = \frac{\sqrt{\frac{1}{V-1}\sum_{j=1}^{V}(t_j - M)^2}}{M} \times 100, \tag{A.6}$$

where t is the mean values over the selected lesion ROI, M_T is the mean value in the same ROI calculated from the true image, t_j is the j^{th} voxel value within the ROI, M is the mean value of the ROI and V is the number of voxels inside the ROI.

A.3 Results and Discussion

Figure (A.2) shows the ROI comparison in terms of bias and CoV for the 4 ROIs, while Figure (A.3) shows the corresponding reconstructed images for the three scenarios explained in Section A.2.

The aim of this work is to show the feasibility of a kernel method based on two different MR images. The results from Figure (A.2) show that for lesion L1 and L2 the quantification is very similar for all the three different cases, showing that if the MR does not have any information on a lesion MHKEM and MKEM will give similar results as HKEM and KEM respectively. An exception of the latter assertions is represented by the L1 lesion obtained with KEM_2. In fact, the bias is slightly more negative than KEM_1 and MKEM. This might be related to the fact that in MR_2 there is no information about the liver, thus allowing spill out from the lesion and over-smoothing. For lesion L3 the worst case scenario is represented by case 2) for both HKEM and KEM, which is the one where the MR image does not show information about L3. The cases 1) and 3) show equally good results for this lesion. Lesion L4 show bias close to zero for all cases except the KEM_1 as no information about this lesion is included in the kernel. In this case the MKEM and MHKEM show the best trade-off between accuracy and precision. From Figure (A.3) it is possible to notice consistent results on the visual point of view. Lesions L1 and L2 are not affected by the change of

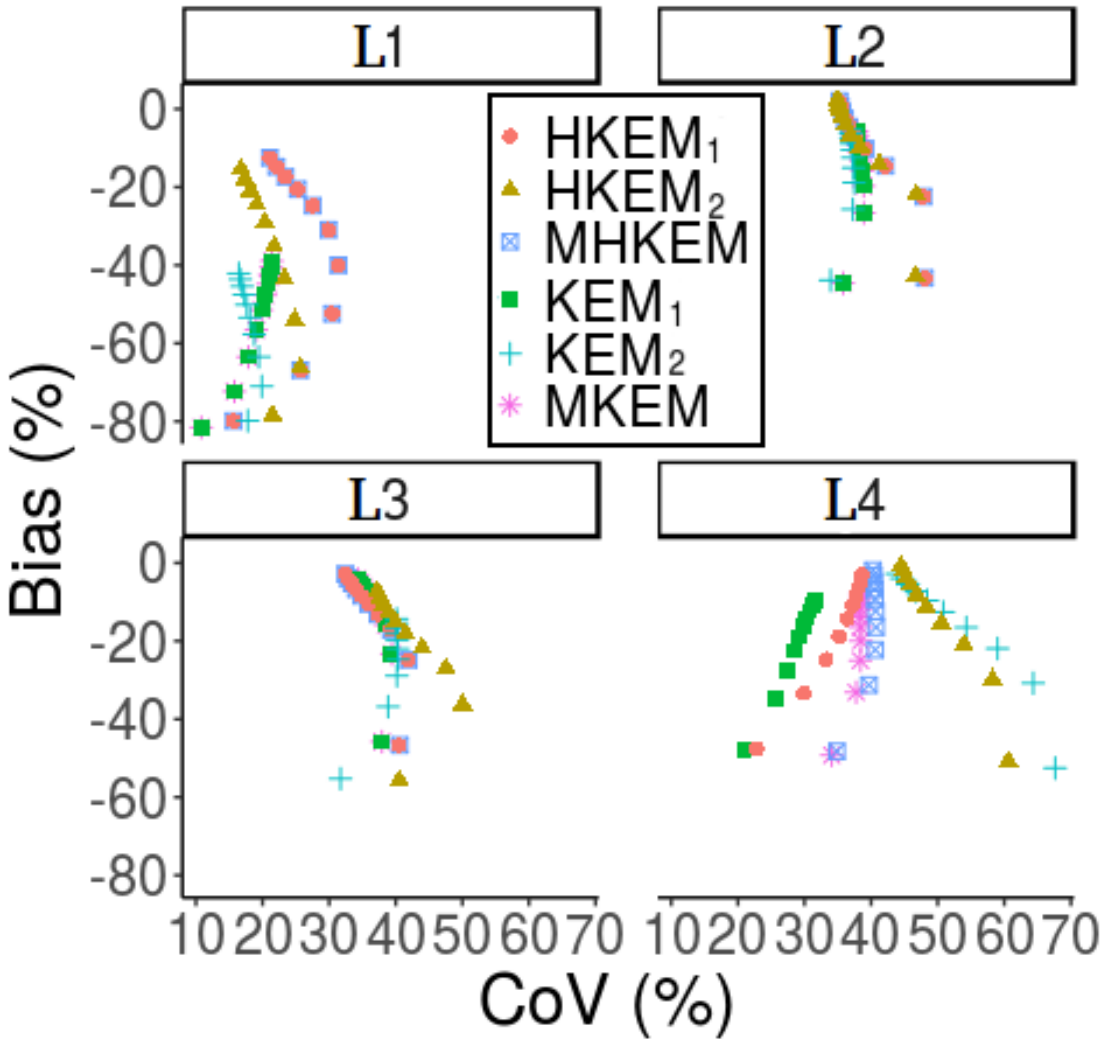

Figure A.2: Comparison between reconstructed image with $HKEM_1$, $HKEM_2$, MHKEM, KEM_1, KEM_2 and MKEM. The bias is plotted against CoV for the four different lesions, L1, L2, L3, L4.

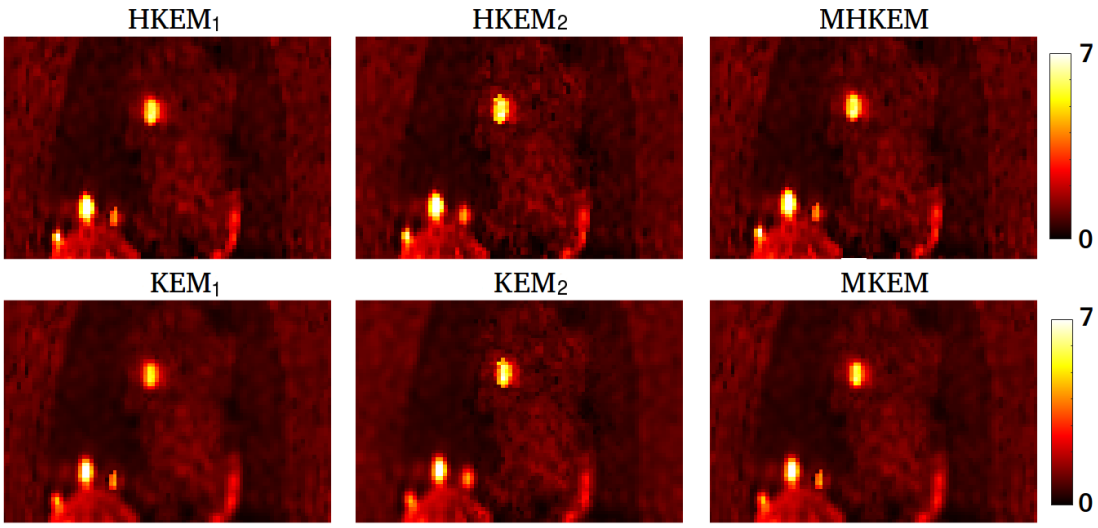

Figure A.3: Reconstructed images with $HKEM_1$, $HKEM_2$, MHKEM in the top row, and KEM_1, KEM_2, MKEM in the bottom.

MR information in the kernel when HKEM is used. In contrast, when KEM is used these lesion express worse resolution and in case 2) it is even more evident. This is the consequence of the absence of the liver information in MR_2. Lesion L3 shows good resolution every time the kernel also contains MR information, while it looks over-smoothed in case 2) where MR_2 only contains features from the heart. Finally, lesion L4 show the best contrast for case 2) and 3).

In summary, the HKEM always shows more accuracy than the KEM due to the ability to exploit functional and anatomical information together. Although the standard HKEM can work well when the focus is on a specific region, it over-smooths other regions that might be of interest. The MHKEM can help providing good quantification, resolution, and noise suppression for areas where the disease might appear.

A.4 Conclusion

In this appendix chapter it was demonstrated with simulated data that potential improvement can be achieved in different areas if multiple images, with different anatomical or functional information provided. Further investigation with real data needs to be carried out to fully demonstrate the applicability of the proposed method.

Appendix B

Implementation of the KEM Reconstruction in STIR

In this appendix it is schematically described the implemented kernel reconstruction in the form of pseudo-code. The written code reproduces the reconstruction algorithm described the equation (4.11). Originally it was implemented as an objective function which could be called by the OSMAPOSL reconstruction algorithm described in Figure (2.7), and two objective functions were created for the LM and for the sinogram reconstruction. Recently, the implementation was adapted to a new reconstruction executable which is derived from OSMAPOSL and it was named KOSMAPOSL. This was done to make the algorithm more flexible and able to use as more as possible all the functionality included in STIR. For instance, there is no need any more to have two different implementation for LM or sinogram because it is possible to choose among all the objective functions available in STIR, including motion compensated image reconstruction.

B.1 Algorithm Architecture

As stated before and shown in Figure (B.1) the kernel method was implemented in the KOSMAPOSLReconstruction class, which inherits the OSMAPOSLReconstruction functionalities but includes the functions for the kernel calculation. In addition, the member function $update\_estimate(TargetT\ \&current\_image\_estimate)$, which perfoms the calculation in OSMAPOSL was overridden by the KOSMAPOSL member function $update\_estimate(TargetT\ \&current\_alpha\_coefficent\_image)$ which takes into account the kernel. The main member functions are described in the following sub-sections.

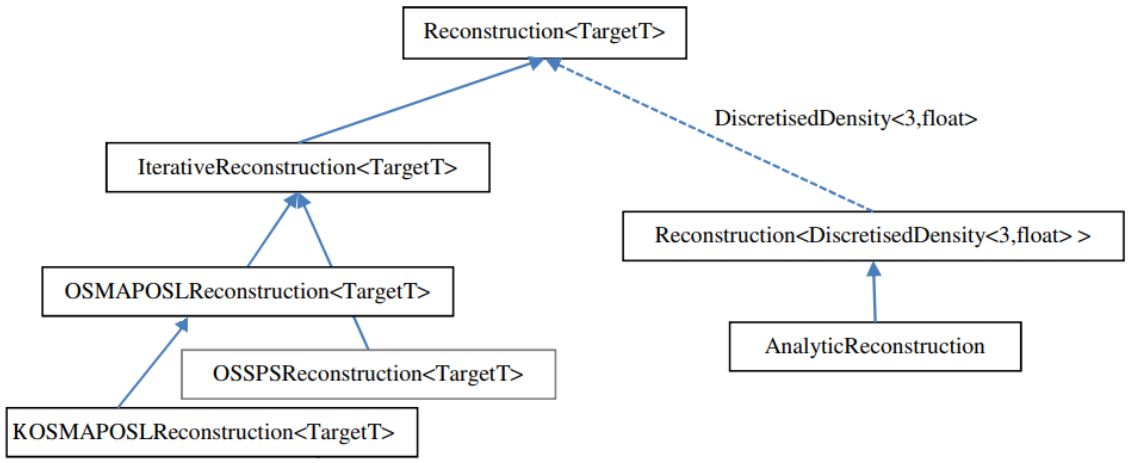

Figure B.1: Class hierarchy for KOSMAPOSL reconstruction algorithms (image modified from Thielemans et al. [2012]).

B.1.1 Calculate Euclidean Distance Between Feature Vectors

This member function extracts the feature vectors for each voxel in the input image and creates a matrix containing the Euclidean distance between feature vectors associated with neighbouring voxels (like in equations (4.13) and (4.14)), and it can also be seen as the norm of the vector obtained from the difference between the two feature vectors.

```
void  calculate_norm_matrix( norm_matrix,
                             number_of_rows,
                             number_of_columns,
                             input_image){

//define an array where the feature vectors will be stored:
f = Array<2,float>(IndexRange2D(0,number_of_rows,
                                0,number_of_columns));

//extract feature vector for each voxel in input_image
for (int z=min_z; z<=max_z; z++){
dimy=max_y-min_y+1;
 for (int y=min_y;y<= max_y;y++){
 dimx=max_x-min_x+1;
  for (int x=min_x;x<= max_x;x++){
//adapt indexes z, y, x to mono-dimensional index l
  l=(z-min_z)*(max_x-min_x +1)*(max_y-min_y +1) +
    (y-min_y)*(max_x-min_x +1) +
    (x-min_x);
```

```
//here f is filled with the feature vectors:
   for (int dz=min_dz;dz<=max_dz;++dz)
   for (int dy=min_dy;dy<=max_dy;++dy)
   for (int dx=min_dx;dx<=max_dx;++dx){
//adapt indexes for the neighbours, dz, dy, dx to mono-
//dimensional index m
   m=(dz)*(max_dx-min_dx +1)*(max_dy-min_dy +1) +
     (dy)*(max_dx-min_dx +1) + (dx);

     int c=m;
     if(m<0){
             c=m + number_of_neighbours ;
            }
     else{c=m;}

   fp[l][c] = (pet[z+dz][y+dy][x+dx]);}}}}

//the norms of the difference between feature vectors related to the
//same neighbourhood are calculated now and stored into norm_matrix

for (int q=0; q<=number_of_rows-1; ++q){
 for (int n=-(number_of_neighbours-1)/2*(!2D);
      n<=(number_of_neighbours-1)/2*(!2D); ++n)
  for (int k=-(number_of_neighbours-1)/2;
       k<=(number_of_neighbours-1)/2; ++k)
   for (int j=-(number_of_neighbours-1)/2;
        j<=(number_of_neighbours-1)/2; ++j)
    for (int i=0; i<=number_of_columns; ++i){

        p=j+k*(cubic_root_of_number_of_neighbours)+
```

```
        n*square((cubic_root_of_number_of_neighbours))+
        (number_of_neighbours-1)/2;

//it checks that the difference is calculated only for neighbouring
// feature vectors and that the voxels in the
// edge have less neighbours to compare;
//dim_x, dim_y, dim_z are dimension of the 3D image along each axis;
//N.B. with number_of_non_zero_elements it is possible to choose
//how many elements of the neighbourhood contribute to the norm.

        if(q mod dimx==0 && (j+k*dimx+n*dimx*dimy)>=(dimx-1)){
        if(j+k*dimx+n*dimx*dimy>=dimx+(num_neighbours-1)/2{
        continue;}

        o=q+j+k*dimx+n*dimx*dimy+1;}
        else{o=q+j+k*dimx+n*dimx*dimy;}

        if(o>=dimf_row-1 || o<0 || i<0||
         i>number_of_non_zero_elements-1 ||
         q>=number_of_rows-1 || q<0){
         continue;}

         normp[0][q][p]+=square(f[q][i]-f[o][i]);}
         }
```

B.1.2 Compute Kernelised Image

With this member function the calculation of the equation (4.9) is performed. However the calculation is not only applied to the kernel coefficients image but

also to the sensitivity image, $\sum_i c_{fi}$:

$$\sum_j k_{fj}^{(n)} \sum_i c_{fi}, \tag{B.1}$$

and to the term obtained from the gradient of the objective function plus the sensitivity:

$$\sum_j k_{fj}^{(n)} \sum_i c_{ij} \frac{1}{\sum_l c_{il} \sum_f k_{fl}^{(n)} \alpha_f^{(n)} + s_i}, \tag{B.2}$$

the function can calculate the kernelised image in two ways according to the number of non zero elements in the feature vector: if $number\_of\_non\_zero\_elements$=1 the $compact\_compute\_kernelised\_image()$ is used while if $number\_of\_non\_zero\_elements$ >1 the $full\_compute\_kernelised\_image()$ is used.

```
void  compute_kernelised_image(output_image,
                               input_image,
                               current_alpha_coefficent_image)
{

if(number_of_non_zero_elements==1){
  compact_compute_kernelised_image(output_image,
                               input_image,
                               current_alpha_coefficent_image);
}
else{
  full_compute_kernelised_image(output_image,
                               input_image,
                               current_alpha_coefficent_image);
                               }
}
```

```
void  full_compute_kernelised_image(output_image,
                                    input_image,
                                    current_alpha_coefficent_image)
{

if(hybrid){
calculate_norm_matrix( pet_norm_matrix,
                               number_of_rows,
                               number_of_columns,
                               current_alpha_coefficent_image);}
//calculate_norm_matrix() is called only once with the anatomical
//image in the post_processing() which is only called at the
//beginning of the iterative process

for (int z=min_z; z<=max_z; z++){
 for (int y=min_y;y<= max_y;y++){
   for (int x=min_x;x<= max_x;x++){
    l=(z-min_z)*(max_x-min_x +1)*(max_y-min_y +1) +
    (y-min_y)*(max_x-min_x +1) +
    (x-min_x);
    for (int dz=min_dz;dz<=max_dz;++dz)
     for (int dy=min_dy;dy<=max_dy;++dy)
      for (int dx=min_dx;dx<=max_dx;++dx){
       m=(dz)*(max_dx-min_dx +1)*(max_dy-min_dy +1) +
     (dy)*(max_dx-min_dx +1) + (dx);

      if(hybrid){
        if(current_alpha_coefficent_image[z][y][x]==0){
        continue;}
        else{
```

```
        kPET = exp(-pet_norm_matrix[0][l][m]/
        square(current_alpha_coefficent_image[z][y][x]*sigma_p)/2)*
        exp(-square(distance[dz][dy][dx])/
        (2*square(sigma_dp)));}
//distance is the Euclidean distance between two voxels



      else{ kPET=1;}


        kanatomical = exp(-a_norm_matrix[0][l][m]/
         square(anatomical_sd*sigma_m)/2)*
         exp(-square(distance[dz][dy][dx])/
         (2*square(sigma_dm)));
//anatomical_sd is the standard deviation calculated over
//all the voxels in the anatomical image

        output_image[z][y][x] += kanatomical*kPET*
                                 input_image[z+dz][y+dy][x+dx];
        normalisation += kanatomical*kPET;}

        output_image[z][y][x] /= normalisation;

        normalisation = 0;}}}}
}
```

When the compact version is called the kernel matrix is not explicitly calculated as the norm becomes the difference between voxel values between neighbours, and these can be directly accessed from the images.

```
void  compact_compute_kernelised_image(output_image,
                                       input_image,
```

```
                                        current_alpha_coefficent_image)
{

for (int z=min_z; z<=max_z; z++){
 for (int y=min_y;y<= max_y;y++){
   for (int x=min_x;x<= max_x;x++){

    for (int dz=min_dz;dz<=max_dz;++dz)
     for (int dy=min_dy;dy<=max_dy;++dy)
      for (int dx=min_dx;dx<=max_dx;++dx){

       if(hybrid){
         if(current_alpha_coefficent_image[z][y][x]==0){
         continue;}
         else{
         pnorm=square{current_alpha_coefficent_image[z][y][x] -
                    current_alpha_coefficent_image[z+dz][y+dy][x+dx]);
         kPET = exp(-pnorm/
         square(current_alpha_coefficent_image[z][y][x]*sigma_p)/2)*
         exp(-square(distance[dz][dy][dx])/
         (2*square(sigma_dp())));}

       else{ kPET=1;}
       anorm=square{anatomical_image[z][y][x] -
                    anatomical_image[z+dz][y+dy][x+dx]);
        kanatomical = exp(-anorm/
         square(anatomical_sd*sigma_m)/2)*
         exp(-square(distance[dz][dy][dx])/
         (2*square(sigma_dm())));
```

```
        output_image[z][y][x] += kanatomical*kPET*
                                 input_image[z+dz][y+dy][x+dx];
        normalisation += kanatomical*kPET;}

        output_image[z][y][x] /= normalisation;

        normalisation=0;}}}}
}
```

B.1.3 Update Estimate

The *update_estimate*() which is called by the IterativeReconstruction class iteratively update the reconstructed image. The sensitivity image and the gradient are estimated from the objective function class, and the kernel is applied in *update_estimate*(). Subsequently, the division between (B.2) and (B.1) is calculated and the result is multiplied by $\alpha^{(n)}$ to obtain $\alpha^{(n+1)}$. Finally, the kernel is applied to $\alpha^{(n+1)}$ to obtain the PET image, $\lambda^{(n+1)}$.

```
update_estimate(current_alpha_coefficent_image)
{

compute_kernelised_image (current_PET_update_image,
                          current_alpha_coefficent_image,
                          current_alpha_coefficent_image);

 ObjectiveFunction::
 compute_sub_gradient_without_penalty_plus_sensitivity (
        multiplicative_update_image,
    current_PET_update_image,
    subset_num);
```

```
//apply kernel to the multiplicative update
compute_kernelised_image(kmultiplicative_update_image,
                         multiplicative_update_image,
                         current_alpha_coefficent_image);

// divide by subset sensitivity
 sensitivity = ObjectiveFunction::
 get_subsedingt_sensitivity(subset_num);

 compute_kernelised_image (ksensitivity,
                           sensitivity,
                           current_alpha_coefficent_image);

 kmultiplicative_update_image=divide(kmultiplicative_update_image,
        ksensitivity);

 current_alpha_coefficent_image=
     multiply(current_alpha_coefficent_image,
              kmultiplicative_update_image);

//Write the PET image estimate:
 compute_kernelised_image (current_PET_image,
                           current_alpha_coefficent_image,
                           current_alpha_coefficent_image);

subiteration_counter++;
if(subiteration_counter mod save_interval == 0){
write_to_file(current_PET_image_filename,current_PET_image);}}
```

B.1.4 Parsing

The parameters that are defined by the user, such as kernel parameters, voxel size, objective function and so on, are set in a text file, also called parameter file. An example of such file is shown below:

```
KOSMAPOSLParameters :=
; Example file for using [Hybrid] Kernelized Expectation Maximisation (HKEM or KEM).
; See documentation of KOSMAPOSLreconstruction
; for more info.
;the following disable the alpha coefficient output:
disable output :=1
; here we have the possibility to choose the parameters which define the kernel
; matrix and the name of the anatomical image. the following are the defaults values:
; 1 (default): use hybrid kernel (prior from MR and PET estimate)
; OR
; 0 kernel is MR-only
hybrid:=1
; Gaussian scaling parameter for the anatomical prior (units of image intensity)
; It controls the edge preservation from the anatomical image, the bigger the stronger
; default: 1
sigma m:= 1
; Gaussian scaling parameter for the PET estimate (units of PET image intensity)
; It controls the edge preservation from the functional image, the bigger the stronger
; default: 1
sigma p:=1
; NB: sigma dm and sigma dp should be the same
; Spatial Gaussian scaling parameter for the anatomical prior (mm)
; default: 1 (usual range 1-5)
sigma dm:=5
; Spatial Gaussian scaling parameter for the PET prior (mm)
; default: 1 (usual range 1-5)
sigma dp:=5
; Number of neigbouring voxels to compare: (num neighbours X num neighbours X num
neighbours)
; default: 3
number of neighbours:= 3
; Number of non-zero elements in the feature vectors
```

; default: 1
number of non-zero feature elements:=1
; this is the file name of the anatomical image
anatomical image filename:= MRbrain.hv
; the following should be 1 if you want to reconstruct 2D data
only 2D:=1
; the following is the output prefix of the PET reconstructed image
kernelised output filename prefix :=KOSMAPOSL
objective function type:= PoissonLogLikelihoodWithLinearModelForMeanAndProjData
PoissonLogLikelihoodWithLinearModelForMeanAndProjData Parameters:=
input file := myprompts.hs
; Daniel: here we have the possibility to choose the parameters which define the kernel matrix and the name of the MR image.
projector pair type := Matrix
Projector Pair Using Matrix Parameters :=
Matrix type := Ray Tracing
Ray tracing matrix parameters :=
number of rays in tangential direction to trace for each bin := 10
do symmetry 90degrees min phi := 1
do symmetry 180degrees min phi:= 1
do symmetry swap s:= 1
do symmetry swap segment:= 1
do symmetry shift z:= 1
End Ray tracing matrix parameters :=
End Projector Pair Using Matrix Parameters :=
; additive projection data to handle randoms etc
additive sinogram := additive.hs
; norm and acf
Bin Normalisation type := From ProjData
Bin Normalisation From ProjData :=
normalisation projdata filename:= multfactors.hs
End Bin Normalisation From ProjData:=
; if the next parameters are enabled,
; the sensitivity will be computed and saved
; use ; we do this here for illustration, but also for re-use later on (to save some time)
; CAREFUL: use correct number of subsets in name to avoid confusion
subset sensitivity filenames:= sens
recompute sensitivity := 1
xy output image size (in pixels) := -1
end PoissonLogLikelihoodWithLinearModelForMeanAndProjData Parameters:=

```
; if you want to continue from a particular image
; initial estimate:= reconML.hv
; Number of subsets should usually be a divisor of num views/8
; the following is an example for the Siemens mMR
number of subsets:= 21
number of subiterations:= 210
save estimates at subiteration intervals:= 21
END KOSMAPOSLParameters:=
```

The KOSMAPOSLReconstruction and the classes used for the reconstruction parse this file in order to assign these values to the appropriate class members. The member function used for this purpose is called *initialise_keymap*(). An example for the overriden function in KOSMAPOSLReconstruction is shown below:

```
void initialise_keymap()
{
parent::initialise_keymap();

parser.add_start_key("KOSMAPOSLParameters");
parser.add_stop_key("End KOSMAPOSLParameters");

parser.add_key("anatomical image filename",
               anatomical_image_filename);

parser.add_key("number of neighbours",num_neighbours);
parser.add_key("number of non-zero feature elements",
               num_non_zero_feat);

parser.add_key("sigma_m",sigma_m);
parser.add_key("sigma_p",sigma_p);
```

```
parser.add_key("sigma_dp",sigma_dp);
parser.add_key("sigma_dm",sigma_dm);
parser.add_key("only_2D",2D);
parser.add_key("hybrid",hybrid);
parser.add_key("kernelised_output_filename_prefix",
                kernelised_output_filename_prefix);
}
```

Appendix C

Description of the Demonstrative Code for the Rabbit Simulation

The last appendix chapter shows the README file from the demonstrative code created for the simulation in Chapter 6 and published in Deidda [2018]. The file describes all the steps from the simulation to the extraction of the ROI.

NaF Rabbit image-derived input function with hybrid kernelised expectation maximisation.

If you use this code or part of it please refer to its DOI.

Author Daniel Deidda, University of Leeds
email: D.Deidda@leeds.ac.uk, danieldeidda@gmail.com

This code creates simulated realistic PET-MR rabbit data using the NaF tracer and the Biograph Siemens mMR.
The rabbit data is simulated using a UTE MR image to segment tissues and organs . The data is then reconstructed using the hybrid
kernelised expectation maximisation (HKEM) proposed by Deidda et al, (“Hybrid PET-MR list-mode kernelized expectation maximization reconstruction for quantitative PET images of the carotid arteries,”
NSS/MIC/RTSD, Atlanta, Georgia, 2017). In this script the sinogram based HKEM is used.

After the reconstruction, the HKEM image is used together with the MR image to extract the aorta region of interest (ROI) that
can be used for the estimation of the image derived input function (IDIF).

The main script is "run_main.sh", this will call other different scripts and STIR utilities (https://github.com/UCL/STIR).
If you are willing to create your personalised simulation you can open the "run_main.sh" and the other scripts to change the
variables according to what you need. For example, you can change the number of frames, the span, the number of iterations,
the tissues that you want in your simulation and so on.

Looking at the main script:

I) the first three steps will call "create_*single*_tissue_*frames.sh*", "*create*_simulated_*image.sh*" *and* "*time*_rescale_frames.sh",
once these are completed you will have 45 simulated images in the folder ../results/ and they are called
simulated_*frames*_f(frame).hv/.v, each image correspond to one time frame.

II) run "run_*simulated*_projdata.sh": this will create your PET raw data (ex: noisyprompts_*s11*_pn1_f5.hs /.s,
multfactors_s11_pn1_f5.hs /.sh and./scatter_s11_pn1_f1/ additive_sino_s11_pn1_f5.hs)

- If you look at the scripts you will see variables like pn (for the seed of the poisson noise), span
(for the axial compression of the data) and frame (the time frame number);
- the data is only simulated for one frame (the number 5, which correspond to the time activity peak);
- you can choose as many noise realisations as you want, in this example is 1, but you can choose by modifying the script;
- span is 11 in this example to make the code running faster;
- once this script has successfully finished to run you will have all your sinograms and you are ready to reconstruct your
PET images.

III) "run_hkem.sh" start the reconstruction of your simulated data using the HKEM. This will reconstruct 3 full iterations with
21 ordered subsets. You can modify the parameter file kOSEM.par to choose your own settings. Note that the reconstructed
image is named as follows:
6__H1_N3_M1_P1D3D3ks_rec_s1_pn1_f5_63_k.v/.hv. If you see an image with the same name but without the final "_k", that is
the kernel coefficient image, it should not be used for the analysis the only image you are interested in are those ending
with "_k".

IV) "extract_*aorta*_ROI.sh" will extract the aorta ROI that you can use for the accurate estimate of the IDIF.

N.B. If you have your own data to test you can modify the scripts accordingly by providing the sinogram file names and the MR image file
name in step III). To extract the ROI you should provide the extrated aorta from your MR image because in step IV) it will be used as a
mask to extract the aorta from the PET image.

Bibliography

S. Ahn, S. G. Ross, E. Asma, J. Miao, X. Jin, L. Cheng, S. D. Wollenweber, and R. M. Manjeshwar. Quantitative comparison of OSEM and penalized likelihood image reconstruction using relative difference penalties for clinical PET. *Physics in Medicine and Biology*, 60:5733–5751, 2015.

M. Alenezi, M. Bentourkia, F. A. A. Slimani, and A. Khalil. Segmentation and kinetic modeling of human arteries in PET/CT imaging. In *IEEE Nuclear Science Symposium and Medical Imaging Conference Record*, pages 1–3, 2016.

S. Alenius and U. Ruotsalainen. Bayesian image reconstruction for emission tomography based on median root prior. *European Journal of Nuclear Medicine*, 24(3):258–265, 1997.

S. Alenius and U. Ruotsalainen. Generalization of median root prior reconstruction. *IEEE Transactions on Medical Imaging*, 21(11):1413–1420, 2002.

S. Alenius, U. Ruotsalainen, and J. Astola. Using local median as the location of the prior distribution in iterative emission tomography image reconstruction. *IEEE Transactions on Nuclear Science*, 45(6):3097–3104, 1998.

N. M. Alpert, D. A. Chesler, J. A. Correia, R. H. Ackerman, J. Y. Chang, S. Finklestein, S. M. Davis, G. L. Brownell, and J. M. Taveras. Estimation of the

local statistical noise in emission computed tomography. *IEEE Transactions on Medical Imaging*, 1(2):142–146, 1982.

E. Asma, S. Ahn, S. G. Ross, . Chen, and R. M. Manjeshwar. Accurate and consistent lesion quantitation with clinically acceptable penalized likelihood images. In *IEEE Nuclear Science Symposium and Medical Imaging Conference Record Conference*, pages 4062–4066. IEEE, 2012.

K. Baete, J. Nuyts, K. Van Laere, W. Van Paesschen, S. Ceyssens, L. De Ceuninck, O. Gheysens, A. Kelles, J. Van den Eynden, P. Suetens, and P. Dupon. Evaluation of anatomy based reconstruction for partial volume correction in brain FDG-PET. *Neuroimage*, 23(1):305–317, 2004.

B. Bai, Q. Li, and R. M. Leahy. Magnetic resonance-guided positron emission tomography image reconstruction. In *Seminars in Nuclear Medicine*, volume 43, pages 30–44. Elsevier, 2013.

H. H. Barrett, D. W. Wilson, and B. M. Tsui. Noise properties of the EM algorithm. i. Theory. *Physics in Medicine and Biology*, 39:833–846, 1994.

H. H. Barrett, T. White, and L. C. Parra. List-mode likelihood. *Journal of the Optical Society of America. A, Optics, Image Science, and Vision*, 14(11): 2914–2923, 1997.

M. Bentourkia. Determination of the input function at the entry of the tissue of interest and its impact on PET kinetic modeling parameters. *Molecular Imaging and Biology*, 17(6):748–756, 2015.

O. Bertolli, M. Cecchetti, N. Camarlinghi, A. Eleftheriou, N. Belcari, and C. Tsoumpas. Iterative reconstruction incorporating positron range correction

within STIR framework. In *Journal of Nuclear Medicine Molecular Imaging Physics*, volume 1, pages 323–330. Springer, 2014.

V. Bettinardi, E. Pagani, M. C. Gilardi, S. Alenius, K. Thielemans, M. Teras, and F. Fazio. Implementation and evaluation of a 3D one-step late reconstruction algorithm for 3D positron emission tomography brain studies using median root prior. *European Journal of Nuclear Medicine Molecular Imaging*, 29:7–18, 2002.

T. Beyer, D. W. Townsend, T. Brun, P. E Kinahan, M. Charron, R. Roddy, J. Jerin, J. Young, L. Byars, and R. Nutt. A combined PET/CT scanner for clinical oncology. *Journal of Nuclear Medicine*, 41(8):1369–1379, 2000.

I. Bezrukov, F. Mantlik, H. Schmidt, B. Schölkopf, and B. J. Pichler. MR-based PET attenuation correction for PET/MR imaging. In *Seminars in Nuclear Medicine*, volume 43, pages 45–59. Elsevier, 2013.

N. Bissantz, B. A. Mair, and A. Munk. A multi-scale stopping criterion for mlem reconstructions in PET. In *IEEE Nuclear Science Symposium and Medical Imaging Conference Record*, volume 6, pages 3376–3379. IEEE, 2006.

J. Bland, A. Mehranian, M. A. Belzunce, S. Ellis, C. J. McGinnity, A. Hammers, and A. J. Reader. MR-guided kernel EM reconstruction for reduced dose PET imaging. *IEEE Translation of Radiation and Plasma in Medical Science*, pages 235–243, 2017.

J. Bland, M. A. Belzunce, S. Ellis, C. J. McGinnity, A. Hammers, and A. J. Reader. Spatially-compact MR-Guided kernel EM for PET image reconstruc-

tion. *IEEE Transactions on Radiation and Plasma Medical Sciences*, pages 470 – 482, 5 2018.

J. E. Bowsher, V. E. Johnson, T. G. Turkington, R. J. Jaszczak, C. E. Floyd, and R. E. Coleman. Bayesian reconstruction and use of anatomical a priori information for emission tomography. *IEEE Transactions on Medical Imaging*, 15(5):673–686, 1996.

D. Brasse, P. E. Kinahan, C. Lartizien, C. Comtat, M. Casey, and C. Michel. Correction methods for random coincidences in fully 3D whole-body PET: impact on data and image quality. *Journal of Nuclear Medicine*, 46:859–867, 2005.

I. Britvitch, I. Johnson, D. Renker, A. Stoykov, and E. Lorenz. Characterisation of Geiger-mode avalanche photodiodes for medical imaging applications. *Nuclear Instruments and Methods in Physics Research Section A: Accelerators, Spectrometers, Detectors and Associated Equipment*, 571:308 – 311, 2007.

C. Byrne. Likelihood maximization for list-mode emission tomographic image reconstruction. *IEEE Transactions on Medical Imaging*, 20(10):1084–1092, 2001.

C. L. Byrne. Accelerating the EMML algorithm and related iterative algorithms by rescaled block-iterative methods. *IEEE Transactions on Image Processing*, 7:100–109, 1998.

C. Catana, Y. Wu, M. S. Judenhofer, J. Qi, B. J. Pichler, and S. R. Cherry. Simultaneous acquisition of multislice PET and MR images: initial results

with a MR-compatible PET scanner. *Journal of Nuclear Medicine*, 47(12): 1968, 2006.

C. Catana, H. H. Quick, and H. Zaidi. Current commercial techniques for MRI-guided attenuation correction are insufficient and will limit the wider acceptance of PET/MRI technology in the clinic. *Medical Physics*, 45:4007–4010, 2018.

S. R. Cherry, T. Jones, J. S. Karp, J. Qi, W. W. Moses, and R. D. Badawi. Total-body PET: Maximizing sensitivity to create new opportunities for clinical research and patient care. *Journal of Nuclear Medicine*, 59:3–12, 2018.

G. J. R. Cook, G. M. Blake, P. K. Marsden, B. Cronin, and I. Fogelman. Quantification of skeletal kinetic indices in Paget's disease using dynamic 18F-Fluoride positron emission tomography. *Journal of Bone and Mineral Research*, 17(5): 854–859, 2002.

D. Deidda. Rabbit image-derived input function with hybrid kernelised expectation maximisation. `https://doi.org/10.24433/CO.bde84e0c-4c73-47fa-8ba5-81fb8bd2af77`, June 2018.

D. Deidda, N. Efthimiou, R. Manber, K. Thielemans, P. Markiewicz, R. G. Aykroyd, and C. Tsoumpas. Comparative evaluation of image reconstruction methods for the siemens PET-MR scanner using the STIR library. In *IEEE Nuclear Science Symposium and Medical Imaging Conference Record*, pages 1–6, 2016.

D. Deidda, N. Karakatsanis, P. M. Robson, N. Efthimiou, Z. A. Fayad, R. G. Aykroyd, and C. Tsoumpas. Hybrid PET-MR list-mode kernelized expectation

maximization reconstruction for quantitative PET images of the carotid arteries. In *IEEE Nuclear Science Symposium and Medical Imaging Conference Record*, pages 1–7, 2017.

D. Deidda, R. G. Aykroyd, and C. Tsoumpas. Assessment of maximum a posteriori image estimation algorithms for reduced acquisition time medical positron emission tomography data. In *Recent Studies on Risk Analysis and Statistical Modeling*, pages 3–16. Springer, 2018a.

D Deidda, N Karakatsanis, P M Robson, N Efthimiou, Z A Fayad, R G Aykroyd, and C. Tsoumpas. Effect of PET-MR inconsistency in the kernel image reconstruction method. *IEEE Transactions on Radiation and Plasma Medical Sciences*, 2018b.

D. Deidda, N. Karakatsanis, P. M. Robson, Y. Tsai, N. Efthimiou, Z. A., K. Thielemans, Fayad, R. G. Aykroyd, and C. Tsoumpas. Hybrid PET-MR list-mode kernelized expectation maximization reconstruction. *Inverse Problems*, 2019a.

D. Deidda, N. A. Karakatsanis, C. Calcagno, P. M. Robson, M. Senders, W. J. M. Mulder, Z. A. Fayad, R. G. Aykroyd, and C. Tsoumpas. Hybrid PET-MR kernelised expectation maximisation reconstruction for improved image- derived estimation of the input function from the aorta of rabbits. *Contrast Media and Molecular Imaging*, pages 1–12, 2019b.

G. Delso and J. Nuyts. PET/MRI: Attenuation correction. In *PET/MRI in Oncology*, pages 53–75. Springer, 2018.

G. Delso, S. Fürst, B. Jakoby, R. Ladebeck, C. Ganter, S. G. Nekolla,

M. Schwaiger, and S. I. Ziegler. Performance measurements of the siemens mMR integrated whole-body PET/MR scanner. *Journal of Nuclear Medicine*, 52:1914–1922, 2011.

J. A. Disselhorst, I. Bezrukov, A. Kolb, C. Parl, and B. J. Pichler. Principles of PET/MR imaging. *Journal of Nuclear Medicine*, 55(Supplement 2):2S–10S, 2014.

M. J. Ehrhardt, K. Thielemans, L. Pizarro, D. Atkinson, S. Ourselin, B. F. Hutton, and S. R. Arridge. Joint reconstruction of PET-MR by exploiting structural similarity. *Inverse Problems*, 31(1):1–23, 2014.

M. J. Ehrhardt, P. Markiewicz, M. Liljeroth, A. Barnes, V. Kolehmainen, J. S. Duncan, L. Pizarro, D. Atkinson, B. F. Hutton, S. Ourselin, K. Thielemans, and S. R. Arridge. PET reconstruction with an anatomical MRI prior using parallel level sets. *IEEE Transactions on Medical Imaging*, 35(9):2189–2199, 2016.

M. Eldib, J. Bini, P. M. Robson, C. Calcagno, D. D. Faul, C. Tsoumpas, and Z. A. Fayad. Markerless attenuation correction for carotid MRI surface receiver coils in combined PET/MR imaging. *Physics in Medicine and Biology*, 60(12): 4705–4717, 2015.

S. Ellis and A. J. Reader. Kernelised EM image reconstruction for dual-dataset PET studies. *IEEE Nuclear Science Symposium and Medical Imaging Conference Record*, pages 1–3, 2016.

F. H. Fahey. Data acquisition in PET imaging. *Journal of Nuclear Medicine Technology*, 30:39–49, 2002.

J. A. Fessler. Statistical image reconstruction methods for transmission tomography. *Handbook of Medical Imaging*, 2:1–70, 2000.

E. C. Frey, J. L. Humm, and M. Ljungberg. Accuracy and precision of radioactivity quantification in nuclear medicine images. In *Seminars in Nuclear Medicine*, volume 42, pages 208–218. Elsevier, 2012.

M. L. Frost, A. E. Moore, M. Siddique, G. M. Blake, D. Laurent, B. Borah, U. Schramm, M. Valentin, T. C. Pellas, P. K. Marsden, P. J. Schleyer, and I. Fogelman. 18F-Fluoride PET as a noninvasive imaging biomarker for determining treatment efficacy of bone active agents at the hip: A prospective, randomized, controlled clinical study. *Journal of Bone and Mineral Research*, 28(6):1337–1347, 2013.

E. K. Fung and R. E. Carson. Cerebral blood flow with [15O] water PET studies using an image-derived input function and MR-defined carotid centerlines. *Physics in Medicine and Biology*, 58:1903, 2013.

A. Gaitanis, G. Kontaxakis, G. Spyrou, G. Panayiotakis, and G. Tzanakos. PET image reconstruction: A stopping rule for the MLEM algorithm based on properties of the updating coefficients. *Computerized Medical Imaging and Graphics*, 34(2):131–141, 2010.

G. Germano, B. C. Chen, S. C. Huang, S. S. Gambhir, E. J. Hoffman, and M. E. Phelps. Use of the abdominal aorta for arterial input function determination in hepatic and renal PET studies. *Journal of Nuclear Medicine: Official Publication, Society of Nuclear Medicine*, 33(4):613–620, 1992.

K. Gong, J. Cheng-Liao, G. Wang, K. T. Chen, C. Catana, and J. Qi. Direct

patlak reconstruction from dynamic PET data using the kernel method with MRI information based on structural similarity. *IEEE Transactions on Medical Imaging*, 37(4):955–965, 2018a.

K. Gong, J. Guan, K. Kim, X. Zhang, G. E. Fakhri, J. Qi, and Q. Li. Iterative PET image reconstruction using convolutional neural network representation. *IEEE Transactions on Medical Imaging*, 2018b.

P. J. Green. Bayesian reconstructions from emission tomography data using a modified EM algorithm. *IEEE Transactions on Medical Imaging*, 9:84–93, 1990a.

P. J. Green. On use of the EM for penalized likelihood estimation. *Journal of the Royal Statistical Society. Series B (Methodological)*, 52(3):443–452, 1990b.

B. S. Halpern, M. Dahlbom, A. Quon, C. Schiepers, C. Waldherr, Silverman D. H., Ratib O., and Czernin J. Impact of patient weight and emission scan duration on PET/CT image quality and lesion detectability. *Journal of Nuclear Medicine*, 45(5):797, 2004.

J. Hamill and T. Bruckbauer. Iterative reconstruction methods for high-throughput PET tomographs. *Physics in Medicine and Biology*, 47(15):2627, 2002.

B. E. Hammer, N. L. Christensen, and B. G. Heil. Use of a magnetic field to increase the spatial resolution of positron emission tomography. *Medical Physics*, 21:1917–1920, 1994.

P. C. Hansen. The l-curve and its use in the numerical treatment of inverse problems. 1999.

K. Heinzmann, L. M. Carter, J. S. Lewis, and E. O. Aboagye. Multiplexed imaging for diagnosis and therapy. *Nature Biomedical Engineering*, 1(9):697–713, 2017.

E. J. Hoffman, P. D. Cutler, W. M. Digby, and J. C. Mazziotta. 3-D phantom to simulate cerebral blood flow and metabolic images for PET. *IEEE Transactions on Nuclear Science*, 37:616–620, 1990.

T. Hoffman, B. Scholkopf, and A. J. Smola. Kernel methods in machine learning. *Annals of Statistics*, 36:1171–1220, 2008.

M. Hofmann, F. Steinke, V. Scheel, G. Charpiat, J. Farquhar, P. Aschoff, M. Brady, B. Schölkopf, and Bernd J. Pichler. MRI-based attenuation correction for PET/MRI: a novel approach combining pattern recognition and atlas registration. *Journal of Nuclear Medicine*, 49(11):1875–1883, 2008.

M. Hofmann, I. Bezrukov, F. Mantlik, P. Aschoff, F. Steinke, T. Beyer, B. J. Pichler, and B. Schölkopf. MRI-based attenuation correction for whole-body PET/MRI: quantitative evaluation of segmentation-and atlas-based methods. *Journal of Nuclear Medicine*, 52:1392–1399, 2011.

D. Hogg, K. Thielemans, T. Spinks, and N. Spyrou. Maximum-likelihood estimation of normalisation factors for PET. In *IEEE Nuclear Science Symposium and Medical Imaging Conference Record*, volume 4, pages 2065–2069, 2001.

H. M. Hudson and R. S. Larkin. Accelerated image reconstruction using ordered subsets of projection data. *IEEE Transactions on Medical Imaging*, 13:601–609, 1994.

R. H. Huesman, G. J. Klein, W. W. Moses, J. Qi, B. W. Reutter, and P. R. Virador. List-mode maximum-likelihood reconstruction applied to positron emission mammography (PEM) with irregular sampling. *IEEE Transactions on Medical Imaging*, 19(5):532–537, 2000.

W. Hutchcroft, G. B. Wang, and J. Qi. Anatomical-image aided PET reconstruction by the kernel method. *Journal of Nuclear Medicine*, 55:suppl 1, abstract 44, 2014.

W. Hutchcroft, G. Wang, K. T. Chen, C. Catana, and J. Qi. Anatomically-aided PET reconstruction using the kernel method. *Physics in Medicine and Biology*, 61(18):6668, 2016.

B. F. Hutton, I. Buvat, and F. J. Beekman. Review and current status of SPECT scatter correction. *Physics in Medicine and Biology*, 56:R85–R112, 2011.

M. Jacobson, R. Levkovitz, A. Ben-Tal, K. Thielemans, T. Spinks, D. Belluzzo, E. Pagani, V. Bettinardi, M. C. Gilardi, A. Zverovich, and G. Mitra. Enhanced 3D PET OSEM reconstruction using inter-update Metz filtering. *Physics in Medicine & Biology*, 45:2417–2439, 2000.

M. W. Jacobson and K. Thielemans. Optimizability of loglikelihoods for the estimation of detector efficiencies and singles rates in PET. In *IEEE Nuclear Science Symposium and Medical Imaging Conference Record*, pages 4580–4586, 2008.

S. Jan, G. Santin, D. Strul, S. Staelens, K. Assié, D. Autret, and C. Morel. GATE: a simulation toolkit for PET and SPECT. *Physics in Medicine and Biology*, 49(19):4543–61, 2004.

Y. Jian, B. Planeta, and R. E. Carson. Evaluation of bias and variance in low-count OSEM list mode reconstruction. *Physics in Medicine and Biology*, 60: 15–29, 2014.

J. Jiao, P. Markiewicz, N. Burgos, D. Atkinson, B. Hutton, S. Arridge, and S. Ourselin. Detail-preserving PET reconstruction with sparse image representation and anatomical priors. In *International Conference on Information Processing in Medical Imaging*, pages 540–551. Springer, 2015.

L. Jødal, S. B. Jensen, O. L. Nielsen, P. Afzelius, P. Borghammer, A. K. O. Alstrup, and S. B. Hansen. Kinetic modelling of infection tracers [18F] FDG, [68Ga] Ga-citrate, [11C] methionine, and [11C] donepezil in a porcine osteomyelitis model. *Contrast Media and Molecular Imaging*, pages 1–18, 2017.

N. Karakatsanis, P. Robson, M. Dweck, R. Abgral, M. Trivieri, J. Sanz, J. Contreras, J. Narula, M. Padilla, U. Gidwani, V. Fuster, J. Kovacic, and Z. Fayad. MR-based attenuation correction in cardiovascular PET/MR imaging: challenges and practical solutions for cardiorespiratory motion and tissue class segmentation. *Journal of Nuclear Medicine*, 57(supplement 2):452–452, 2016.

N. Karakatsanis, M. Trivieri, M. Dweck, P. Robson, R. Abgral, R. Soler, C. Calcagno, V. Mani, C. Tsoumpas, J. Kovasic, and Z. A. Fayad. Simultaneous assessment of carotid plaque inflammation and micro-calcification with dual-tracer 18F-FDG: 18F-NaF PET-MR imaging: a clinical feasibility study. *Journal of Nuclear Medicine*, 58(Supplement 1):446–446, 2017.

N. A. Karakatsanis, E. Fokou, and C. Tsoumpas. Dosage optimization in positron

emission tomography: state-of-the-art methods and future prospects. *American Journal of Nuclear Medicine and Molecular Imaging*, 5:527–547, 2015.

K. Karaoglanis, I. Polycarpou, N. Efthimiou, and C. Tsoumpas. Appropriately regularized OSEM can improve the reconstructed PET images of data with low count statistics. *Hellenic Journal of Nuclear Medicine*, 18:140–145, 2015.

V. Keereman, Y. Fierens, T. Broux, Y. De Deene, M. Lonneux, and S. Vandenberghe. MRI-based attenuation correction for PET/MRI using ultrashort echo time sequences. *Journal of Nuclear Medicine*, 51(5):812–818, 2010.

F. Knoll, M. Holler, T. Koesters, R. Otazo, K. Bredies, and D. K. Sodickson. Joint MR-PET reconstruction using a multi-channel image regularizer. *IEEE Transactions on Medical Imaging*, 36(1):1–16, 2017.

H. Kobayashi, M. R. Longmire, M. Ogawa, P. L. Choyke, and S. Kawamoto. Multiplexed imaging in cancer diagnosis: applications and future advances. *The Lancet Oncology*, 11(6):589 – 595, 2010.

F. A Kotasidis, C. Tsoumpas, and A. Rahmim. Advanced kinetic modelling strategies: towards adoption in clinical PET imaging. *Clinical and Translational Imaging*, 2(3):219–237, 2014.

R. Laforest, T. L. Sharp, J. A. Engelbach, N. M. Fettig, P. Herrero, J. Kim, J. S. Lewis, D. J. Rowland, Y. Tai, and M. J. Welch. Measurement of input functions in rodents: challenges and solutions. *Nuclear Medicine and Biology*, 32(7):679–685, 2005.

K. Lange and R. Carson. EM reconstruction algorithms for emission and trans-

mission tomography. *Journal of Computer Assisted Tomography*, 8:306–316, 1984.

E. Levitan and G. T. Herman. A maximum a posteriori probability expectation maximization algorithm for image reconstruction in emission tomography. *IEEE Transactions on Medical Imaging*, 6(3):185–192, 1987.

R. Levkovilz, D. Falikman, M. Zibulevsky, A. Ben-Tal, and A. Nemirovski. The design and implementation of COSEN, an iterative algorithm for fully 3-D listmode data. *IEEE Transactions on Medical Imaging*, 20(7):633–642, 2001.

Y. Li, G. R. Berenji, W. F. Shaba, B. Tafti, E. Yevdayev, and S. Dadparvar. Association of vascular Fluoride uptake with vascular calcification and coronary artery disease. *Nuclear Medicine Communications*, 33(1):14–20, 2012.

K. Lin, S. Huang, Y. Choi, R. C. Brunken, H. R. Schelbert, and M. E. Phelps. Correction of spillover radioactivities for estimation of the blood time-activity curve from the imaged LV chamber in cardiac dynamic FDG PET studies. *Physics in Medicine and Biology*, 40:629, 1995.

J. S. Liow and S. C. Strother. Practical tradeoffs between noise, quantitation, and number of iterations for maximum likelihood-based reconstructions. *IEEE Transactions on Medical Imaging*, 10:563–571, 1991.

J. Litton. Input function in PET brain studies using MR-defined arteries. *Journal of Computer Assisted Tomography*, 21:907–909, 1997.

F. Liu, H. Jang, R. Kijowski, T. Bradshaw, and A. B. McMillan. Deep learning MR imaging–based attenuation correction for PET/MR imaging. *Radiology*, 286(2):676–684, 2017.

A. Martinez-Möller, M. Souvatzoglou, G. Delso, R. A. Bundschuh, C. Chefd'hotel, S. I. Ziegler, N. Navab, M. Schwaiger, and S. G. Nekolla. Tissue classification as a potential approach for attenuation correction in whole-body PET/MRI: evaluation with PET/CT data. *Journal of Nuclear Medicine*, 50 (4):520–526, 2009.

D. W. McRobbie, E. A. Moore, and M. J. Graves. *MRI from Picture to Proton*. Cambridge University Press, 2017.

A. Mehranian and H. Zaidi. Emission-based estimation of lung attenuation coefficients for attenuation correction in time-of-flight PET/MR. *Physics in Medicine and Biology*, 60:4813, 2015.

A. Mehranian, A. Rahmim, M. R. Ay, F. Kotasidis, and H. Zaidi. An ordered-subsets proximal preconditioned gradient algorithm for edge-preserving PET image reconstruction. *Medical Physics*, 40(1-14), 2013.

A. Mehranian, H. Arabi, and H. Zaidi. Vision 20/20: Magnetic resonance imaging-guided attenuation correction in PET/MRI: Challenges, solutions, and opportunities. *Medical Physics*, 43(3):1130–1155, 2016.

A. Mehranian, M. Belzunce, C. Prieto, A. Hammers, and A. J. Reader. Synergistic PET and SENSE MR image reconstruction using joint sparsity regularization. *IEEE Transactions on Medical Imaging*, 37:20–34, 2018.

S. R. Meikle, B. F. Hutton, D. L. Bailey, P. K. Hooper, and M. J. Fulham. Accelerated EM reconstruction in total-body PET: potential for improving tumour detectability. *Physics in Medicine and Biology*, 39:1689–1704, 1994.

H. W. Müller-Gärtner, J. M. Links, J. L. Prince, R. N. Bryan, E. McVeigh, J. P. Leal, C. Davatzikos, and J. J. Frost. Measurement of radiotracer concentration in brain gray matter using positron emission tomography: MRI-based correction for partial volume effects. *Journal of Cerebral Blood Flow and Metabolism*, 12:571–583, 1992.

E. Ü. Mumcuoglu, R. M. Leahy, and S. R. Cherry. Bayesian reconstruction of PET images: methodology and performance analysis. *Physics in Medicine and Biology*, 41:1777–1807, 1996.

O. L. Munk, L. P. Tolbod, S. B. Hansen, and T.V. Bogsrud. Point-spread function reconstructed PET images of sub-centimeter lesions are not quantitative. *European Journal of Nuclear Medicine and Molecular Imaging, Physics*, 4(1): 5, 2017.

S. Musafargani, K. K. Ghosh, S. Mishra, P. Mahalakshmi, P. Padmanabhan, and B. Gulyás. PET/MRI: a frontier in era of complementary hybrid imaging. *European Journal of Hybrid Imaging*, 2(1):12–39, 2018.

P. Novosad and A. J. Reader. MR-guided dynamic PET reconstruction with the kernel method and spectral temporal basis functions. *Physics in Medicine and Biology*, 61:4624–4645, 2016.

J. Nuyts. The use of mutual information and joint entropy for anatomical priors in emission tomography. In *IEEE Nuclear Science Symposium and Medical Imaging Conference Record*, volume 6, pages 4149–4154, 2007.

J. Nuyts, P. Dupont, S. Stroobants, R. Benninck, L. Mortelmans, and P. Suetens. Simultaneous maximum a posteriori reconstruction of attenuation and activity

distributions from emission sinograms. *IEEE Transactions on Medical Imaging*, 18(5):393–403, 1999.

J. Nuyts, G. Bal, F. Kehren, M. Fenchel, C. Michel, and C. Watson. Completion of a truncated attenuation image from the attenuated PET emission data. *IEEE Transactions on Medical Imaging*, 32(2):237–246, 2013.

J. P. B. O'Connor, E. O. Aboagye, J. E. Adams, H. J. Aerts, S. F. Barrington, A. J. Beer, R. Boellaard, S. E. Bohndiek, M. Brady, G. Brown, D. L. Buckley, T. L. Chenevert, L. P. Clarke, S. Collette, G. J. Cook, N. M. deSouza, J. C. Dickson, C. Dive, J. L. Evelhoch, C. Faivre-Finn, F. A. Gallagher, F. J. Gilbert, R. J. Gillies, V. Goh, J. R. Griffiths, A. M. Groves, S. Halligan, A. L. Harris, D. J. Hawkes, O S. Hoekstra, E. P. Huang, B. F. Hutton, E. F. Jackson, G. C. Jayson, A. Jones, D. Koh, D. Lacombe, P. Lambin, N. Lassau, M. O. Leach, T. Lee, E. L. Leen, J. S. Lewis, Y. Liu, M. F. Lythgoe, P. Manoharan, R. J. Maxwell, K. A. Miles, B. Morgan, S. Morris, T. Ng, A. R. Padhani, G. J. M. Parker, M. Partridge, A. P. Pathak, A. C. Peet, S. Punwani, A. R. Reynolds, S. P. Robinson, L. K. Shankar, R. A. Sharma, D. Soloviev, S. Stroobants, D. C. Sullivan, S. A. Taylor, P. S. Tofts, G. M. Tozer, M. van Herk, S. Walker-Samuel, J. Wason, K. J. Williams, P. Workman, T. E. Yankeelov, K. M. Brindle, L. M. McShane, A. Jackson, and J. C. Waterton. Imaging biomarker roadmap for cancer studies. *Nature Reviews Clinical Oncology*, 14(3):169–186, 2017.

L. Parra and H. H. Barrett. List-mode likelihood: EM algorithm and image quality estimation demonstrated on 2-D PET. *IEEE Transactions on Medical Imaging*, 17(2):228–235, 1998.

B. Pichler, E. Lorenz, R. Mirzoyan, W. Pimpl, F. Roder, M. Schwaiger, and S. I. Ziegler. Performance test of a LSO-APD PET module in a 9.4 Tesla magnet. In *IEEE Nuclear Science Symposium and Medical Imaging Conference Record*, volume 2, pages 1237–1239. IEEE, 1997.

I. Polycarpou, K. Thielemans, R. Manjeshwar, P. Aguiar, P. K. Marsden, and C. Tsoumpas. Comparative evaluation of scatter correction in 3D PET using different scatter-level approximations. *Annals of Nuclear Medicine*, 25(9):643–649, 2011.

A. Rangarajan, T. Hsiao, and G. Gindi. A bayesian joint mixture framework for the integration of anatomical information in functional image reconstruction. *Journal of Mathematical Imaging and Vision*, 12(3):199–217, 2000.

W. Raynor, S. Houshmand, S. Gholami, S. Emamzadehfard, C. S. Rajapakse, B. A. Blomberg, T. J. Werner, P. F. Høilund-Carlsen, J. F Baker, and Abass Alavi. Evolving role of molecular imaging with 18F-Sodium Fluoride PET as a biomarker for calcium metabolism. *Current Osteoporosis Reports*, 14(4): 115–125, 2016.

A. J. Reader and H. Zaidi. Advances in PE image reconstruction. *PET Clinics*, 2(2):173–190, 2007.

A. J. Reader, K. Erlandsson, M. A. Flower, and R. J. Ott. Fast accurate iterative reconstruction for low-statistics positron volume imaging. *Physics in Medicine and Biology*, 43(4):835–846, 1998a.

A. J. Reader, K. Erlandsson, M. A. Flower, and R. J. Ott. Fast accurate iterative

three-dimensional Bayesian reconstruction for low-statistics positron volume imaging. *IEEE Transactions on Nuclear Science*, 45(3):1090–1095, 1998b.

A. J. Reader, S. Ally, F. Bakatselos, R. Manavaki, R. J. Walledge, A. P. Jeavons, P. J. Julyan, S. Zhao, D. L. Hastings, and J. Zweit. One-pass list-mode EM algorithm for high-resolution 3-D PET image reconstruction into large arrays. *IEEE Transactions on Nuclear Science*, 49:693–699, 2002.

A. J. Reader, P. J. Julyan, H. Williams, D. L. Hastings, and J. Zweit. EM algorithm system modeling by image-space techniques for PET reconstruction. *IEEE Transactions on Nuclear Science*, 50(5):1392–1397, 2003.

D. Renker. New trends on photodetectors. *Nuclear Instruments and Methods in Physics Research Section A: Accelerators, Spectrometers, Detectors and Associated Equipment*, 571:1 – 6, 2007.

E. Roncali and S. R. Cherry. Application of silicon photomultipliers to positron emission tomography. *Annals of Biomedical Engineering*, 39:1358–1377, 2011.

O. G. Rousset, Y. Ma, and A. C. Evans. Correction for partial volume effects in PET: principle and validation. *Journal of Nuclear Medicine*, 39:904–911, 1998.

P. J. Schleyer, T. Schaeffter, and P. K. Marsden. The effect of inaccurate bone attenuation coefficient and segmentation on reconstructed PET images. *Nuclear Medicine Communications*, 31(8):708–716, 2010.

K. C. Schmidt and F. E. Turkheimer. Kinetic modeling in positron emission tomography. *The Quarterly Journal of Nuclear Medicine and Molecular Imaging*, 46:70–85, 2002.

G. Schramm, M. Holler, A. Rezaei, K. Vunckx, F. Knoll, K. Bredies, F. Boada, and J. Nuyts. Evaluation of parallel level sets and Bowsher's method as segmentation-free anatomical priors for time-of-flight PET reconstruction. *IEEE Transactions on Medical Imaging*, 37(2):590–603, 2018.

V. Schulz, T. Solf, B. Weissler, P. Gebhardt, P. Fischer, M. Ritzert, V. Mlotok, C. Piemonte, N. Zorzi, M. Melchiorri, S. Vandenberghe, V. Keereman, T. Schaeffter, and P. K. Marsden. A preclinical PET/MR insert for a human 3T MR scanner. In *IEEE Nuclear Science Symposium and Medical Imaging Conference Record*, pages 2577–2579. IEEE, 2009.

A. R. Seyal, K. Parekh, Y. S. Velichko, R. Salem, and V. Yaghmai. Tumor growth kinetics versus RECIST to assess response to locoregional therapy in breast cancer liver metastases. *Academic Radiology*, 21(8):950–957, 2014.

A. R. Seyal, K. Parekh, A. Arslanoglu, F. D. Gonzalez-Guindalini, S. M. Tochetto, Y. S. Velichko, and V. Yaghmai. Performance of tumor growth kinetics as an imaging biomarker for response assessment in colorectal liver metastases: correlation with FDG PET. *Abdominal Imaging*, 40(8):3043–3051, Oct 2015.

L. A. Shepp and Y. Vardi. Maximum likelihood reconstruction for emission tomography. *IEEE Transactions on Medical Imaging*, 1:113–122, 1982.

M. Shidahara, C. Tsoumpas, C. J. McGinnity, T. Kato, H. Tamura, A. Hammers, H. Watabe, and F. E. Turkheimer. Wavelet-based resolution recovery using an anatomical prior provides quantitative recovery for human population phantom PET [11c] raclopride data. *Physics in Medicine and Biology*, 57: 3097–3101, 2012.

J. Silva-Rodríguez, J. Cortés, X. Rodríguez-Osorio, J. López-Urdaneta, J. Pardo-Montero, P. Aguiar, and C. Tsoumpas. Iterative structural and functional synergistic resolution recovery (iSFS-RR) applied to PET-MR images in epilepsy. *IEEE Transactions on Nuclear Science*, 63:2434–2442, 2016.

U. Simoncic, S. Perlman, G. Liu, M. J. Staab, J. E. Straus, and R. Jeraj. Comparison of NaF and FDG PET/CT for assessment of treatment response in castration-resistant prostate cancers with osseous metastases. *Clinical Genitourinary Cancer*, 13(1):e7–e17, 2015.

D. L. Snyder and M. I. Miller. The use of sieves to stabilize images produced with the em algorithm for emission tomography. *IEEE Transactions on Nuclear Science*, 32(5):3864–3872, 1985.

D. L. Snyder and D. G. Politte. Image reconstruction from list-mode data in an emission tomography system having time-of-flight measurements. *IEEE Transactions on Nuclear Science*, 30(3):1843–1849, 1983.

S. Somayajula, C. Panagiotou, A. Rangarajan, Q. Li, S. R. Arridge, and R. M. Leahy. PET image reconstruction using information theoretic anatomical priors. *IEEE Transactions on Medical Imaging*, 30(3):537–549, 2011.

D. Strul and B. Bendriem. Robustness of anatomically guided pixel-by-pixel algorithms for partial volume effect correction in positron emission tomography. *Journal of Cerebral Blood Flow and Metabolism*, 19(5):547–559, 1999.

S. Surti, A. Kuhn, M. E Werner, A. E. Perkins, J. Kolthammer, and J. S. Karp. Performance of Philips Gemini TF PET/CT scanner with special consideration

for its time-of-flight imaging capabilities. *Journal of Nuclear Medicine*, 48(3): 471–480, 2007.

J. Tang and A. Rahmim. Bayesian PET image reconstruction incorporating anato-functional joint entropy. *Physics in Medicine and Biology*, 54(23):7063, 2009.

K. Thielemans, M. W Jacobson, and D. Belluzzo. On various approximations for the projectors in iterative reconstruction algorithms for 3D-PET. *Proceedings of the International Meeting on Fully 3D Image Reconstruction in Radiology and Nuclear Medicine*, 1999.

K. Thielemans, R. M. Manjeshwar, C. Tsoumpas, and F. P. Jansen. A new algorithm for scaling of PET scatter estimates using all coincidence events. In *IEEE Nuclear Science Symposium and Medical Imaging Conference Record*, volume 5, pages 3586–3590, 2007.

K. Thielemans, C. Tsoumpas, S. Mustafovic, T. Beisel, P. Aguiar, N. Dikaios, and M. W. Jacobson. STIR: software for tomographic image reconstruction release 2. *Physics in Medicine and Biology*, 57:867–883, 2012.

A. Torrado-Carvajal, J. Vera-Olmos, D. Izquierdo-Garcia, O. A. Catalano, M. A. Morales, J. Margolin, A. Soricelli, M. Salvatore, N Malpica, and C. Catana. Dixon-VIBE Deep Learning (DIVIDE) Pseudo-CT Synthesis for Pelvis PET/MR attenuation correction. *Journal of Nuclear Medicine*, pages 1–24, 2018.

D. W. Townsend. Multimodality imaging of structure and function. *Physics in Medicine and Biology*, 53(4):R1–R39, 2008.

C. Tsoumpas, P. Aguiar, K. S. Nikita, D. Ros, and K. Thielemans. Evaluation of the single scatter simulation algorithm implemented in the STIR library. In *IEEE Nuclear Science Symposium and Medical Imaging Conference Record*, volume 6, pages 3361–3365, 2004.

C. Tsoumpas, C. Buerger, A. P. King, P. Mollet, V. Keereman, S. Vandenberghe, V. Schulz, P. Schleyer, T. Schaeffter, and P. K. Marsden. Fast generation of 4D PET-MR data from real dynamic MR acquisitions. *Physics in Medicine and Biology*, 56(20):6597–613, 2011.

C. Tsoumpas, I. Polycarpou, K. Thielemans, Ch. Buerger, A. P. King, T. Schaeffter, and P. K. Marsden. The effect of regularization in motion compensated PET image reconstruction: a realistic numerical 4d simulation study. *Physics in Medicine and Biology*, 58(6):1759–1773, 2013.

C. Tsoumpas, D. Visvikis, and G. Loudos. Innovations in small-animal PET/MR imaging instrumentation. *PET Clinics*, 11(2):105–118, 2016.

E. Veklerov, J. Llacer, and E. J. Hoffman. MLE reconstruction of a brain phantom using a monte carlo transition matrix and a statistical stopping rule. *IEEE Transactions on Nuclear Science*, 35(1):603–607, 1988.

K. Vunckx, A. Atre, K. Baete, A. Reilhac, C. M. Deroose, K. Van Laere, and J. Nuyts. Evaluation of three MRI-based anatomical priors for quantitative PET brain imaging. *IEEE Transactions on Medical Imaging*, 31(3):599–612, 2012.

M. D. Walker, M. C. Asselin, P. J. Julyan, M. Feldmann, P. S. Talbot, T. Jones, and J. C. Matthews. Bias in iterative reconstruction of low-statistics PET

data: benefits of a resolution mode. *Physics in Medicine and Biology*, 56: 931–949, 2011.

G. Wang and J. Qi. PET image reconstruction using kernel method. *IEEE Transactions on Medical Imaging*, 34:61–71, 2015.

Y. Wang, A. J. Yee, C. Sirard, S. Landau, N. Raje, and U. Mahmood. Sodium Fluoride PET imaging as a quantitative pharmacodynamic biomarker for bone homeostasis during anti-DKK1 therapy for multiple myeloma. *Blood Cancer Journal*, 7(10):e615, 2017.

C. C. Watson, D. M. Newport, and M. E. Casey. A single scatter simulation technique for scatter correction in 3D PET. In *Three-Dimensional Image Reconstruction in Radiology and Nuclear Medicine*, pages 255–268. Springer, 1996.

D. Weishaupt, V. D. Köchli, and B. Marincek. *How does MRI work?: an introduction to the physics and function of magnetic resonance imaging*. Springer Science & Business Media, Berlin, 2008.

W. M. Wells, P. Viola, H. Atsumi, S. Nakajima, and R. Kikinis. Multi-modal volume registration by maximization of mutual information. *Medical Image Analysis*, 1(1):35–51, 1996.

C. Wu, F. Li, G. Niu, and X. Chen. PET imaging of inflammation biomarkers. *Theranostics*, 3(7):448–466, 2013.

P. A. Yushkevich, J. Piven, H. C. Hazlett, R. G. Smith, S. Ho, J. C. Gee, and G. Gerig. User-guided 3D active contour segmentation of anatomical

structures: Significantly improved efficiency and reliability. *Neuroimage*, 31 (3):1116–1128, 2006.

H. Zaidi, O. Mawlawi, and C. G. Orton. Simultaneous PET/MR will replace PET/CT as the molecular multimodality imaging platform of choice. *Medical Physics*, 34(5):1525–1528, 2007.

P. Zanotti-Fregonara, J. Liow, M. Fujita, E. Dusch, S. S. Zoghbi, E. Luong, R. Boellaard, V. W. Pike, C. Comtat, and R. B. Innis. Image-derived input function for human brain using high resolution PET imaging with [11C](R)-rolipram and [11C] PBR28. *PLoS One*, 6:e17056, 2011.